EXPERIMENTAL AND NUMERICAL INVESTIGATION OF SMALL PUNCH CREEP TEST

FRANCESCO CORTELLINO

M.Sc. (Mechanical Engineering)

Politecnico di Bari

Thesis submitted to The University of Nottingham

for the degree of Doctor of Philosophy

NOVEMBER 2014

ABSTRACT

The small punch creep testing (SPCT) technique has received much attention because it can provide information on the creep behaviour of materials with a very small specimen being tested. However, the nature of the test is complex and several aspects of the behaviour of the specimen, characterised by various non-linear concurrent processes, still need investigation.

This thesis reports the findings of experimental investigations and numerical analyses of SPCT carried out with the aim of improving the understanding of various features which characterise the behaviour of the specimen and to develop a novel technique to correlate the SPCT experimental output with the corresponding uniaxial creep test data, which is also presented.

The experimental programme consisted of SPCTs and pre-strained uniaxial creep tests, all performed at 600°C on the same batch of P91 steel. The pre-strained uniaxial creep tests have been used to evaluate the effects of large initial plasticity on the subsequent creep behaviour of P91 steel. For different stress levels, the results of the experiments have shown that creep was resisted for low pre-strain levels and enhanced for high pre-strains. The SPCT specimens have been investigated by use of scanning electron microscopy (SEM) to identify the effects of the punch load on the fracture surface of the failed specimens and the evolution of microstructural features in the material during the test. When the punch load was increased, the failure mechanism changed from creep-governed to plasticity-governed, as the presence of fresh dimples in the fracture surface increased. For the low-load tests, a macro crack was found to nucleate on the bottom surface of the specimen at approximately

20% of the failure life, and it subsequently propagated along the circumferential direction and through the thickness of the specimen.

A modified creep constitutive model has been developed based on the results of the pre-strained uniaxial creep tests and it has been implemented in a FE model of a SPCT capable to take into account the effects of the large initial plasticity, generated by the load application, on the creep response of the SPCT specimen. A global creep resistance in the SPCT specimen, due to the combination of localised different effects in various regions of the sample, was observed when these effects were included.

FE calculations have also been performed to investigate the effects of the eccentricity and the misalignment of the punch loading conditions on the punch minimum displacement rate (MDR) and on the time to failure. A correlation equation for these effects has also been reported. When the punch load was eccentric and misaligned, the MDR decreased and the time to rupture increased.

Further numerical analyses have been carried out to evaluate the effects of the friction modelling procedure on the behaviour of the specimen. The results obtained using the classical Coulomb friction theory are compared with those obtained by a more modern friction formulation, which takes into account the dependency of the friction coefficient on the contact pressure.

Finally, a novel interpretation technique for SPCT data has been developed using the results of experimental tests and numerical analyses. The interpretation technique takes into account the effects of the initial, large plasticity on the creep behaviour of the SPCT specimen, in order to correlate the SPCT results with the corresponding uniaxial data. A significant improvement in the accuracy of the correlation for rupture SPCT data with the corresponding uniaxial test results has been obtained.

LIST OF PUBLICATIONS

1. F. Cortellino, Thomas. H. Hyde, W. Sun and C. Pappalettere, 'Finite element calculation of contour integral parameters for cracked P91 pipe weld', *Materials Research Innovations*, **17** (5), pp.300-305,2013.

2. J. P. Rouse, F. Cortellino, W. Sun, T.H. Hyde and J. Shingledecker, 'Small punch creep testing: review on modelling and data interpretation', *Materials Science and Technology*, **29** (11), pp.1328-1345, 2013.

3. F. Cortellino, W. Sun, T. H Hyde and J. Shingledecker, 'The effects of geometrical inaccuracies of the experimental set-up on small punch creep test results', *The Journal of Strain Analysis for Engineering Design*, **49** (8), pp. 571-582, 2014.

4. T. H. Hyde, F. Cortellino, J. P. Rouse and W. Sun, 'Small Punch Creep Testing and Data Analysis of a P91 Steel at 650°C', in: K. Matocha, H. R and W. Sun (eds.), '2nd International Conference SSTT - Determination of mechanical properties of materials by small punch and other miniature testing techiques, Ostrava (Czech Republic), October 2nd to 4th, 2012', pp. 64-74, OCELOT s.r.o.

5. F. Cortellino, J. P. Rouse, W. Sun, T.H. Hyde and J. Shingledecker, 'Comparison of Interpretation Techniques for the Small Punch Creep Test Method for a High Temperature Steel', 'Energy Materials Conference 2012: High Temperature Materials, 18th-19th of October 2012', Loughborough (UK).

6. F. Cortellino, R. Chen, W. Sun and T.H. Hyde, 'A Microscopic Investigation on the Failure Mechanisms of Small Punch Creep Test of a P91 Steel at 873 K', in: K.

Matocha, H. R and W. Sun (eds.), '3rd International Conference SSTT - Determination of mechanical properties of materials by small punch and other miniature testing techiques, Castle Seggau (Austria), September 23rd to 25th, 2014', pp. 260-269, OCELOT s.r.o.

7. F. Cortellino, J.P. Rouse, W. Sun and T.H. Hyde, 'A study on the effect of initial plasticity on the small punch creep test for a P91 steel at 600°C', in: K. Matocha, H. R and W. Sun (eds.), '3rd International Conference SSTT - Determination of mechanical properties of materials by small punch and other miniature testing techiques, Castle Seggau (Austria), September 23rd to 25th, 2014', pp. 300-311, OCELOT s.r.o.

8. F. Cortellino, W. Sun and T. H. Hyde, 'On the effects of friction modelling on Small Punch Creep Test results: a numerical investigation', submitted to *International Journal of Pressure Vessels and Piping, under peer review*.

ACKNOWLEDGEMENTS

First of all, I would like to acknowledge my supervisors, Prof Wei Sun and Prof Thomas H. Hyde. Their expert advice, guidance and support during my studies were fundamental for this dissertation to be completed. The financial support provided by the Electrical Power Research Institute (EPRI), Charlotte (NC), U.S.A., that sponsored the research, is also acknowledged.

Also, I would like to thank Dr James P. Rouse who provided an extremely valuable contribution to the pre-strained testing programme and to the subsequent modelling activities, and Dr Rong Chen, from the Institute of Aeronautical Materials, Beijing, who helped me with the microscopical investigations. The collaboration with Dr Rouse also led to the publication of a literature review paper, on small punch creep testing, I am a co-author of. The technical support provided by Mr Shane Maskill, senior technician from this University, is also acknowledged.

I need to express my highest gratitude to my Father, my Mother, Raffaella and Nicola. They have always given the strength to choose the hardest option when life required it and I would have never been able to achieve any of the targets I aimed to without their example of honesty, decency and success.

My thanks also go to my colleagues of the Structural Integrity and Dynamics Research Group, which I am proud to be part of, for the lovely memories of my Ph.D. time. My particular gratitude goes to Dr Bahlassn S.M. Ali, whose friendship honoured me, and to Dr Rupesh Patel, who helped me in innumerable occasions.

CONTENTS

NOMENCLATURE

a_p	Receiving hole radius for the small punch test rig
a_r	Transverse axis of the small ring test specimen
A_{KR}	Material constant in Kachanov-Rabotnov constitutive model
A_{LM}	Material constant in Liu & Murakami constitutive model
$\underline{\mathbf{b}}$	Burger's vector
b_i	Length of the impression creep test specimen
b_r	Axis of the small ring test specimen parallel to the load direction
b_t	Width of the loading bar of the impression creep test specimen
$b_{0,R}$	Thickness of the small ring test specimen (out-of-plane)
B	Stress multiplier in Norton's creep law
C_a	Scaling constant for Leu's friction formulation
d_i	Width of the impression creep test specimen
d_r	Thickness of the small ring test specimen (in-plane)
d_t	Thickness of the two-bar specimen
$d\lambda$	Scalar representing the variation of the hardening behaviour of materials
$D_{i,T}$	Diameter of the two-bar specimen
D_{SPT}	Diameter of the small punch test specimen
E	Young's modulus in generic material conditions
E_0	Young's modulus for undamaged material
EGL_{SRT}	Equivalent gauge length of the small ring test specimen
G	Shear modulus
h_i	Thickness of the impression creep test specimen
h_{punch}	High of the punch
h_0	High of the punch at the contact edge
I	Identity tensor
k_T	Length of the supporting end of the two-bar specimen
K_f	Shear strength of materials
K_{SP}	Correction factor for the load/stress correlation equation reported in the CEN code of practice

$L_{0,T}$	Effective length of the two-bar specimen
m	Time exponent of the Bailey/Norton creep law
MDR	Minimum displacement rate in a generic configuration
MDR_0	Minimum displacement rate in the centred configuration
MSR	Minimum strain rate
MSR_{CORR}	"Modified" minimum strain rate, obtained by using converted small punch creep test data and representing the behaviour of not pre-strained material
MSR_{EXP}	Minimum strain rate obtained by converting the experimental small punch creep test data
$MSR_{SPCT,N-PRE}$	Minimum strain rate obtained by converting the FE results of small punch creep test without including the effects of initial plasticity
$MSR_{SPCT,PRE}$	Minimum strain rate obtained by converting the FE results of small punch creep test with the effects of initial plasticity included
n	Stress exponent in Norton's creep law
n_2	Stress exponent in Kachanov-Rabotnov constitutive model
n_3	Stress exponent in Liu & Murakami constitutive model
p	Contact pressure
p_l	Lateral pressure
$\overline{p}$	Average contact pressure
P	Load
P_{Clamp}	Clamping load
P_x	Punch load in the x-direction
P_z	Punch load in the z-direction
q_2	Material constant for the Liu & Murakami constitutive model
Q_c	Activation energy for creep
r_1	Radial coordinate in a generic point of the unsupported region of the membrane in the Chakrabarty theory
r_2	Radial coordinate in a generic point of the supported region of the membrane in the Chakrabarty theory
R	Boltzmann constant
R_s	Punch radius
S_{ij}	Deviatoric stress tensor
$SPCT$	Small punch creep test
SRT	Small ring test
t	Time
t_f	Time to failure
t_{f0}	Time to failure in the centred configuration
$t_{f,n-p}$	Time to failure for not pre-strained material
$t_{f,p}$	Time to failure for pre-strained material

$t_{f,CORR}$	"Modified" time to failure, obtained by using converted small punch creep test data and representing the behaviour of not pre-strained material
$t_{f,EXP}$	Time to failure obtained by converting the experimental small punch creep test data
$t_{fFE,N-PRE}$	Time to failure obtained by converting the FE results of small punch creep test without including the effects of initial plasticity
$t_{fFE,PRE}$	Time to failure obtained by converting the FE results of small punch creep test with the effects of initial plasticity included
t_h	Thickness of the small punch test specimen
u_x	Displacement in the x-direction
u_z	Displacement in the z-direction
U_s	Elastic distortion energy
w_i	Width of the impression creep test specimen
z	High of a generic point of the membrane

α	Reference stress parameter
α_c	Contact area parameter for Leu's friction formulation
α_D	Stress multi-axiality parameter
β	Reference stress parameter
γ	Parameter to quantify the effects of initial plastic strain on the converted minimum strain rate obtained from SPCT data
δ	Punch eccentricity
Δ	Load-line displacement
Δu_{Clamp}	Displacement imposed to the specimen holder
$\dot{\Delta}$	Load-line displacement rate
ε_c	Circumferential strain component
ε_{ij}	Strain tensor
ε_{ij}^c	Creep strain tensor
ε_{ij}^e	Elastic strain tensor
ε_{ij}^p	Plastic strain tensor
ε_{ij}^t	Total strain tensor
ε_r	Radial strain component
$\varepsilon_{p,true}$	True plastic strain
$\varepsilon_{p,pre}$	Plastic pre-strain
ε_{pre}	Total engineering pre-strain
ε_t	Strain component in the through-thickness direction
$\varepsilon_{t,eng}$	Engineering total strain
ε_{EQ}	Equivalent strain

$\varepsilon_{EQ,EDGE}$	Equivalent strain at the punch/membrane contact edge
$\varepsilon^{in}_{EQ,EDGE}$	Initial equivalent strain at the punch/membrane contact edge
$\dot{\varepsilon}^{c}_{ij}$	Creep strain rate tensor
$\dot{\varepsilon}^{c}_{MIN,p}$	Minimum creep strain rate for pre-strained material
$\dot{\varepsilon}^{c}_{MIN,0}$	Minimum creep strain rate for not pre-strained material
η	Reference stress parameter
θ	Punch misalignment
θ_{Ch}	Normal angle at the supports of the membrane
$\theta_{0,Ch}$	Normal angle at the edge of contact of the membrane
θ_r	Angular coordinate for the small ring specimen
λ_f	Parameter which quantifies the effects of initial plastic deformation on the failure time obtained from small punch creep test data
μ	Coefficient of friction
μ_{LIM}	Limit value for the coefficient of friction
ν	Poisson ratio
ρ_c	Curvature radius in the circumferential direction
ρ_r	Curvature radius in the radial direction
σ_c	Stress component in the circumferential direction
σ_{EFF}	Effective stress
σ_{EQ}	Equivalent stress
σ^{UNI}_{EQ}	"Equivalent" uniaxial stress
σ_{ij}	Stress tensor
σ_{NOM}	Nominal stress
σ_r	Stress component in the meridional direction
σ_{REF}	Reference stress
σ_{RUP}	Rupture stress
σ^{p}_{RUP}	Peak rupture stress
σ_y	Yielding stress
τ_f	Friction shear force
τ_{MAX}	Maximum shear stress
ϕ	Pre-strain parameter for the minimum strain rate
$\phi_{1,Ch}$	Normal angle in the supported region of the membrane
$\phi_{2,Ch}$	Normal angle in the unsupported region of the membrane
χ_{LM}	Material constant in the Liu & Murakami constitutive model
χ_{KR}	Material constant in the Kachanov-Rabotnov constitutive model
ψ	Pre-strain parameter for the time to failure
ω	Creep damage parameter
ω_i	Generic ith internal variable in damage laws
Ω	Cross section in the current configuration

$\Omega_{c,A}$	Apparent contact area
$\Omega_{c,R}$	Real contact area
Ω_0	Cross section in the undamaged configuration

CHAPTER 1

INTRODUCTION

1.1 Background

In the recent years, miniature specimens testing techniques have received increasing attention from the power generation industry in view of several situations where the amount of material available for testing is limited [53, 91]. One of these cases is life assessment of in-service components, where the material which can be taken without impairing the structural integrity of the analysed component is limited [11, 27, 28, 31, 57, 72, 76, 91]. This investigation is of high importance because, when components are approaching the end of their designed operational life, extension programmes can be more economically convenient than their replacement [31], as they were designed by particularly conservative procedures [47]. In view of these economical and safety reasons, the uncertainty related to life assessment techniques needs to be reduced, and in-service components testing constitutes a key approach [8, 31].

Focused analyses of critical locations of high temperature components, such as the Heat Affected Zones (HAZ) of welds, can also be carried out by use of miniature testing techniques [8, 34, 36, 53, 91, 111]. This is particularly useful for components made from high chromium steel, such as P91 (9Cr-1Mo-V-Nb) steel, adopted for piping systems of fossil fuelled power plant since the 1970s [36, 94], because of its superior properties at high temperature compared to other materials, such as stainless steels [34]. A main concern with

the application of these advanced high temperature steels is the creep resistance of their welds as a major cause of failure was found to be Type IV cracking, which occurs at the interface between the fine grain (FG) HAZ and the parent material (PM), depending on local loading conditions [20, 111]. Blagoeva et al. [8] reported that, in a P91 steel weld tested at 600°C, the least creep resistant material region is the FG-HAZ, while the PM and the weld metal (WM) exhibit a significantly higher creep resistance. In view of these considerations, a conventional cross-weld specimen would not be suitable to characterise the creep material behaviour of each region of the weld, because the FG-HAZ, where large creep deformations occur, would be constrained by the WM and the PM [34]. Other situations where the amount of material available for testing is small consists of the development of new alloys [42, 56, 91].

Generally, miniature specimens used for creep testing can be divided into two categories: specimens characterised by a shape and form similar to that of full size specimens but manufactured in miniature dimensions, and specimens developed to benefit from their small size [56]. The first category includes miniature uniaxial test specimens, which are characterised by a total length that can reach 20 [mm]. The procedures for the manufacturing, handling, testing and the data interpretation of these specimens show a degree of difficulty which increases with the decrease in specimen size [56].

In order to overcome the difficulties related to miniature uniaxial test specimens, various small specimen testing techniques have been developed. These include the impression creep test, the small ring specimen creep test, the small punch creep test (SPCT) and the two-bar specimen creep test [41, 42, 51–54, 56]. These specimens can be manufactured from scoop samples, taken e.g. from in-service components without any deterioration of their structural integrity, or from the HAZ of welds. The impression creep test and the small ring test can be used to characterise the steady-state creep behaviour of materials, i.e. the minimum creep strain rate, but they cannot provide the creep rupture behaviour, as the specimen is not taken to rupture [42, 45, 46, 52, 53]. On the other hand, small two bar creep specimens and SPCT specimens can be tested until failure, therefore they can be used to obtain tertiary creep and rupture behaviour of materials [45, 46]. Despite of these

advantages, which make the SPCT a very promising testing method, this technique is still not universally accepted, due to limitations which concern the test repeatability (because test results depend on the geometry of the experimental set-up) and the procedure used to correlate SPCT data with the output of corresponding full size uniaxial creep tests [31].

The nature of the test is complex, as several non-linear factors, such as non-linear contact, non-linear material behaviour, large strains and large deformations, concurrently characterise the behaviour of the specimen [51]. In the early stages, large plastic deformations occur in localised regions of the specimen [34, 36, 91] and affect the subsequent creep behaviour of the material and the response of the specimen. The contact conditions between the specimen and the test rig are complicated and have a significant effect on the test output [24, 25]. In view of the complex nature of the SPCT, there is no established, straightforward procedure to convert the experimental results into those of conventional uniaxial creep tests [51]. In an attempt to overcome some of the repeatability issues and propose a universally accepted correlation technique, the European Committee for Standardisation (CEN) developed a draft code of practice (workshop agreement CWA 15627) for small punch creep testing of metallic materials, which constitutes a key step towards a standardisation of SPCT [1]. In the CEN draft code of practice, a specimen geometry and a test apparatus are recommended, and a procedure to correlate SPCT data with corresponding uniaxial creep test results is also reported.

1.2 Thesis objectives

The first objective of the research is the improvement of the understanding of various features characterising the behaviour of the SPCT specimen by using experimental investigations and FE analyses. Experimental techniques have been adopted to investigate the evolution of micro-mechanical features which characterise the behaviour of the specimen during the test and to identify the effects of prior plastic deformation on the subsequent creep response of a P91 steel at 600°C. The results of the experimental investigations have been used to develop an improved constitutive model which has been adopted in FE calcu-

lations of a SPCT in order to quantify the effects of the initial plastic deformation on the output of the test.

The work is also aimed to investigate the effects of the procedure used to model the friction interaction between the punch and the specimen. An axisymmetric FE model of SPCT, capable of taking into account the variation of the friction coefficient with the local loading conditions, has been developed and the results have been compared with those obtained by adopting the models commonly used.

It is also aimed to investigate the effects of inaccuracies of the loading configuration on the SPCT output by use of numerical calculations. A 3D FE model of SPCT has been developed in order to include asymmetric loading conditions in the analyses.

The final objective of the research is to develop an improved interpretation technique which is capable of taking into account the effects of the initial, large deformations occurring in the specimen and to correlate the SPCT output with the results of corresponding uniaxial creep tests by a physically-based approach.

1.3 Thesis outline

Chapter 2 consists of a literature review focused on plasticity and creep behaviour of metallic materials (together with the effects of their interaction) and on small specimen creep testing techniques, with particular attention to the SPCT method. The analytical and numerical modelling procedures of SPCT and the techniques currently used for data interpretation are discussed in detail.

Chapter 3 reports the results of pre-strained uniaxial creep tests (which have been used to investigate the plasticity/creep interaction) and SPCTs carried out on a P91 steel at 600°C. Chapter 4 reports a microscopical investigation carried out on the specimens of the SPCTs discussed in Chapter 3. The effects of the punch load on microscopical features in the material and the evolution of the failure and the deformation mechanisms and of

material's features during the test will be shown.

The results of elastic/plastic/creep FE analyses of SPCT, which have been performed using a constitutive model able of taking into account the effects of plasticity on the creep behaviour of the specimen, are reported in Chapter 5. These effects constitute a key factor in the numerical modelling of SPCT.

The effects of geometrical inaccuracies of the loading procedure on the SPCT output, investigated using 3D elastic/creep FE analyses of a SPCT, are reported in Chapter 6. Chapter 7 includes the results of a numerical study focused on the friction modelling procedure for the contact interaction between the punch and the specimen. The FE results obtained by using the classical Coulomb's theory are compared with those obtained by using a friction formulation able of taking into account the effects of the local contact load, between the punch and the specimen, on the coefficient of friction.

The numerical results discussed in Chapter 5 and the experimental findings reported in Chapter 3 have been used to develop a new procedure for the interpretation of SPCT data. This procedure is presented in Chapter 8. Finally, Chapter 9 reports the concluding remarks and future work considerations.

CHAPTER 2

LITERATURE REVIEW

2.1 Materials structure and defects - an overview

On a microscopical level, crystalline materials do not always exhibit a perfect structure. As a result their behaviour is characterised by a large number of defects of different types [3, 12]. These defects include both irregularities of the structure of the material and the presence of atoms of different types in the crystal.

Some defect types, encountered in crystals, are of the point defect types, i.e. *vacancies* and *impurities*. A vacancy is a site in a crystal where an atom is missing. Alternatively, it may result in atoms of a different material, i.e. the solute, dissolved in the hosting metal, i.e. the solvent. Two types of solid solutions can be found, i.e. substitutional solutions, where the solute atoms replace those of the host material, and interstitial solutions, where solute atoms are located in interstices among the atoms of the host crystal. Since solute atoms are generally of different size to those of the hosting metal, distortion occurs in the lattice at locations close to the solute atoms. Impurities also modify the properties of materials, and, in many cases, they are added to metals, generating *alloys*, in order to obtain specific characteristics, e.g. improved strength or resistance to corrosion [3, 12] etc.

In metals, linear defects, i.e. *dislocations*, may exist. These consist of atoms being misplaced, and lattice distortion in the proximity of a linear path, generally referred to as

dislocation line [3]. In Figure 2.1 an *edge dislocation* is schematically represented. In this configuration, an extra semi-plane of atoms starting from the dislocation line is inserted in the crystal, and alters the regular lattice structure. The inter-atomic bonds of the top half of the scheme shown in Figure 2.1 are compressed, while, those of the bottom half are stretched. The distortion of the lattice is concentrated within an area around the dislocation line, while, at a distance from the dislocation line, the distribution of the atoms is not affected [12].

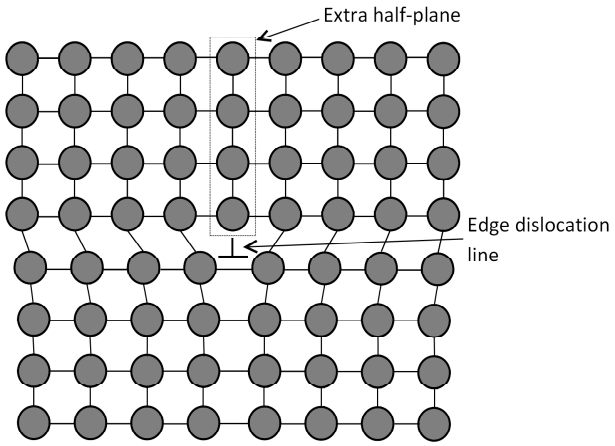

Figure 2.1: Schematic representation of an edge dislocation. Adapted from [3], Figure 6.13

The *screw dislocation* is another type of linear defect. This type of defect is generated when a part of the lattice exhibits a displacement, on the direction parallel to the dislocation line, with respect to the adjacent region of the crystal. Figure 2.2 shows a schematic representation of a screw dislocation. Also in this case, the distortion of the lattice is concentrated in the region close to the dislocation line, while, in the far field, the crystal is virtually perfect.

The displacements of atoms related to dislocations are described by the *Burger's vector*, $\mathbf{b}$. For edge dislocations, the $\mathbf{b}$ vector is perpendicular to the dislocation line while, for screw dislocations, $\mathbf{b}$ is parallel to the dislocation line. In crystalline materials, dislocations generally consist of various components of different nature, i.e. edge and screw dislocation segments, called *mixed dislocations*, for which the dislocation line is generally curved, while $\mathbf{b}$ does not change orientation. For metallic materials, the $\mathbf{b}$ vector is always oriented

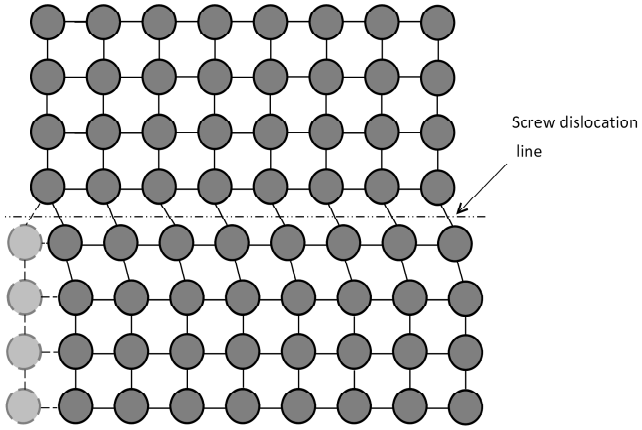

Figure 2.2: Schematic representation of dislocations in a crystal lattice. Adapted from [12], Figure 4.4

along the direction with the highest atomic density, and it is characterised by an absolute value equal to the inter-atomic distance [3, 12].

The presence and the motion of dislocations is the cause of plastic and creep deformation of metals and of the differences found between the theoretical and the actual strengths of real crystalline materials [3].

In addition to point and linear defects, a crystal can also exhibit interfacial defects, such as grain boundaries, phase boundaries or external surfaces, which are the interface between material regions characterised by different crystalline structure or orientation [12]. In grain boundaries, crystals with different orientations, called grains, are located adjacent to each other and, based on the angle between their crystal orientations, a distinction between *low-angle* and *high-angle* grain boundaries can be made. In fact, low angle grain boundaries can be described by a distribution of dislocations [12]. Grains can have different chemical compositions, as in the case of alloys, and, in the boundary regions, atoms are organised in an intermediate orientation between those of the interfacing lattices, leading to a higher energetic level compared to the central regions of the grain. Because of the higher energetic content, grain boundaries are preferred locations for dislocation nucleation and interstitial solution sites. Low-angle grain boundaries have a lower energy than high angle grain boundaries [12].

2.2 Elasto-plastic behaviour of materials

2.2.1 Overview

When a solid body is loaded, it initially shows a fully recoverable elastic deformation, that is, if the load is removed, no residual deformation is found and the stress is fully determined by the strain [35]. Many materials, such as steels, exhibit a linear relationship between loads and deformation, and, hence, between stress and strain [55]. This is represented by Hooke's law, reported in equation (2.1), which relates the components of the strain and stress tensors in a generic reference system *(O,x,y,z)*, where *E* is the Young's modulus, ν is the Poisson's ratio and σ_{ij} and ε_{ij} are the stress and strain tensors, respectively (see also ref. [55]).

$$\varepsilon_{xx} = \frac{1}{E}[\sigma_{xx} - \nu(\sigma_{yy} + \sigma_{zz})] \tag{2.1a}$$

$$\varepsilon_{yy} = \frac{1}{E}[\sigma_{yy} - \nu(\sigma_{zz} + \sigma_{xx})] \tag{2.1b}$$

$$\varepsilon_{zz} = \frac{1}{E}[\sigma_{zz} - \nu(\sigma_{xx} + \sigma_{yy})] \tag{2.1c}$$

$$\varepsilon_{ij} = \frac{1+\nu}{E}\sigma_{ij}, i \neq j \tag{2.1d}$$

Figure 2.3 shows a stress/strain curve of a generic ductile material, such as a mild steel, obtained from uniaxial tensile tests, i.e. with principal stress components $\sigma_{11} \neq 0$ and $\sigma_{22} = \sigma_{33} = 0$ [35]. When the load level is increased, the behaviour of the material differs from the linear model and the elastic limit is reached (point A in Figures 2.3(a) and (b)), i.e. initial plastic deformation occurs in the specimen [35, 55].

The transition from elastic regime to plastic regime, which is characterised by significant plastic deformation, is referred to as yield [35, 37, 55, 88, 96]. In some materials, the yield point can be clearly identified in the tensile curve, as shown in Figure 2.3 (a), while, for others, the yield point is not as evident, as shown in Figure 2.3 (b). In view of this difficulty, the yield point of a material is defined as the stress, σ_y, at which a plastic, permanent deformation equal to ε_p=0.002 is induced, as indicated in Figure 2.3 (b). Typically, the

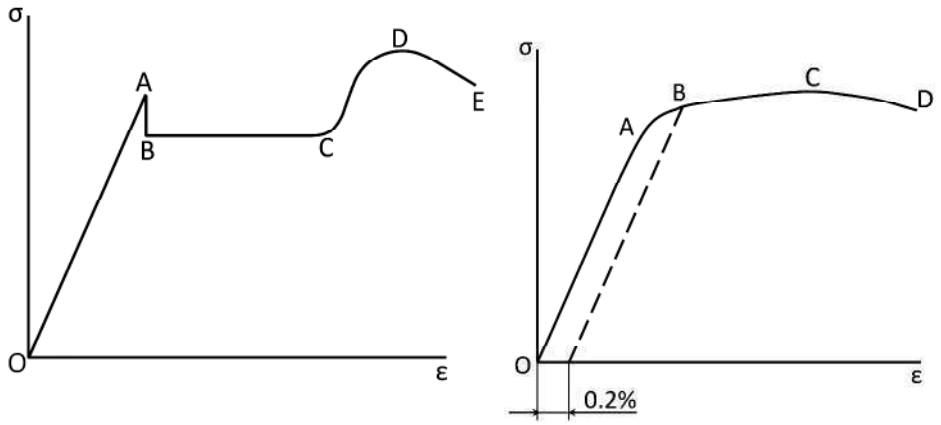

(a) (b)

Figure 2.3: Typical tensile curves obtained from (a) a mild steel and (b) a generic ductile material

plastic behaviour of metals can be described by the perfect plastic model or the multi-linear model, represented in Figures 2.4 (a) and (b), respectively.

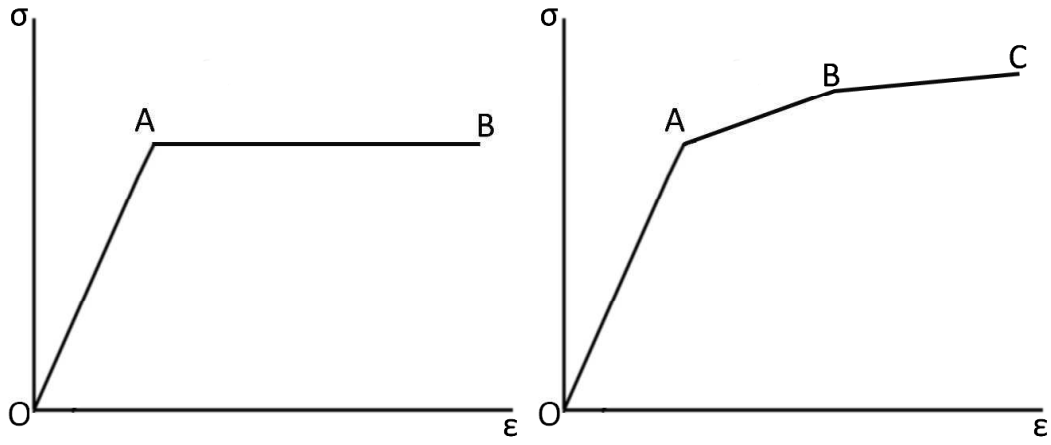

(a) (b)

Figure 2.4: Typical tensile curves obtained from (a) a mild steel and (b) a generic ductile material

When a solid body is loaded beyond the yielding limit, i.e. beyond the point A in Figures 2.3 (a) and (b), the unloading path does not overlap with that of loading, while it follows a linear curve parallel to the elastic section of the tensile curve, see Figure 2.3 (b). This leads to residual unrecoverable plastic deformation, ε_p, and the σ/ε relation is path dependent.

2.2.2 Yield criteria

In uniaxial tests, the yield stress, at which plastic deformation occurs in the specimen, can be obtained from the tensile curve, while, in components subjected to a more complex multi-axial stress field (such as the SPCT specimen), the yield stress cannot be directly obtained. In these situations, a yield criterion, i.e. a mathematical representation of the stress field under which yield occurs, needs to be identified [37]. Yield criteria are of the form of equation (2.2), where C_y is a material constant, and they relate the stress field, σ_{ij}, acting on the real component to uniaxial stress conditions, when yielding takes place.

$$f(\sigma_{ij}) = C_y \tag{2.2}$$

Under the hypothesis of plastic isotropy, the yield criterion does not depend on the reference system adopted, and, since plastic deformation does not involve any change in volume, the hydrostatic (spherical) part of the stress tensor, represented by equation (2.3) in a generic reference system *(O,x,y,z)*, does not have any influence on the yielding process, while the stress deviator, S_{ij}, defined by equation (2.4), is the component of the stress tensor which governs the yielding behaviour of the material, with *I* representing the identity tensor [5, 35, 37, 55, 87].

$$Sph(\sigma_{ij}) = \frac{\sigma_{xx} + \sigma_{yy} + \sigma_{zz}}{3}\, I \tag{2.3}$$

$$S_{ij} = \sigma_{ij} - Sph(\sigma_{ij}) = \sigma_{ij} - \frac{tr(\sigma_{ij})}{3}\, I \tag{2.4}$$

For ductile materials, the Tresca and the von Mises yield criteria are typically adopted. The Tresca criterion is based on the assumption that, in a generically loaded solid body, the onset of plasticity takes place when the maximum shear stress, τ_{max}, equals the maximum shear stress occurring, at yielding, in a uniaxial tensile test of the same material, i.e.

$\tau_{MAX}^{UNI} = \frac{1}{2}\sigma_y$, where σ_y is the yield stress obtained from the uniaxial curve [35, 88]. This criterion is based on the hypothesis that plastic deformation is governed by shear deformation which is related to dislocation motion in ductile materials. The Tresca criterion is reported in equation (2.5), written in the principal reference system [35, 55].

$$\frac{1}{2}max|\sigma_i - \sigma_j| = \frac{\sigma_y}{2} \implies max|\sigma_i - \sigma_j| = \sigma_y, i \neq j \tag{2.5}$$

The von Mises yield criterion is based on the comparison of the elastic distortion energy density (related to shear strain) corresponding to a generic multi-axial stress field with that of a uniaxial tensile test, for the same material. The elastic distortion energy density, U_S, defined by equation (2.6), is the difference between the total elastic energy density, U_{TOT}, and the energy density related to the volume variation, U_{VOL}. According to the von Mises yield criterion, described in equation (2.7), plastic deformation takes place when the shear strain energy density obtained in a multi-axial stress field equals that obtained during the tensile test at the yield point [35].

$$U_S = \frac{1+\nu}{6E}\left[(\sigma_1 - \sigma_2)^2 + (\sigma_2 - \sigma_3)^2 + (\sigma_3 - \sigma_1)^2\right] \tag{2.6}$$

$$\sigma_y = \frac{\sqrt{2}}{2}\sqrt{(\sigma_1 - \sigma_2)^2 + (\sigma_2 - \sigma_3)^2 + (\sigma_3 - \sigma_1)^2} = \sqrt{\frac{3}{2}S_{ij}S_{ij}} \tag{2.7}$$

In the principal stresses space, $(0, \sigma_1, \sigma_2, \sigma_3)$, the Tresca criterion, equation (2.5), is represented by an hexagonal prism, with its axis parallel to the hydrostatic axis, that is equally inclined to the principal axes directions and is characterised by the relations $\sigma_1 = \sigma_2 = \sigma_3$, while the von Mises criterion, equation (2.7), is represented by a cylinder, also with its axis parallel to the hydrostatic axis, circumscribing the Tresca criterion prism, see Figure 2.5 (a). This means that any variation of the hydrostatic stress, $\sigma_M = \frac{\sigma_1+\sigma_2+\sigma_3}{3}$, does not affect the yield of the material [35, 55]. When the stress field is biaxial, i.e. $\sigma_1, \sigma_2 \neq 0$ and $\sigma_3 = 0$, the Tresca and the von Mises yield criteria are represented, on the $(0, \sigma_1, \sigma_2)$ plane, by an hexagon and its circumscribing ellipsoid, respectively, see Figure 2.5 (b).

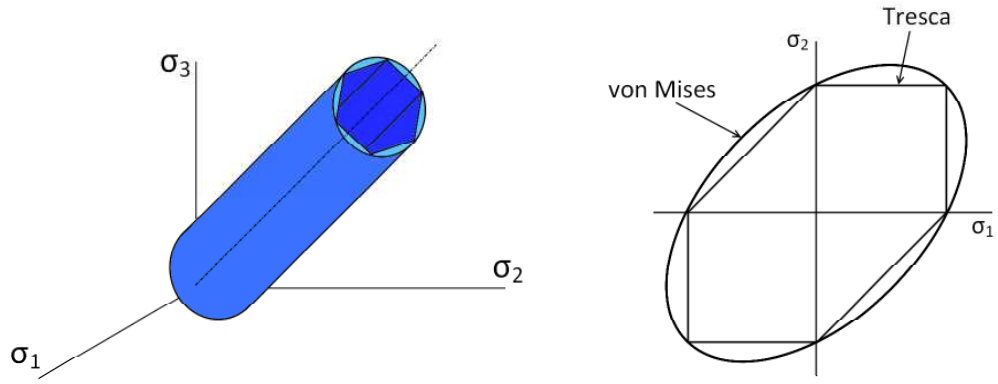

(a) (b)

Figure 2.5: Graphic representation of the Tresca and von Mises yield criteria (a) in the principal stress space and (b) in plane stress conditions. Adapted from [35], Figs. 3.9 and 3.10.

In Figures 2.5 (a) and (b), the Tresca yield surface is not smooth, but it consists of smooth faces which intersect in edges (Figure 2.5 (a)). This creates ambiguity in the calculation of the strain increment, resulting from yielding, for the stress states represented by these edges. In view of the *normality law*, for an isotropic material, the plastic strain increment, $d\varepsilon_p$, resulting from a stress state $\sigma(\sigma_1, \sigma_2, \sigma_3)$ on the yield surface, is normal to tangent plane to the yield surface in that stress state. If the yield surface is not smooth in $\sigma(\sigma_1, \sigma_2, \sigma_3)$, the normal direction to the yield surface in $\sigma(\sigma_1, \sigma_2, \sigma_3)$ is not univocally defined. However, a *cone of normals* to the yield surface in $\sigma(\sigma_1, \sigma_2, \sigma_3)$, in which the direction of $d\varepsilon_p$ lies, is bounded by the normal directions to the yield surface in the proximity of σ [35, 37]. For the Tresca criterion, the normal to the yield surface is not univocally defined on the edges of the yield surface (see Figure 2.5). The direction of $d\varepsilon_p$ for the stress states corresponding to each of the edges of the prism lies within the cone defined by the normals on the faces of the prism adjacent to the edge. The von Mises criterion does not exhibit this ambiguity, since it leads to a smooth yield surface, as Figure 2.5 shows.

Both these criteria are applicable to ductile metals, and experimental evidence shows that, for a bi-axial stress field (see Figure 2.5 (b)), the yield loci, regardless of their definition, are closer to the von Mises ellipsoid than the Tresca hexagon. However, in all cases, the Tresca criterion is more conservative than the von Mises equation [37, 88].

2.2.3 Plastic flow

As mentioned in Section 2.2.1, in the elastic regime, the strain field is univocally defined by the current stress while, when plasticity takes place, the stress field depends on the current state of the material and the loading history [35, 88, 96]. This difference is due to the nature of the processes characterising elastic and plastic deformations. Elastic behaviour is due to deformation of crystal lattice, and it does not involve any distortion, while plastic deformation involves motion of dislocations on preferential sliding planes with distortion of the crystalline lattice. Under the effects of a stress level higher than the yield strength of the material, dislocations can move in the crystal [3]. On the other hand, atoms of dissolved solutes, precipitate particles and other dislocations become obstacles to this motion and, when the equilibrium is reached between the stress field applied to the material and the resistance that obstacles oppose, dislocation slip stops. One of the classical theories of plasticity is the incremental theory of Prandtl-Reuss, reported in equation (2.8), which relates the total strain increment to the current deviatoric stress and the stress variation [88].

$$d\varepsilon_{ij}^{t} = d\varepsilon_{ij}^{p} + d\varepsilon_{ij}^{e} = d\lambda S_{ij} + \left[\frac{(1-2\nu)}{3E} tr(d\sigma_{ij})\; I + \frac{dS_{ij}}{2G}\right] \tag{2.8}$$

In equation (2.10), the elastic strain increment, $d\varepsilon_{ij}^{e}$, consists of a hydrostatic and a deviatoric contribution, while the scalar $d\lambda$, representing the variation of the hardening behaviour of the material, can be obtained from an equivalent uniaxial stress field, where $\sigma_1 = \sigma_{EQ}$ and $\sigma_2 = \sigma_1 = 0$, see equation (2.9).

$$d\varepsilon_{EQ}^{p} = d\lambda S_{EQ} = d\lambda \left(\sigma_{EQ} - \frac{1}{3}\sigma_{EQ}\right) \implies d\lambda = \frac{3}{2}\frac{d\varepsilon_{EQ}^{p}}{\sigma_{EQ}} \tag{2.9}$$

Therefore, the Prandtl - Reuss plastic flow theory results in equation (2.10), where the contributions of the plastic term is governed by the deviator stress tensor, S_{ij}.

$$d\varepsilon_{ij}^{t} = d\varepsilon_{ij}^{p} + d\varepsilon_{ij}^{e} = \frac{3}{2}\frac{d\varepsilon_{EQ}^{p}}{\sigma_{EQ}}S_{ij} + \left[\frac{(1-2\nu)}{3E}tr(d\sigma_{ij})\ I + \frac{dS_{ij}}{2G}\right] \tag{2.10}$$

2.3 Creep behaviour of materials

2.3.1 Overview

For temperatures above $0.3\ T_m$, for metals, the deformation of the material is enhanced because the energy associated with atomic vibration increases [55, 85]. This can cause time dependent deformations, i.e. creep can occur. Various mechanisms govern creep deformation at different temperatures. Below $0.35\ T_m$, dislocation slip processes take place, inducing a creep deformation which is governed by the stress applied to the material. The deformation generated by this mechanism due to dislocation motion encounters the resistance of obstacles, such as solute precipitates or other dislocations [85]. At temperatures in the range between $0.35\ T_m$ and $0.4\ T_m$, screw dislocations can move away from obstacles as a consequence of the *cross slip* mechanism, due to their increased energy level. When temperature is increased up to $0.6\ T_m$, diffusion is active in metallic crystals and, as a consequence, when a dislocation subjected to a stress field encounters an obstacle to its movement, e.g. a solute precipitate, the atoms of the dislocation in the proximity of the obstacle diffuse away from it. In this conditions, dislocations can *climb* over the obstacle, by the process called *creep recovery* [3, 85, 106, 107]. At temperatures above $0.8\ T_m$, creep occurs by diffusion within crystals, but this temperature range falls outside normal structural engineering applications [85].

Diffusion and dislocation climb generate time-dependent unrecoverable deformation, i.e. *creep deformation*, which represents one of the main effects of temperature increase on the mechanical behaviour of materials [3, 55, 63, 85].

Creep tests are generally carried out by applying a constant load to a conventional uniaxial test specimen, under high temperature conditions, and recording the variation of deformation with time [55].

Figure 2.6 is a typical creep curve obtained from a uniaxial creep test; it exhibits the characteristic time-dependency of the creep strain, ε^c, where the instantaneous deformation, ε_0, is either elastic or elastic-plastic and three different regions, characterising the creep response of the material, can be identified, i.e. primary, secondary and tertiary creep regions. In the primary creep region, strain hardening is the governing mechanism, and it is generated by the increase of dislocation density occurring when creep deformation takes place. At the same time, creep recovery, governed by diffusion, generates dislocation motion. In the secondary creep region, these two mechanisms balance each other and the creep strain rate is constant [3, 85, 107]. In the tertiary creep region, damage occurs in the material, leading to increasing creep strain rates and failure.

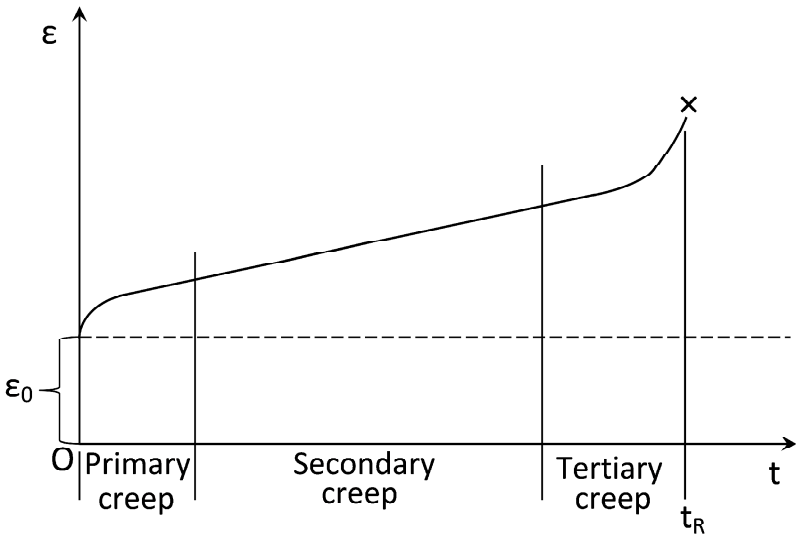

Figure 2.6: Typical creep curve. Adapted from ref [63], Fig. 1.4.

Creep deformation is governed by stress (i.e. loading conditions), temperature and time, as equation (2.11) (a) shows for a uniaxial stress field, where ε^c is the creep strain, σ is the stress and T is temperature [55, 63, 85]. A first, generally accepted, approximation is the separation of the three of effects, reported in equation (2.11) (b) [63, 85].

$$\varepsilon^c = f(\sigma, T, t) \tag{2.11a}$$

$$\varepsilon^c = f_1(\sigma) f_2(T) f_3(t) \tag{2.11b}$$

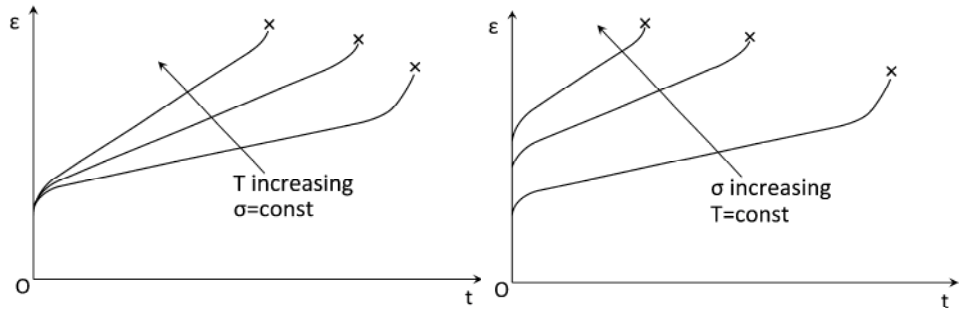

(a) (b)

Figure 2.7: Effects of (a) temperature and (b) stress on a typical creep curve. Adapted from ref [63], Figs. 1.6 and 1.7.

Figures (2.7) (a) and (b) show the effects of temperature and stress on the plot of creep strain versus time, respectively [63]. When σ and temperature increase, the instantaneous response of the material, ε_0, and the secondary creep rate increase, while the time to failure, t_R, decreases as Figure 2.7 (a) shows.

The influence of temperature on creep deformation can be modelled by an Arrhenius-type relation, represented by equation (2.12), where Q_c is the activation energy for creep and R is the Boltzmann constant [55, 85].

$$f_2(T) = exp\left[-\frac{Q_c}{RT}\right] \tag{2.12}$$

For constant temperature conditions, the dependency of creep deformation on stress and time can be described by the well known Bailey-Norton law, reported in equation (2.13), where *B*, *m* and *n* are material constants which depend on temperature. The Bailey-Norton equation is able to describe the primary and secondary creep regimes, without taking into account tertiary creep behaviour and creep rupture [55, 63, 85].

$$\varepsilon^c = B\sigma^n t^m \tag{2.13}$$

For relatively high stress levels, dislocation creep governs the time-dependent re-

sponse of the material and the stress exponent, n varies in the range from 3 to 10, while, for lower stress levels and higher temperatures, diffusion is the governing mechanism of creep deformation [3], and n is approximately 1 [3, 55, 106].

Equation (2.13) is valid for constant loads and temperature, while, under variable loading conditions, the creep behaviour of materials depends on the current state and its past history [55, 63]. In order to account for the effects of the past history on the creep material behaviour, two approaches may be followed: the time hardening and strain hardening procedures.

The time hardening formulation is obtained by differentiating equation (2.13) with respect to time, leading to equation (2.14). With this approach, the creep strain rate, in the primary and secondary creep regimes, is assumed to depend on temperature (through the material constants), the stress and time. Since the stress was not differentiated with respect to time, equation (2.14) is valid only for constant stress or step variations of the stress field with long duration [63].

$$\dot{\varepsilon}^c = Bm\sigma^n t^{m-1} \tag{2.14}$$

If time is eliminated in equation (2.14) by using equation (2.13), as equation (2.15) shows, the strain hardening formulation is obtained, reported in equation (2.16). In this formulation, which is also valid for constant stress or step variations of stress, the creep strain rate is taken to depend on stress, creep strain and temperature, while time does not explicitly appear as a variable in equation (2.16) [63].

$$t = \left[\frac{\varepsilon^c}{B\sigma^n}\right]^{\frac{1}{m}} \tag{2.15}$$

$$\dot{\varepsilon}^c = B^{\left(\frac{1}{m}\right)} m\sigma^{\left(\frac{n}{m}\right)} \left[\varepsilon^c\right]^{\left(\frac{m-1}{m}\right)} \tag{2.16}$$

The differences between the results obtained from these two approaches are due to procedural, rather than physical, reasons and, from comparison with experimental results, the strain hardening approach was found to be more accurate than time hardening [63].

2.3.2 Secondary creep approximation

In many industrial situations, components may be designed so that they do not exhibit excessive creep deformation, in order to avoid undesired interferences, such as in the case of gas turbine blades, where clearances are particularly critical [3]. For these scenarios, a useful assumption is provided by the *secondary creep approximation*, which takes the creep material behaviour to be governed by the constant creep strain rate regime (secondary creep region of Figure 2.6) [63]. Under this hypothesis, the strain is described by equation (2.17), where $\dot{\varepsilon}^c_{S-S}$ is the steady-state creep strain rate while ε_{in} approximates the instantaneous response, and it is obtained by extrapolating the constant creep strain rate curve to $t = 0$. Figure 2.8 is a schematic representation of the secondary creep approximation.

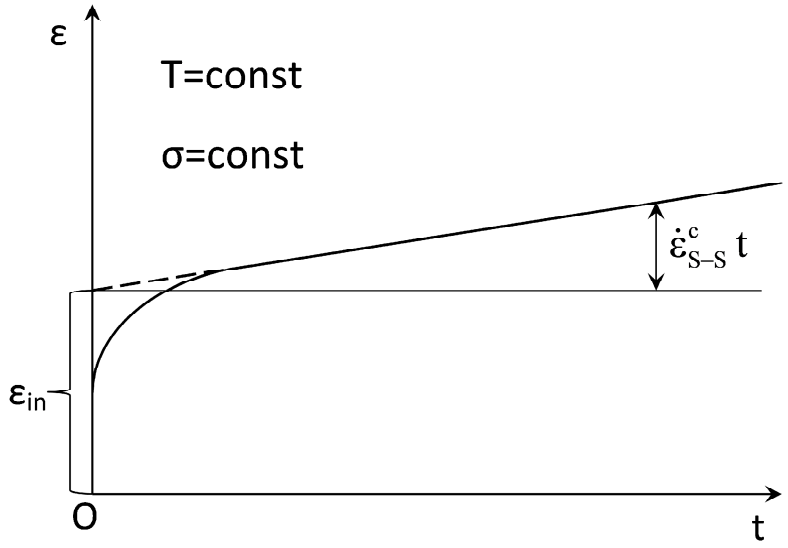

Figure 2.8: Secondary creep approximation. Adapted from [63], Fig. 2.6

$$\varepsilon(\sigma, T, t) = \varepsilon_{in}(\sigma, T, t) + \dot{\varepsilon}^c_{S-S}(\sigma, T)t \tag{2.17}$$

If a power law is chosen for the dependency of the secondary creep strain rate on the

stress level, the Norton law, reported in equation (2.18) in uniaxial form, is obtained, where *B* and *n* are material constants depending on temperature, as in equations (2.13)-(2.17).

$$\varepsilon^c = B\sigma^n t \tag{2.18}$$

When a solid body experiences creep deformation under a multiaxial stress condition, the formulation used to describe the dependency of the secondary creep strain rate on the stress must satisfy some conditions observed in experimental testing [63]:

- During creep deformation, the volume of the solid body is constant.
- The multiaxial model must reduce to the uniaxial equivalent formulation when a uniaxial stress field is described.
- The hydrostatic component of the stress tensor does not affect creep deformation.
- For isotropic materials, the principal directions of the creep strain and the stress are coincident.

In view of these requirements, equation (2.19), which is written in terms of creep strain rates in order to also account for the dependency of the creep response on the loading history, can be used for the multiaxial creep formulation. This equation is analogous to the plastic flow relation, see equation (2.10).

$$\dot{\varepsilon}^c_{ij} = \frac{3}{2}\frac{\dot{\varepsilon}^c_{EQ}}{\sigma_{EQ}} S_{ij} = \frac{3}{2} B\sigma^n_{EQ}\left(\frac{S_{ij}}{\sigma_{EQ}}\right) \tag{2.19}$$

2.3.3 Creep damage models

For those situations where the requirements of components are that rupture must be avoided during the operational life, such as high temperature pipework [3, 26, 47, 74], more sophisticated constitutive models, capable of predicting the behaviour of the material in tertiary

creep regime up to failure, should be adopted for modelling purposes [55, 71, 73, 81, 85].

During tertiary creep, the material undergoes deterioration processes, which are characterised by temperature and the stress field acting on the component. For relatively low temperatures ($T < 0.3\ T_m$) and high stress levels (near the yield stress), ductile creep rupture is the mechanism governing failure. In this situation, the deformation is mainly homogeneous, i.e. no significant strain concentration appears, and failure occurs by necking, similarly to the case of low temperature plasticity [85]. Ductile rupture is related to the changes of the global shape of the solid body because, under the effects of stress, dislocation glide causes distortion of the crystal, while the entropy (i.e. disorder) related to grain boundaries provides obstacles to dislocation motion [85].

When temperature increases ($0.4\ T_m < T < 0.6\ T_m$) and the stress is reduced, intergranular cavitation becomes the governing creep rupture process [71, 85]. In these conditions, diffusion has an important role in mass transportation, also by activating creep recovery deformation and vacancy migration [3, 85]. In this scenario, the higher entropy of grain boundaries generated by a less regular structure compared to that of the central regions of grains, enhances mass and vacancies transportation induced by diffusion. This generates high local stresses at grain boundaries, which become preferential sites for vacancies (as grains exhibit an approximately rigid body relative motion) producing micro voids nucleation, growth and their coalescence into macro-cracks [85]. When rupture is governed by intergranular cavitation, the component shows lower ductility than in the case of the of ductile creep rupture [85]. For temperatures higher than $0.6\ T_m$, mass transport by diffusion within grains is the governing deformation mechanism, and vacancies can move within grains as well. Furthermore, in this temperature range, ductile creep rupture becomes significant again [85].

Creep damage leads to a decrease of carrying load capability of the component or the tested specimen. As a consequence, under constant loading conditions, the stress acting on the undamaged ligament increases and, therefore, the creep strain rate increases.

Continuum damage mechanics (CDM) constitutive models take into account the evo-

lution and the effects of damage accumulation in the materials, in order to describe the tertiary creep regime and failure [71, 73, 85]. The material is assumed to be homogeneous, and its degradation is modelled by use of internal variables, ω_i (which cannot be directly measured), affecting the creep strain rate, as well as stress and temperature, see equation (2.20) [71, 73, 85]. Also, the evolution equations of the internal variables is specified in equation (2.21).

$$\dot{\varepsilon}^c = \dot{\varepsilon}^c(\sigma, T, \varepsilon^c, \omega_1, \omega_2, ..., \omega_n..) \tag{2.20}$$

$$\dot{\omega_i} = \dot{\omega_i}(\sigma, T, \varepsilon^c, \omega_1, \omega_2, ..., \omega_n..) \tag{2.21}$$

Equations (2.20) and (2.21) provide measures of micro-mechanical quantities related to material degradation, but they also show their effects on the macro-mechanical response of materials [71, 85, 95]. Furthermore, these models do not specifically describe a particular damaging mechanism and are not based on direct micro-mechanical observations, but they predict the effects of the global damage accumulation on the bulk creep response and are obtained by a phenomenological approach, fitting experimental results [71]. However, in more recent, mechanism-oriented, multivariable CDM models, each internal variable is related to a damage micromechanism [71].

The first creep damage model was proposed by Kachanov (1958) and Rabotnov (1969), to predict the rupture behaviour of metals for high temperature applications, and it was extended to a multiaxial formulation by Leckie and Hayhrust (1977) [71, 73, 85]. The model is reported in equations (2.23)-(2.25), where the damaged internal variable, ω, represents the damaged material fraction. This variable is defined by equation (2.22), where Ω and Ω_0 are the undamaged area of material and the initial section, respectively, and it ranges from 0, for undamaged material, to its critical value, $\omega_{MAX} = 1$, for the completely damaged configuration; σ_{RUP} is the rupture stress and A_{KR}, B_{KR} χ, f, n_2 and α_D are material constants, with α_D taking into account the effects of the stress multiaxiality [55, 71, 73, 85].

$$\omega = 1 - \frac{\Omega}{\Omega_0} \tag{2.22}$$

$$\dot{\varepsilon}_{ij}^{c} = \frac{3}{2} B_{KR} \left(\frac{\sigma_{EQ}}{1-\omega} \right)^{n_2} \frac{S_{ij}}{\sigma_{EQ}} \tag{2.23}$$

$$\dot{\omega} = A_{KR} \frac{\sigma_{RUP}^{\chi}}{(1-\omega)^{f}} \tag{2.24}$$

$$\sigma_{RUP} = \alpha_D \sigma_1 + (1 - \alpha_D)\sigma_{EQ} \tag{2.25}$$

In the Kachanov-Rabotnov (KR) damage model, since the damaged material does not carry any load, the effective stress σ_{EFF}, acting on the undamaged ligament, is given by equation (2.26), where σ is the nominal stress (in uniaxial conditions). The strain generated by the effective stress on the effective configuration (which does not exhibit any voids or cracks) is the same as that generated by homogenised stresses on the damaged configuration [85, 95].

$$\sigma_{EFF} = \frac{\sigma}{1-\omega} \tag{2.26}$$

Applications of the KR constitutive model show that it is capable of accurately predicting the secondary and tertiary creep response of metals and it has been successfully adopted in numerical finite element (FE) calculations for component assessment and material characterisation [50, 51, 56, 68, 71–73]. Despite of the capabilities of predicting tertiary creep and rupture, during FE analyses, difficulties in the convergence process were found when the damage variable approaches unity [50]. The difficulties are caused by the singular behaviour of $\dot{\varepsilon}_{ij}^{c}$ and $\dot{\omega}$ when $\omega \rightarrow 1$, as equations (2.23) and (2.24) show, which is also related to the high stress sensitivity of this constitutive model [49–51, 68, 73].

In order to overcome the convergence problems encountered in numerical analyses, especially for the local approach in fracture mechanics investigations, Liu & Murakami [50, 73] proposed a constitutive model which eliminates the singularities characterising the KR equations when the damage variable approaches its critical value. Their model is reported in equations (2.27) and (2.28), with σ_{RUP} defined by equation (2.25) [55, 73] and A_{LM}, B_{LM}, n_3 and χ_2 material properties.

$$\dot{\varepsilon}^c_{ij} = \frac{3}{2} B_{LM} \sigma^{n3}_{EQ} \frac{S_{ij}}{\sigma_{EQ}} exp \left[\frac{2(n_3+1)}{\pi \sqrt{1+\frac{3}{n_3}}} \left(\frac{\sigma_1}{\sigma_{EQ}} \right)^2 \omega^{\frac{3}{2}} \right] \tag{2.27}$$

$$\dot{\omega} = A_{LM} \frac{1 - exp[-q_2]}{q_2} \sigma^{\chi_2}_{RUP} exp[q_2 \omega] \tag{2.28}$$

Equations (2.27) and (2.28) were obtained by extending the constitutive model proposed by Hutchinson (1983) [39, 73] for dilute cracks concentration to the non-dilute case, by using the self-consistent method [90]. This led to the use of the exponential function in equation (2.27), which generates a finite creep strain rate when $\omega \rightarrow 1$. Furthermore, equation (2.28) shows that, when the damage parameter approaches its upper bound, also the damage rate is finite.

It should be noted that, for the undamaged material, i.e. with $\omega = 0$, equations (2.23) and (2.27) lead to the secondary creep strain rate, therefore the coefficients B_{KR} and B_{LM} are equal to the strain multiplier, B, of Norton's creep law, while n_2 and n_3 are equal to the Norton stress exponent, n, see equation (2.19).

Furthermore, when equations (2.24) and (2.28) are integrated between the beginning of the analysis, $t = 0$, corresponding to $\omega = 0$, and and failure, $t = t_R$, corresponding to $\omega = 1$, equations (2.29) and (2.30) are obtained, respectively. These equations show that, in equations (2.24) and (2.28) A_{LM} equals $A_{KR}(f+1)$ and $\chi_2 = \chi$.

$$\int_0^1 (1-\omega)^f d\omega = A_{KR}\sigma_{RUP}^{\chi}\int_0^{t_R} dt \implies t_r = \frac{1}{A_{KR}(f+1)\sigma_{RUP}^{\chi}} \tag{2.29}$$

$$\int_0^1 exp[-q_2\omega]d\omega = \frac{A_{LM}\sigma_{RUP}}{q_2}[1-exp(-q_2)]\int_0^{t_R} dt \implies t_r = \frac{1}{A_{LM}\sigma_{RUP}^{\chi 2}} \tag{2.30}$$

2.4 Effects of plasticity on creep behaviour of metals

Many components and structures, operating at high temperature, are subjected to plastic deformations, caused by the loading conditions, together with creep. Examples of these situations can be found in power plants, where high temperature components can be in pre-strained conditions, or they can be subjected to plastic strains under low temperature operational conditions and creep at high temperature. Also, components of aero engine turbines experience thermal and mechanical loading cycles, which can induced plastic deformations, due to the stress field, and creep [66]. In addition, local plastic strains can also be caused by welding processes carried out on thick-section components because of the constraint effects caused by the material surrounding the weld [107]. Small punch creep test specimens provide another example of structures where plasticity takes place together with creep deformation.

The effects of plastic deformation (taking place either at low or high temperature) on creep properties of materials are of practical and theoretical interest, as they can lead to improvements in the performances of power plants, by the development of an optimised pre-straining procedure, and they can provide information about the mechanisms governing deformation and damaging processes during high temperature creep. Several experimental studies have been carried out on steels and non-ferrous materials, and different effects of prior inelastic deformation on subsequent creep properties of materials were reported in the open literature [66].

Willis et al. [104, 107] investigated the effects of pre-straining on the creep response of 316H stainless steel in partially-solution treated (PST) and fully-solution treated (FST) conditions, and of FST 316L stainless steel, at 575°C [104, 107]. The 316H specimens were machined from an in-service power plant component. Standard uniaxial creep tests were carried out, with a stress, σ, of 450 [MPa] on as-received specimens and room temperature pre-strained specimens, with pre strain level, ε_P, ranging from 0 to 0.39 for PST material and from 0 to 0.20 for FST material.

Figure 2.9 is the plot of the initial strain versus pre-straining level for FST and PST 316H stainless steel [107].

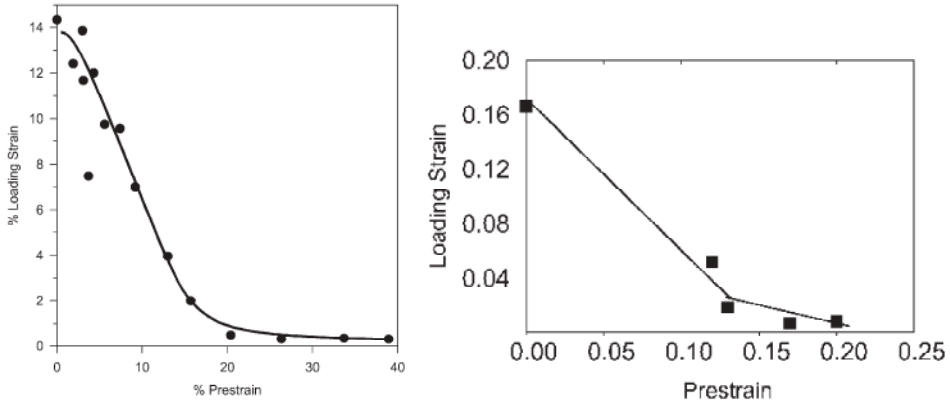

(a) (b)

Figure 2.9: Initial strain plotted versus pre-strain level for (a) PST 316H stainless steel, with σ=450 [MPa] (ref. [104], Fig. 1) and (b) and FST 316H stainless steel with σ=360 [MPa] (ref. [107], Fig. 4(a)), both tested at 575°C.

Plastic deformation, prior to the constant-stress creep tests, increased the dislocation density within the material, generating barriers to further dislocation motion and plastic flow. The first effect of the dislocation density increase is the reduction of the strain level obtained by applying the test load, i.e. the loading strain, as Figure 2.9 shows [104, 107].

For constant stress creep tests, when the loading strain had no plastic component as a consequence of room temperature pre-straining, the creep behaviour of 316 stainless steel was found to be remarkably modified [104, 107]. A drastic reduction in the creep ductility and the minimum creep rate, was observed for both PST and FST 316 stainless steels, while the failure time was found to decrease for PST conditions and to increase for

the fully treated material [104, 107]. Figure 2.10 shows the creep curves of PST and FST 316H stainless steel with different pre-strain levels [66, 104, 107].

A similar variation of the creep curve, after room temperature pre-straining, was also observed by Wilshire and Palmer for polycrystalline copper [105, 107].

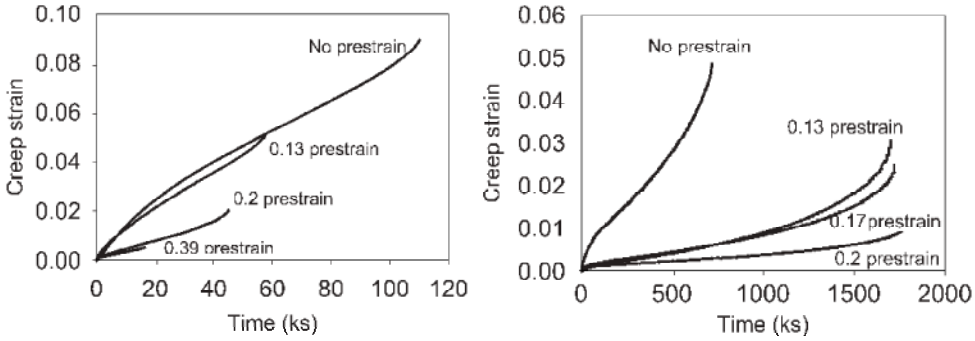

Figure 2.10: Creep curves for room temperature pre-strained (a) PST 316H stainless steel, with a stress of 450 [MPa] and (b) FST 316H stainless steel with σ=360 [MPa], both tested at 575°C. Ref. [107], Figs. 1 and 2, respectively.

Wilshire and Willis [107] also reported the effects of high temperature pre-straining on the subsequent creep behaviour of 316L stainless steel at 575°C. An initial stress of 360 [MPa] was applied for 15 [sec] and, subsequently, the test was continued until rupture with a stress of 340 [MPa]. Immediately after the load reduction, the creep rate became extremely low and, after that, it increased to a value similar to the minimum creep strain rate observed during a constant stress creep test at 340 [MPa]. This indicates that, when prior creep deformation was applied at high temperature, the primary creep region was replaced by an 'inverse creep' behaviour, i.e. the creep strain rate increased instead of decreasing to its minimum value, in contrast with the behaviour observed when room temperature pre-straining was carried out. Inverse creep immediately after the load reduction was also observed when the stress of 360 [MPa] was hold until the minimum creep strain rate was reached [107]. Figure 2.11 shows the plots of the creep strain rate versus creep strain for a FST 316L stainless steel at 575°C, with the two of creep pre-straining procedures adopted by Wilshire and Willis [107].

For not pre-strained material, in the testing conditions reported in ref. [107], the pri-

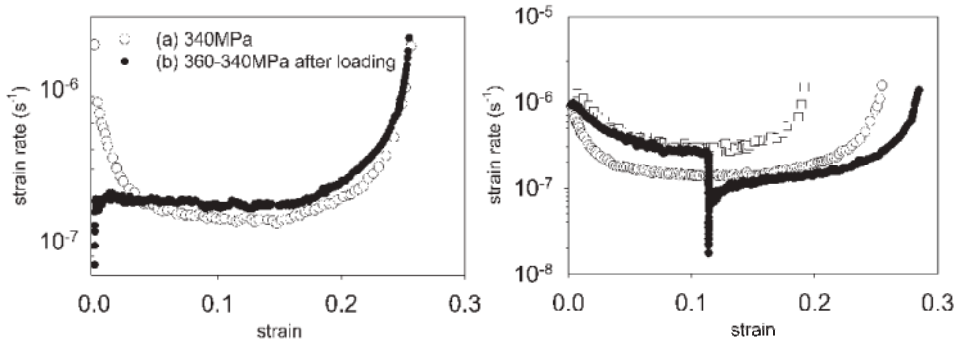

(a) (b)

Figure 2.11: Creep rate plotted versus creep strain for a FST 316L stainless steel, tested at 575°C with a stress of 340 [MPa] after creep pre-straining at 360 [MPa] for (a) 15 [sec] and (b) for the time to reach the minimum creep rate. Ref. [107], Figs. 9 and 11, respectively.

mary creep region, characterised by strain rate decrease, is mainly governed by strain hardening caused by the dislocation density increase with creep strain. Creep recovery also takes place, and dislocations can rearrange into a lower energy configuration, see also Section 2.3.1 [3, 85, 107].

In the case of a pre-crept material, immediately after the stress reduction from 360 to 340 [MPa], dislocations encounter obstacles created at a stress of 360 [MPa], which are stronger barriers than those obtained with a stress of 340 [MPa]. This causes a sudden drop of the creep rate, as shown in Figure 2.11. The creep rate then increases as a consequence of creep recovery, which gradually removes the effects of the previous higher stress state, i.e. the stronger barriers to dislocation motion and creep deformation. As a result, the creep strain rate approaches that obtained with a stress of 340 [MPa] without pre-straining [107].

In contrast, when the material is pre-strained at room temperature, the main dislocation mechanisms are not influenced by pre-strain for all of the tests. The barriers to dislocation motion are stronger than in the case of as-received material, and, as a consequence of strain hardening and creep recovery, the typical primary creep region, with a decreasing creep strain rate, takes place [107].

Mehmanparast et al. reported the effects of a plastic pre-compression $\varepsilon_p = -0.08$, carried out at room temperature, on the creep response of 316H stainless steel removed

from ex-service power station steam header components manufactured from different casts of material and exposed to different previous service conditions [79]. Mehmanparast and co-workers showed that, as a consequence of pre-compression, the yield stress of 316H stainless steel increased and, for a constant stress level, the loading strain decreased with pre-compression, similarly to the effects of room temperature pre-tension reported in refs. [104, 107]. The results of uniaxial creep tests, performed at 550°C with stress ranging between 257 and 335 [MPa], showed that the minimum creep rate was not remarkably affected by the amount of pre-compression, while the creep ductility of pre-compressed material, measured by the axial creep strain at failure and by the reduction of the cross sectional area at the failure location, significantly decreased [79]. Also, the average creep strain rate, did not considerably change with pre-compression. Figure 2.12 shows the plots of the engineering strain, at failure, versus the stress and of the average creep strain rate versus the stress (both on logarithmic scales) for two casts of material taken from different components, [79].

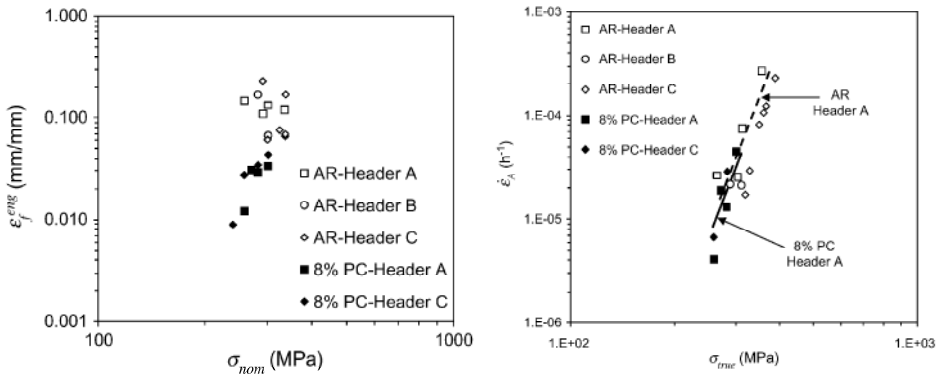

(a) (b)

Figure 2.12: Effects of pre-compression on 316H stainless steel. Plots of (a) axial strain at failure versus stress and of (b) average creep strain rate versus stress for pre-compressed (PC) and as-received (AR) material taken from different components (Header A and C). Ref. [79], Figs. 3a and 4, respectively.

The behavoiur of 316 stainless steel was also investigated by Hyde [43] who reported the results of plasticity/creep tests performed at 550°C by applying a creep load to the specimens and overloading for 3 [sec] at regular time intervals of 168 [h]. Plastic strain was accumulated during the short overloading periods while creep deformation increased during the constant load intervals between the overloads [43]. An anomalous creep behaviour was observed for the tests performed at 550°C with constant stresses lower than 320 [MPa], i.e.

without overloading, which exhibited renewed primary and secondary creep regions (with an increased minimum creep rate). Hyde suggested that the anomalous behaviour can be related to creep recovery [43, 44]. The results of plasticity/creep tests showed standard creep curves, with primary, secondary and tertiary regions, for any base creep stress, because of the increase of dislocation density, induced by the overloads, inhibiting recovery processes and the anomalous behaviour [43].

During plasticity/creep tests, the primary creep region was not sensibly affected by high stress overloads, while creep ductility, represented by the creep strain at failure, decreased because high dislocation density, generated by the overloads, increased the strength of the barriers to dislocation motion [43]. The failure time was not remarkably affected by the overloads when the increase in stress, produced by overloading, was of 100 [MPa] or less, while, it significantly decreased when an overload stress increase of 140 [MPa], or more, was applied. Furthermore, Hyde reported that failure occurred during the creep strain accumulation periods for low overload levels and during one of the short overload periods for relatively high overloads [43].

Kikuchi and Ilschner [58] reported the effects of high temperature pre-straining on primary and steady-state creep behaviour of AISI 304 stainless steel at 600°C. Uniaxial specimens were pre-strained up to a 4.5% elongation at different temperatures, i.e. 650, 700 and 750°C, with a normalised stress equal to $\sigma/G = 4.1 \times 10^{-3}$ (where G is the shear modulus) and, then, they were cooled to 600°C to be creep-tested at the same normalised stress used for pre-straining. A creep resistance behaviour was found for all of the pre-straining conditions, and the secondary creep rate was reduced by about 50% when a prior deformation of 4.5% at 700°C was applied. In the primary creep region, the creep rate decreased when the pre-strain level increased, while the duration of the primary creep regime was shortened. The inverse primary creep region produced by stress reduction at high temperature, reported in ref. [107], was not observed for AISI 304 steel [58], and typical primary creep region, characterised by decreasing creep rate, was found. The normalised stress used for pre-straining is the same as that of creep testing, therefore the strength of the barriers to dislocation motion generated during pre-straining is not higher than that of creep tests.

The creep resistance effects of high temperature pre-strain, observed for AISI 304 stainless steel, are due to changes in the dislocation substructure generated by prior deformation and carbide precipitation enhancement (caused by thermal ageing) [58]. The material did not show a variation of sub-grain size, but the dislocation structure of the pre strained specimens was found to be more regular than that of as-received specimens, causing a reduction of the primary creep strain and of the secondary creep rate. Figure 2.13 shows the effects of high temperature pre-straining on the creep response of AISI 304 stainless steel [58, 66].

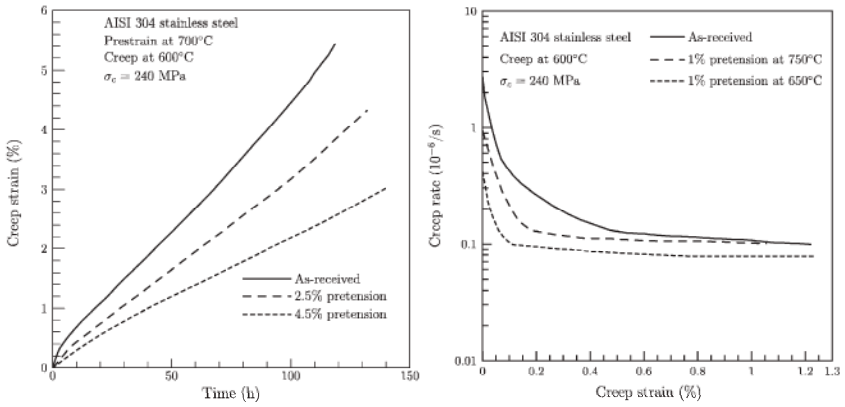

(a) (b)

Figure 2.13: Effects of high temperature pre-straining on (a) the variation of creep strain versus time (ref. [66], Fig. 3) and (b) the variation of creep strain rate versus creep strain (ref. [66], Fig. 4).

Under different pre-straining conditions, a creep enhancement effect, i.e. an increase of creep strain rate, was observed for various materials. Tai and Endo [66, 101] investigated the creep behaviour of 2.25Cr-1Mo steel at 600°C after creep pre-straining at high temperature. The effects of pre-straining on the minimum strain rate were quantified, by Tai and Endo, by using the *degradation parameter*, ϕ, defined by equation (2.31), where $\dot{\varepsilon}^c_{min,p}$ is the minimum creep strain rate of pre-strained material, $\dot{\varepsilon}^c_{min,0}$ is the minimum creep rate of the as-received material [101]. When the material exhibits creep enhancement after pre-straining, ϕ os grater than 1, as in the results reported in ref. [101], while for creep resistance effects, ϕ is less than 1 [101].

$$\phi = \frac{\dot{\varepsilon}^c_{min,p}}{\dot{\varepsilon}^c_{min,0}} \tag{2.31}$$

For 2.25Cr-1Mo steel, the deterioration of the material was shown to be dependent on the stress and the pre-strain level [101]. The creep pre-strain applied to the material ranged between 0.14 % and 19.4 %, with a stress level between 78.4 and 127.4 [MPa]. After creep pre-straining, the load was released for 1 [h] and, then, a stress of 98 [MPa] was applied to perform the creep tests [101]. A creep enhancement effect was observed for all of pre-straining conditions, i.e. the creep strain rate of pre-crept material was found to be higher than that of the as-received material. Tai and Endo also suggested a relation between the deterioration parameter, ϕ, and the pre strain level, ε_p reported in equation (2.32), where L_T and M_T are constants determined by the best fitting of experimental data [66, 101]. Figure 2.14 is the plot of the variation of the degradation parameter, ϕ, versus the creep pre-strain level, for different pre-straining stresses [66, 101].

$$\phi = L_T(\varepsilon_p + 1)^{M_T} \tag{2.32}$$

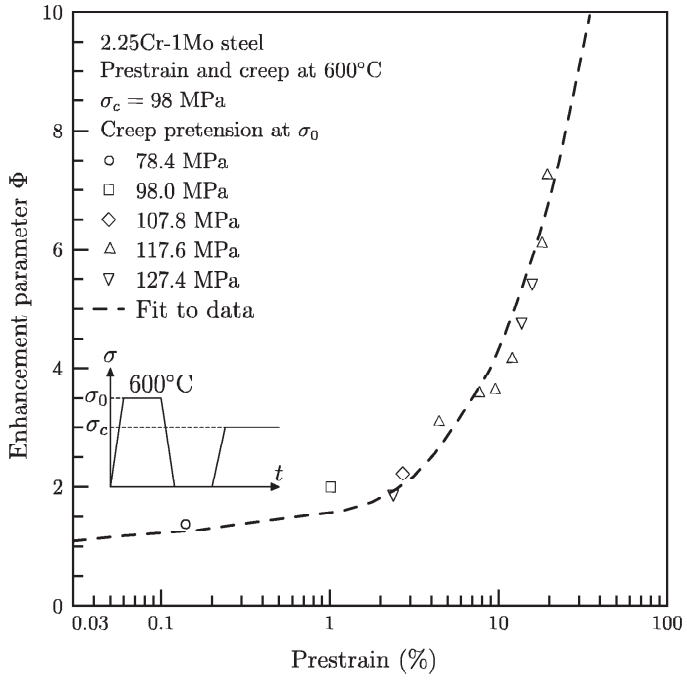

Figure 2.14: Variation of ϕ versus creep pre-strain level for a 2.25Cr-1Mo steel at 600°C. Ref. [66], Fig. 10.

When the stress applied during creep pre-straining was the same as that of creep tests, i.e. an interrupted test was performed, and the prior creep deformation is approximately 1%,

the creep rate obtained for pre-strained specimens was found to be approximately twice than that of the as-received material [101].

The influence of the creep test stress on ϕ was investigated by Tai and Endo and the dependency of the degradation factor on the normalised creep stress is given by a power law, reported in equation (2.33), where σ_ϕ is a reference creep stress, ϕ_0 is the degradation parameter, corresponding to σ_ϕ, A_{TE} and k_{TE} are material constants [101].

$$\phi = A_{TE}\phi_0 \left(\frac{\sigma}{\sigma_\phi}\right)^{k_{TE}} \tag{2.33}$$

Chanduri and Ghosh [15] analysed the effects of room temperature plastic pre-straining on the subsequent creep behaviour of 2.25Cr-1Mo steel tested at temperatures ranging between 500 and 600°C. They observed that room temperature pre-straining induced a reduction of the minimum creep strain rate (creep resistance behaviour), because of dislocation density increase [15]. Figure 2.15 is the plot of creep strain versus time for a 2.25Cr-1Mo steel at 550°C, with different levels of room temperature pre-strain and it shows the decrease in the minimum creep rate and the increase in failure time with a pre-straining level increase [15].

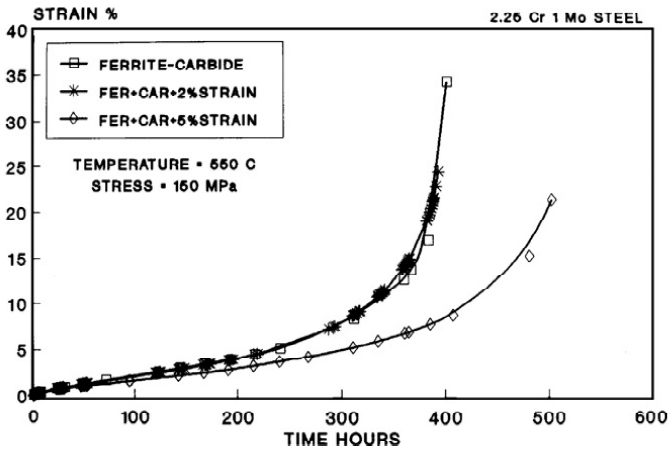

Figure 2.15: Effects of room temperature plastic pre-straining on the creep behaviour of 2.25Cr-1Mo steel at 550°C. Ref. [15], Fig. 5.

The effects of room temperature pre-straining on the creep behaviour of Ti834 tita-

nium alloy were investigated by Whittaker et al. [103]. The Ti834 alloy is a near α titanium alloy which exhibits remarkable material properties up to 630°C, and it is used for gas turbine applications [103]. Whittaker et al. reported that, when this alloy was pre-strained, a creep enhancement effect was observed, since the minimum creep rate increased, while the time to failure and the strain at failure decreased [103]. Figure 2.16 is the plot of creep strain versus time for a Ti834 titanium alloy tested at 600°C with a stress of 400 [MPa], for different pre-strain levels [103]. Furthermore, the effects of a compressive pre-straining of -1.25%, on the minimum creep strain rate are similar to those obtained by applying a tensile pre-straining of 1.25%, but the onset of tertiary creep is delayed for the case of compressive pre-strain (see figure 2.16).

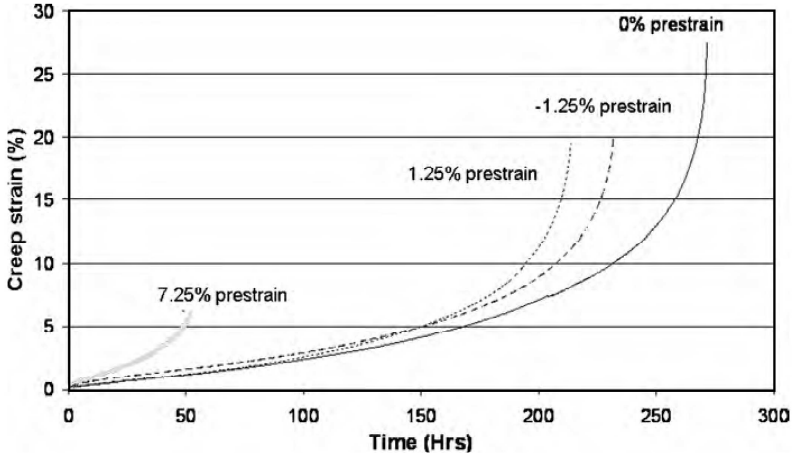

Figure 2.16: Effects of pre-straining on the creep behaviour of Ti834 titanium alloy at a temperature of 600°C with σ=400 [MPa]. Ref. [103], Fig. 7.

Creep enhancement effects were reported by Loveday and Dyson [66, 75] for IN597 nickel based super-alloy at 800°C and by Pandey et al. [66, 83] for Inconel alloy X-750 at 750°C.

The viscoplastic behaviour (with small plastic strains) of P91 and P92 steels, has been investigated by Saad et al., and the material constants for the Chaboche unified viscoplasticity model were obtained, for thermo-mechanical fatigue applications [92]. However, in the open literature, studies on the effects of plastic pre-strain, applied at high stress levels and high temperature, on the creep response of 9Cr steels, such as P91 steel, are rare.

2.5 Small specimen testing techniques

2.5.1 Overview

As reported in Chapter 1, the need for material creep testing has become of high importance over the last few decades [42, 56]. These needs have been driven by the aerospace and power generation industries. An aspect is the need for material testing where only small amounts of material are available for assessment [42, 52, 53, 91, 97, 98, 108]. This includes non-destructive evaluation of in-service components, especially when the removal of material could significantly impair the structural integrity of the component [21], the characterisation of the HAZ of welds [34, 111], the development of new alloys [91] and, in the nuclear industry, problems related to the handling of active materials [56]. In these situations, it may not be possible to use conventional full-size specimens, and innovative techniques, adopting miniature specimens, have been developed [42, 46, 52, 53, 55, 56]. Two main categories of miniature specimens have been developed to date [56]:

- Miniature samples which are similar in shape similar to conventional specimens, but smaller in sizes.
- Miniature samples specifically designed to benefit from their reduced dimensions.

For creep testing, the first category of miniature specimens (those with shapes similar to those of conventional samples) generally includes uniaxially loaded samples with a total length of approximately 50 [mm], a gauge length of 25 [mm] and a diameter of 8 [mm] [56]. The experimental results obtained from small sized uniaxial specimen tests can be easily compared with results obtained from conventional creep test specimens including rupture data e.g. [42]. Alternatively, in cases where the material available is limited in size, single sections of the specimen can be separately manufactured and subsequently joined together by use of electron beam welding, causing a relatively expensive and not trivial manufacturing process [42, 56].

The second category of specimens includes samples characterised by a variety of shapes. These are designed so that they require relatively simple and economic manufacturing processes. These specimens can be manufactured from scoop samples, usually with approximate dimensions of 30×20×3 [mm], as shown in Figure 2.17, [41, 42, 98], which can be taken from in-service components [42].

Small sample testing techniques currently used include:

- Impression creep testing
- Small ring specimen creep testing
- Two bar specimen creep testing
- Small punch creep testing

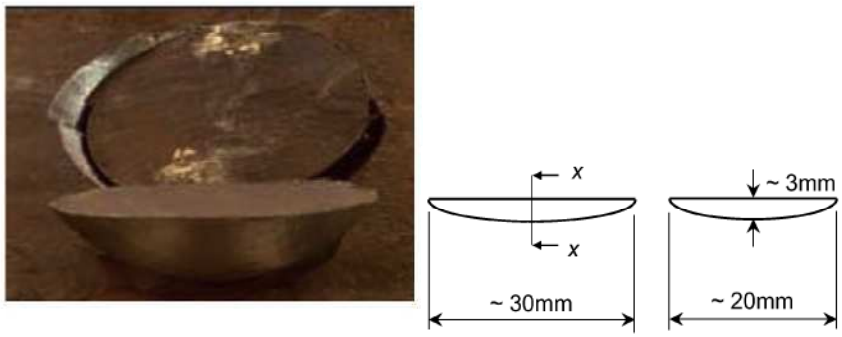

Figure 2.17: (a) Scoop sample taken from an in-service power plant component (ref. [42], Fig. 2 (b)) and (b) its dimensions (ref. [42], Figs. 2 (c) and (d)).

These techniques have the advantage of requiring the testing of very small samples. However, conversion procedures to relate the output from experimental tests to that of the more useful standard uniaxial creep tests are needed [45, 55, 56].

A technique which may be used to convert the results of non-conventional testing to those of standard full size uniaxial tests is the inverse *reference stress method* (RSM) [51–55]. By using this approach, the deformation rate due to creep of a specific point of a structure, or a specimen, can be related to the creep strain rate of a uniaxial creep test carried

out at a reference stress, σ_{REF} [51, 55, 85]. For a material which obeys the Norton creep law, with stress exponent and multiplier represented by *n* and *B*, respectively, the displacement rate, $\dot{\Delta}$, of the point of interest can be related to the creep material properties, the geometry of the structure (through the dimensions) and a suitably defined nominal stress, σ_{NOM}, by equation (2.34) [51].

$$\dot{\Delta} = f_1(n) f_2(\text{dimensions}) B(\sigma_{NOM})^n \tag{2.34}$$

A constant, η, can be defined such that $f_1(n)/(\eta^n)$ does not vary with *n*. Therefore, the deformation rate can be related to the creep strain rate of the reference uniaxial test by use of equation (2.35), where σ_{REF} is the reference stress defined by equation (2.36), *s* is a characteristic dimension of the structure analysed and the *D* constant is the equivalent gauge length of the structure [51].

$$\dot{\Delta} = DB(\sigma_{REF})^n = \beta s B \sigma_{REF}^n = \beta s \dot{\varepsilon}^c(\sigma_{REF}) \tag{2.35}$$

$$\sigma_{REF} = \eta \sigma_{NOM} \tag{2.36}$$

Since $D = f_1(n) f_2(\text{dimensions})/(\eta)^n$ is, by its definition, independent of *n*, then also $\beta = D/s$, defined by equation (2.37), does not depend on the material properties. When an analytical expression is available for $\dot{\Delta}$, the value of the stress multiplier α, for which the normalised displacement rate reported in the left hand side of equation (2.37) is practically independent of n, is the reference stress parameter η. Once η is obtained, the β parameter is obtained by equation (2.37) the and the deformation of the structure can be converted into the corresponding uniaxial creep test data e.g. [52].

$$\frac{\dot{\Delta}}{sB(\alpha\sigma_{NOM})^n} = constant = \beta \tag{2.37}$$

In those situations where an analytical solution is not available, the conversion parameters can be obtained by use of numerical techniques, such as the finite element (FE) method.

2.5.2 Impression Creep Test

Use of the impression creep test method was first reported in 1977, by Chu and Li [17], for testing of a molecular crystal which exhibited creep behaviour at room temperature, and, then, it was used for testing of several materials, such as the HAZ of P91 welds [53], 316 stainless steel, 0.5Cr-Mo-V steel [52], magnesium alloys [86] or solid fuel for the nuclear industry [64]. Impression creep testing was also used under stepped load or stepped temperature conditions, in order to investigate the creep response of the material, at different stresses or temperatures, using a single specimen in each case [98].

The test is performed by applying a constant load to a flat-ended indenter in contact with the specimen. The variation of the punch displacement with time is recorded and it constitutes the experimental output of the test. It exhibits an initial deformation, related to the loading level, followed by the time dependent behaviour caused by creep. The impression creep curve is characterised by a decreasing deformation rate region and a stationary region, where the deformation rate is constant [53, 54, 67, 97, 98]. Figure 2.18 shows a plot of indenter displacement versus time for impression creep tests performed on a P91 steel at 650°C and on a molecular crystal at 37°C.

The impression creep deformation curve is related to the primary and secondary creep properties of the tested material in the vicinity of the contact region between the specimen and the indenter. Due to the compressive stress field which is produced in the specimen during the test, the material does not exhibit creep damage, and therefore, tertiary creep behaviour cannot be investigated by using this testing technique [86, 98]. However, Rashno et al. [86] reported that magnesium alloy MRI153 exhibited an increase of the displacement rate curve when impression creep tested at 217°C and they related this behaviour to carbide coarsening or precipitate dissolution.

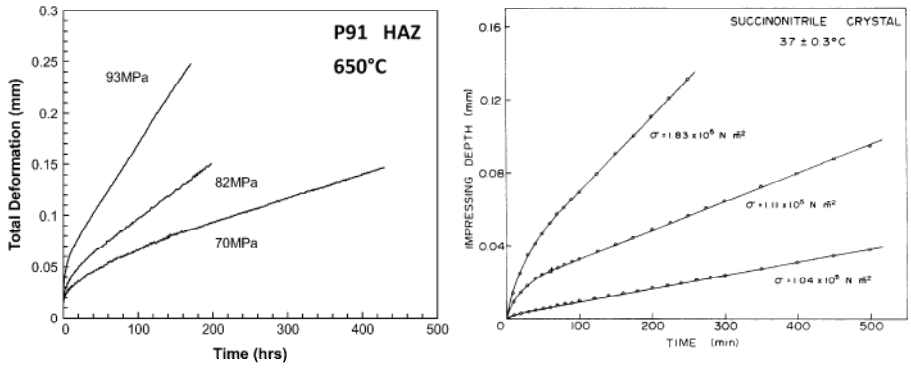

(a) (b)

Figure 2.18: Impression creep curves for (a) the HAZ of a P91 steel weld tested at 650°C with different stress levels, ranging from 70 to 93 [MPa], (adapted from ref. [52], Fig.2(a)) and (b) the molecular crystal reported by Chu and Li in ref. [17] (adapted from ref. [67], Fig.3).

The localised nature of deformation which occurs in an impression creep test is apparent from the microscope images shown in Figure 2.19. The microstructural configuration, after impression creep testing, of two different specimens made of MRI153 magnesium alloy and 316LN stainless steel, respectively, are shown [82, 86]. In these two specimens, three regions can be identified. The region closest to the indenter, indicated in Figure 2.19 (a) as zone 1, is characterised by a hydrostatic stress field as it shows no significant distortion of grains. In the region close to the edge of the indenter, i.e. zone 2 of Figure 2.19 (a), there is significant shear deformation which causes distinct grain distortion. The test loading conditions did not affect the shape of grains in both of the specimens in the remote region (zone 3 of Figure 2.19 (a)), indicating that no significant plastic deformation occurred at that location [82].

It is generally considered that the contact area between the indenter and the specimen must be relatively large compared to metallurgical features, in order to obtain bulk creep properties of the material investigated and to avoid size effects which can affect the experimental results when less than 6-10 grains are covered by the effective section of the specimen, i.e. the contact area with the indenter [52, 54]. In view of this requirement, Hyde et al. recommended the use of rectangular indenters for impression creep tests in order to increase the contact area, and also the load level, with respect to the case of a cylindrical indenter [52, 54]. Figure 2.20 shows the configuration of an impression creep test with a

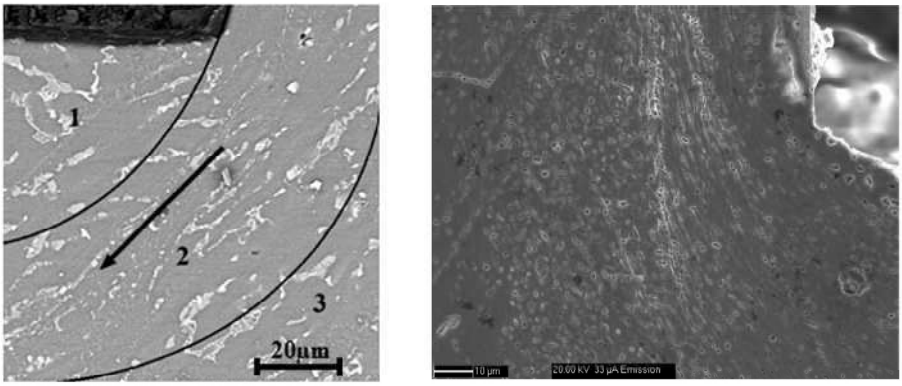

(a) (b)

Figure 2.19: Microstructure of impression creep specimens near the contact region with the indenter. The materials tested are (a) a magnesium alloy (adapted from ref. [86], Fig.4) and (b) a 316LN stainless steel (adapted from ref. [82], Fig.10 (b)).

rectangular indenter and the geometry and of a square specimen, used in the work reported in refs. [52, 54], where w_i, b_i, h_i, are the width, the length and the thickness of the specimen, respectively, and d_i is the thickness of the indenter, while $\bar{p}$ is the average contact pressure between the indenter and the specimen, defined in equation (2.38), with *P* representing the indentation load.

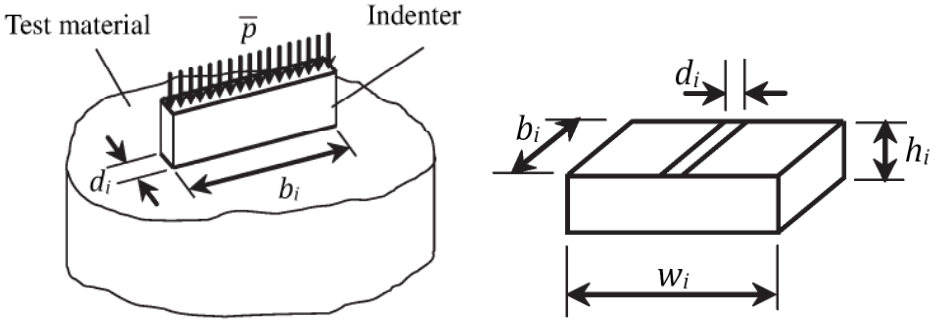

(a) (b)

Figure 2.20: Geometry recommended by Hyde et al. with (a) rectangular indenter(adapted from ref. [52], Fig.1 (a)) and (b) square specimen (adapted from ref. [52], Fig.1 (c)).

$$\bar{p} = \frac{P}{b_i d_i} \tag{2.38}$$

The geometry of the test set-up represented in Figure 2.20 is defined by the $\frac{w_i}{d_i}$, $\frac{w_i}{b_i}$ and

$\frac{h_i}{d_i}$ ratios, with $w_i = b_i$ =10 [mm], d_i =1 [mm] and h_i =2.5 [mm] for the configuration used in refs. [52, 54]. The square specimen can be manufactured from a scoop sample, similar to that shown in Figure 2.17, and it is large enough to ensure that full contact with the punch and the support is maintained during the creep test [52]. This prevents significant bending deformation of the specimen and therefore the displacement of the indenter is caused only by creep occurring in the localised region of the specimen close to the area of contact with the indenter [98].

If the material is assumed to obey Norton's creep law (equation (2.18)), the conversion relationships between impression creep test output and uniaxial creep test data can be obtained by use of the reference stress method, which is briefly described in Section 2.5.1. The reference stress, σ_{REF}, is related to the mean pressure, $\bar{p}$, by equation (2.39) while the steady-state displacement rate, $\dot{\Delta}_{s-s}$ is related to the strain rate of the corresponding uniaxial creep test, $\dot{\varepsilon}^c(\sigma_{REF})$, by equation (2.40).

$$\sigma_{REF} = \eta\bar{p} \tag{2.39}$$

$$\dot{\Delta}_{s-s} = DB(\eta\bar{p})^n = \beta d_i B(\sigma_{REF})^n \tag{2.40}$$

Since an analytical solution is not available for $\dot{\Delta}_{s-s}$, a series of FE analyses is needed to obtain the displacement rate for various values of the stress multiplier, *n*. The η parameter is then calculated by plotting the normalised displacement rate $\frac{\dot{\Delta}}{d_i B(\alpha\bar{p})^n}$ versus *n*, as shown in Figure 2.21, and the value of the stress multiplier α for which the normalised displacement rate is constant is the η parameter. The β parameter is calculated by extrapolating the intercept of the normalised $\dot{\Delta}$ for *n*=0.

The reference stress parameters depend on the geometry of the experimental set-up and are independent of material properties. The correlation between impression creep test results and secondary creep uniaxial data, i.e. minimum creep strain rate, was found to

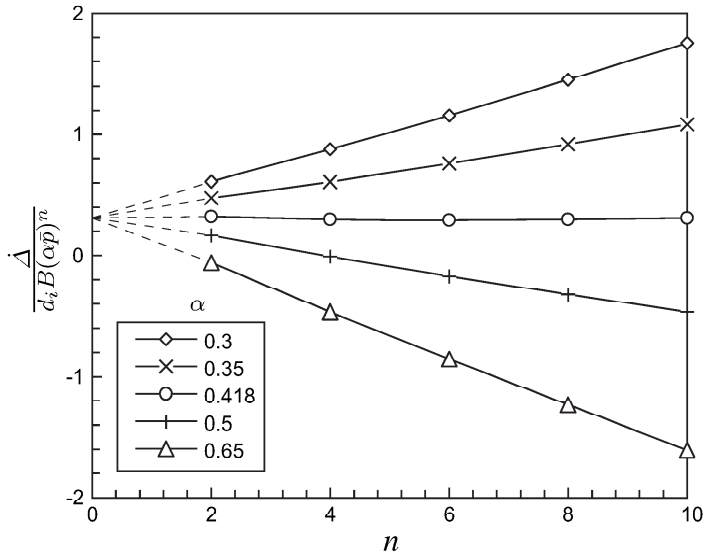

Figure 2.21: Variation of normalised $\dot{\Delta}$ versus n (adapted from ref. [52], Fig.5 (a)).

be accurate when the displacement of the indenter is small compared to the the specimen thickness or indenter width [52].

A limitation of this technique is represented by the range of materials that can be tested, because, in order to avoid excessive deformations of the indenter, its creep resistance needs to be two to three orders of magnitude higher than that of the specimen. Therefore, steels for high temperature applications, such as P91 or 0.5Cr-Mo-V steels, can be tested [52], while materials with higher creep strengths, such as nickel-based superalloys, cannot be tested [42]. Also, the displacement of the indenter during the test is in the order of magnitude of 0.1 [mm], see Figure 2.18, hence accurate measurement systems need to be used because experimental noise, due for example to temperature fluctuations during the test, is likely to affect the test results [42, 98].

2.5.3 Small Ring Creep Test

Small ring creep testing is a relatively new miniature testing technique in which a small circular or elliptical ring is diametrically loaded at high temperature by the use of two pins [42] and the variation of the load-line displacement with time is measured and recorded. The specimens are relatively easy to manufacture [53] and they can be obtained from a scoop

sample similar to that shown in Figure 2.17. Figure 2.22 shows a schematic representation of a small ring specimen and the experimental set-up used by Hyde et al. for small ring creep testing of a nickel-based superalloy [42]. The experimental output is able to provide information about the primary and secondary creep behaviour of the investigated material [42, 53]; Hyde and Sun [53] proposed an analytical solution for the load-line displacement rate of an elliptical ring in the steady-state creep regime, where the effects of shear stresses are neglected and only bending deformation is taken to influence the results. The solution is given in equation (2.41a), where *P* is the load applied to the ring specimen, a_r is the semi-axis of the specimen perpendicular to the loading direction, b_r is the semi-axis parallel to the loading direction, d_r is the width of the cross section of the specimen, $b_{0,R}$ is the thickness of the specimen, *n* and *B* are the Norton creep law material constants and Int_2, defined by equation (2.41b), is a term which depends on the geometry of the specimen and the Norton stress exponent, *n*, with θ_r representing the angular coordinate of the small ring specimen.

$$\dot{\Delta} = \left(\frac{2n+1}{n}\right)^n \mathrm{Int}_2(n, a_r/b_r)\frac{4a_r b_r}{d_r} B \left(\frac{P a_r}{b_{0,R} d_r^2}\right)^n \tag{2.41a}$$

$$\mathrm{Int}_2\left(n, \frac{a_r}{b_r}\right) = -\int_0^{\theta_r^I} \left(\cos\theta_r - \cos\theta_r^I\right)^n \left(1-\cos\theta_r\right) \sqrt{\left(\frac{a_r}{b_r}\right)^2 \sin^2\theta_r + \cos^2\theta_r}\, d\theta_r + \\ + \int_{\theta_r^I}^{\pi/2} \left(\cos\theta_r^I - \cos\theta_r\right)^n \left(1-\cos\theta_r\right) \sqrt{\left(\frac{a_r}{b_r}\right)^2 \sin^2\theta_r + \cos^2\theta_r}\, d\theta_r \tag{2.41b}$$

Figure 2.23 shows the small ring creep test results obtained by Hyde et al. [42] for a nickel-based super alloy tested at 800°C.

Similarly to the impression creep test, see Section 2.5.2, the experimental output can be related to conventional creep data as well, by use of the reference stress method. The relations between the constant load applied in a small ring test and the reference stress is given in equation (2.43), while equation (2.44) relates the displacement rate, $\dot{\Delta}$, to the creep strain rate $\dot{\varepsilon}^c$. The η and β values can be calculated by using a procedure similar to that described in Sections 2.5.1 and 2.5.2 using the relation, given by equation (2.42), of $\dot{\Delta}$ with

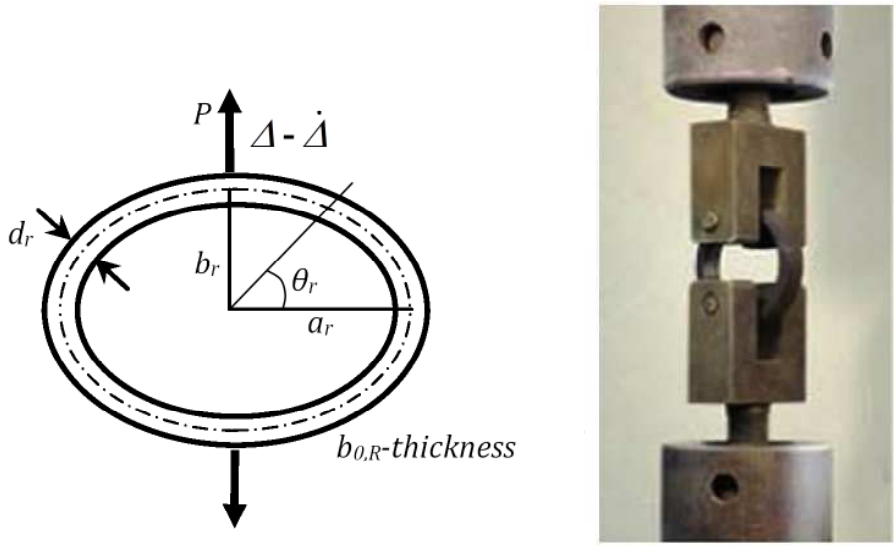

(a) (b)

Figure 2.22: (a) Schematic representation of the small ring specimen (adapted from ref [53], Fig.5) and (b) experimental set-up used by Hyde et al. (adapted from ref [53], Fig.7).

the material properties and the geometry of the specimen. Also in this case, these parameters are material independent and vary with the geometry of the specimen. During the test, they are practically constant [42, 53].

$$\dot{\Delta} = \left(\frac{2n+1}{n}\right)^n \frac{\mathrm{Int}_2(n, a_r/b_r)}{\alpha^n} \frac{4a_r b_r}{d_r} B \left(\alpha \frac{P a_r}{b_{0,R} d_r^2}\right)^n \tag{2.42}$$

$$\sigma_{REF} = \eta \frac{P a_r}{b_{0,R} d_r^2} \tag{2.43}$$

$$\dot{\varepsilon}^c(\sigma_{REF}) = \frac{d_r}{4 a_r b_r \beta} \dot{\Delta} \tag{2.44}$$

During the test, the transverse semi-axis, a_r, decreases and, as a consequence, the reference stress decreases also, see equation (2.43) [53]. The variation of the reference stress with time during the test is also reflected in the results shown in Figure 2.23, where the primary region of the displacement curve, characterised by a decreasing rate, is followed

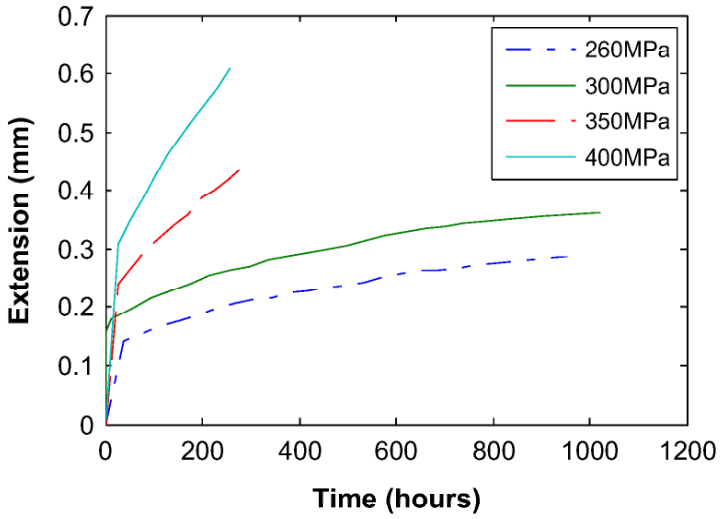

Figure 2.23: Variation of the load-line displacement versus time of small ring creep tests performed on an Inconel 738 nickel-based superalloy at 800°C (adapted from ref [53], Fig.7)

by a secondary region where the deformation rate is not quite constant but rather exhibits a finite curvature [42]. Hyde et al. obtained the minimum creep strain rate data from the small ring creep test results plotted in Figure 2.23 by using the data in the region where the rate is almost constant and taking specific values of $\dot{\Delta}$ at regular time intervals. The averages of the values of the reference stress and the corresponding creep strain rates calculated at these time intervals were then used to obtain the final values [42]. Figure 2.24 shows the variation of the minimum strain rate, obtained from small ring creep tests, plotted versus the stress on logarithmic scales, together with corresponding uniaxial creep results for an Inconel 738 superalloy and a P91 steel [42, 53].

The experimental results reported in Figure 2.24, show that the correlation between small ring test data and conventional creep data is excellent [42, 53], therefore this testing technique is capable of providing secondary creep data. Furthermore, the small ring creep test method is a high sensitivity test because of the high flexibility of the specimen and the large equivalent gauge length obtained for this testing method, EGL_{SRT}, reported in equation (2.45). Also in view of the large equivalent gauge lengths which are obtained with this these tests, relatively large deformations are obtained with good accuracy and these are related to small strains. Thermal fluctuations and other forms of experimental noise experienced during tests do not significantly affect the testing results, in view of the

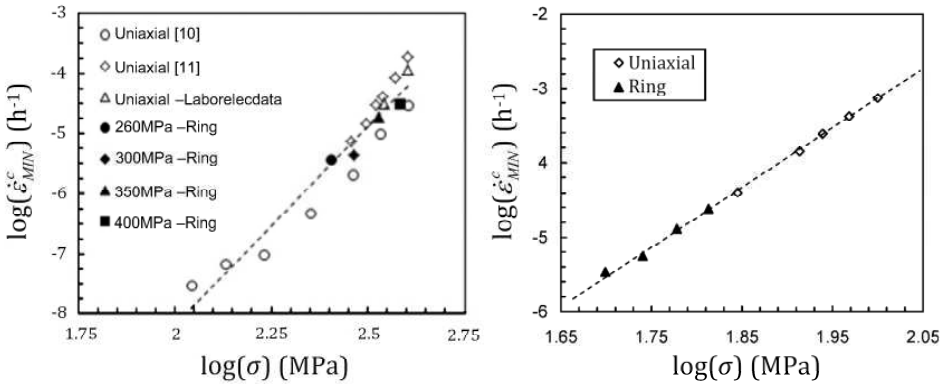

(a) (b)

Figure 2.24: Variation of the minimum creep strain rate versus stress obtained from small ring creep tests performed on (a) an Inconel 738 nickel-based superalloy at 800°C (adapted from ref. [42], Fig.12), and (b) a P91 steel at 650°C (adapted from ref. [53], Fig.12). The results are compared to corresponding uniaxial data.

relatively large overall deformations involved.

$$EGL_{SRT} = \frac{\dot{\Delta}}{\dot{\varepsilon}^c} = \frac{4a_r b_r \beta}{d_r} \tag{2.45}$$

The stresses and the temperatures at which the specimen can be tested are close to practical operational conditions, whereas, for the indentation creep test method, the testing stresses are usually significantly higher [42, 53]. This constitutes a major advantage of the small ring testing technique because the materials of the specimen and of the loading pin can have similar creep resistance. As a consequence, if the pins are manufactured from the same material as the specimen, then high creep resistance materials, such as nickel-based superalloys, can be tested [53].

2.5.4 Small Two-Bar Creep Test

Impression creep and small ring creep tests provide information about primary and secondary creep regions only, as specimens are not taken to rupture during tests. In order to investigate the creep rupture behaviour from a small volume of material, Hyde et al. [45, 46] developed a small two-bar specimen testing technique, in which a small specimen is creep

tested with a constant load applied by two pins characterised by a higher creep resistance than the specimen's material. The geometry of the specimen is shown in Figure 2.25 (a), where $L_{0,T}$ is the distance between the axes of the pins, k_T is the length of the supporting end, $D_{i,T}$ is the diameter of the loading pins and b_T and d_T are the dimensions of the bars cross section, while the experimental set-up is represented in Figure 2.25 (b) [45]. Typical dimensions of the specimen are $L_{0,T}$=13 [mm], b_T=2 [mm], $k_{i,T}$=6.5 [mm] and $D_{i,T}$=5 [mm], which allow the specimen to be manufactured from a sample of material of the type shown in Figure 2.17 [55].

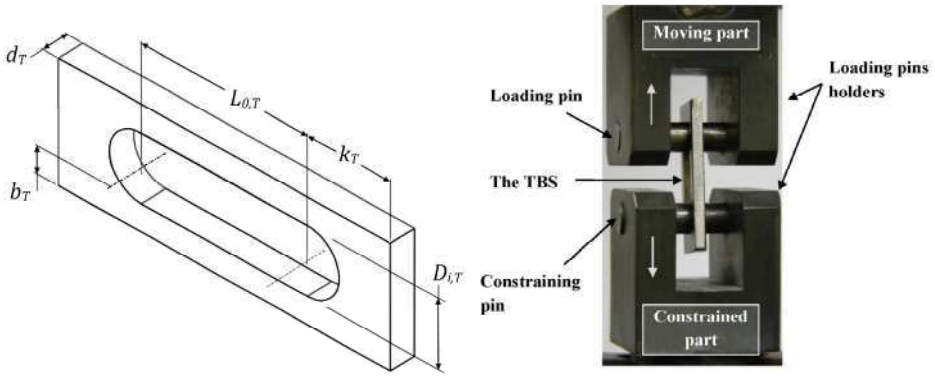

(a) (b)

Figure 2.25: (a) Two bar creep test specimen and (b) experimental set-up, adapted from ref. [45], Fig 5.

The displacement of the movable pin is recorder with time to provide the experimental output of the test, as well as the failure time of the specimen. Hyde et al. used the reference stress method, see equations (2.35) and (2.36), to relate the experimental output of two-bar creep tests with uniaxial creep tests data. Equation (2.46) is the mathematical link between the minimum deformation rate obtained from two-bar creep tests, $\dot{\Delta}_{S-S}$, and the minimum creep strain rate, $\dot{\varepsilon}^c_{MIN}$, of the reference uniaxial test, while equation (2.47) relates the reference stress to the loading conditions and the geometry of the two-bar specimen [45].

$$\dot{\Delta}_{S-S} = \beta L_{0,T} \dot{\varepsilon}^c_{MIN}(\sigma_{REF}) \tag{2.46}$$

$$\sigma_{REF} = \eta\sigma_{NOM} = \eta\frac{P}{2b_T d_T} \tag{2.47}$$

In the work by Hyde et al. [45], the values of the reference stress parameters, for the two-bar specimen with typical dimensions, were obtained by an FE-based procedure, similar to that used in the case of impression creep test, see Section 2.5.2. The values η=0.987 and β=1.456 were obtained. As for the impression creep and the small ring creep tests, these parameters are material independent and they take into account the stress conditions and the geometry of the specimen tested. The η parameter is close to unity because the mechanism governing creep deformation and rupture of the plain bars is mainly stretching under uniaxial stress. Bending deformation occurs in the ends of the specimen and local contact forces act between the pins and the specimen. However, the deformation of the ends of the specimen was found to have a relatively insignificant effect on the experimental data [45]. Figure 2.26 shows the results of the numerical procedure used to obtain the η and β parameters, where the steady-state displacement rate is normalised and plotted against *n* on logarithmic scales. The α value for which the normalised $\dot{\Delta}_{S-S}$ is independent of *n* is chosen as the η parameter. Similarly to the cases of the impression creep and the small ring testing methods, the logarithm of β is the intercept on Figure 2.26 for *n*=0.

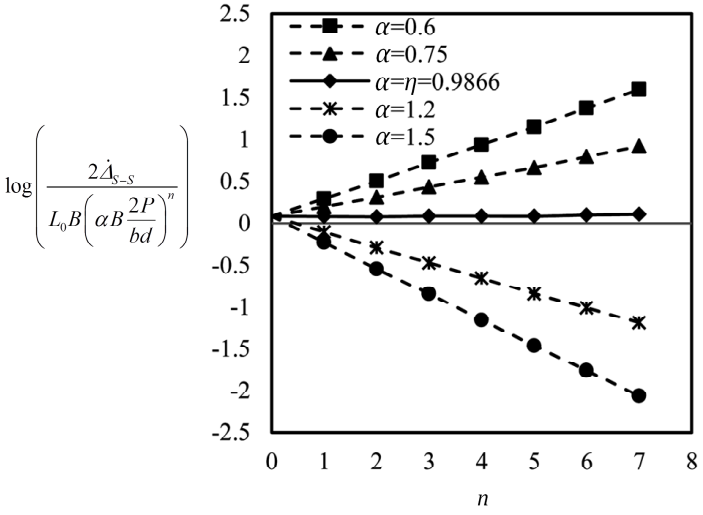

Figure 2.26: Variation of the normalised $\dot{\Delta}_{S-S}$ versus *n*, on logarithmic scales, for different values of the α scaling factor, obtained from FE analyses of a two-bar specimen test. Adapted from ref. [45], Fig 9.

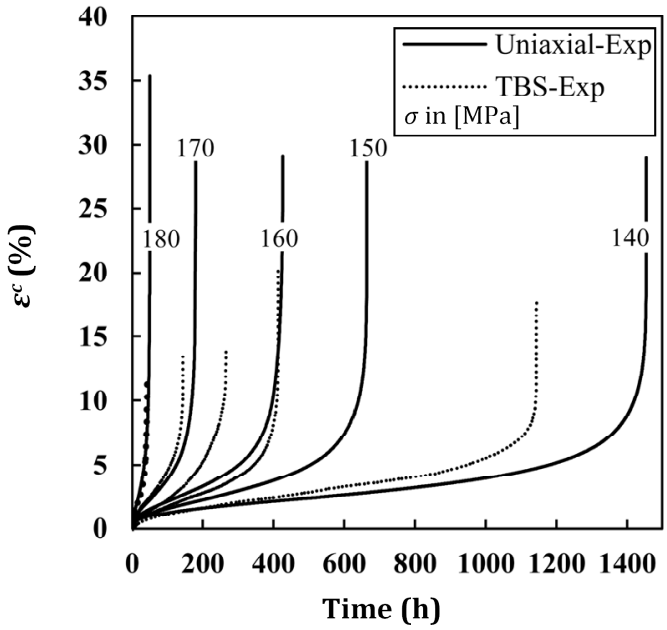

Figure 2.27: Plot of the converted creep strain versus time for two-bar creep tests of a P91 steel at 600°C compared with corresponding uniaxial data. Adapted from ref. [45], Fig 18.

Figure 2.27 is a plot of the creep strain versus time obtained, by Hyde et al. [45], by converting the experimental results of two-bar creep tests for a P91 steel at 600°C. The corresponding uniaxial creep results are also included for comparison [45].

Figure 2.28 shows the variations of the converted minimum strain rate and of the rupture time with stress, on logarithmic scales [45, 46]. The results reported in Figures 2.27 and 2.28 show a good degree of correlation between two-bar output and uniaxial creep test data. Furthermore, the curves shown for two-bar creep strain versus time exhibit primary, secondary and tertiary creep regions, leading to failure. However, since the reference stress parameters were obtained by using a Norton's creep law, they accurately describe the steady-state creep behaviour but further investigation is needed for their application to tertiary creep regime [45].

Hyde et al. [46] also used the notched two-bar specimens, shown in Figure 2.29, to determine the stress multi-axiality material constant, α_D, of the Kachanov and the Liu&Murakami creep damage models, see equations (2.23)-(2.28), for a P91 steel at 600 and 650°C. They obtained results which are very consistent with those of traditional notched specimen tests

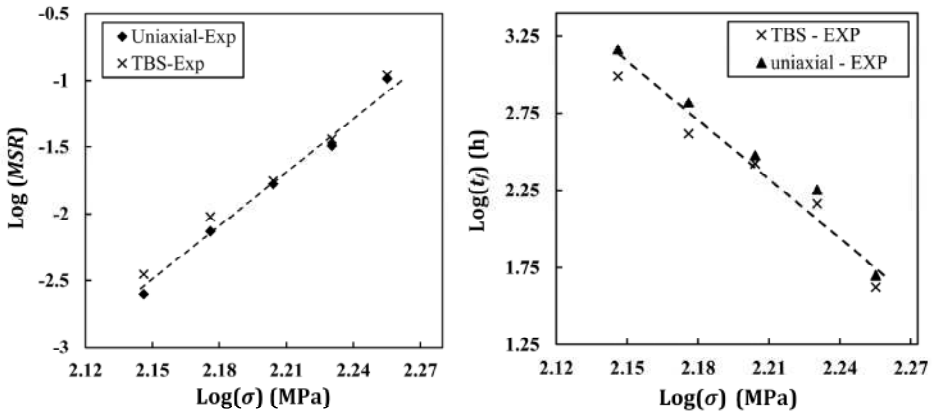

(a) (b)

Figure 2.28: (a) Variation of the converted minimum creep strain rate and (b) of the time to failure versus stress for a P91 steel at 600°C, on logarithmic scales. Corresponding uniaxial creep test results are included for comparison. Adapted from ref. [45], Figs. 17 and 19.

Figure 2.29: Two bar notched specimen of a P91 steel used by Hyde and co-workers. Adapted from ref. [46], Fig. 20.

[46].

2.6 Small punch creep testing

2.6.1 Overview

The small punch creep testing (SPCT) method is a miniature testing technique which has been used to predict the full creep curve of a material, from a very small disc specimen [25, 31, 51, 56, 80, 91]. The test consists of a hemispherical indenter, or a ceramic sphere, which is pushed into a disc specimen with a diameter generally ranging between 3 and 10 [mm] and a thickness of approximately 0.2-0.5 [mm], usually clamped between an upper and a lower die containing the receiving hole [1, 31, 51, 56, 80, 91]. Figure 2.30 shows a schematic diagram of a typical experimental set-up used for SPCTs [48].

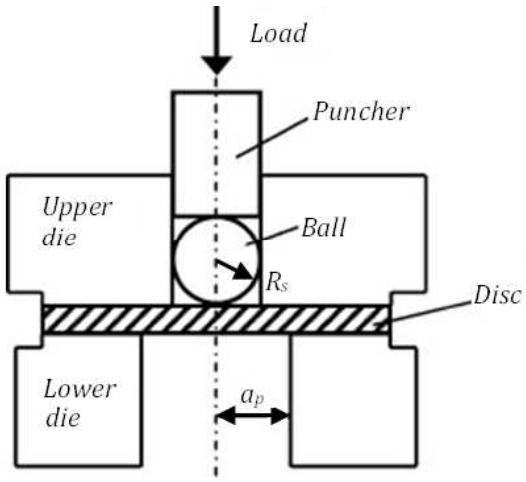

Figure 2.30: Typical SPCT experimental set-up. Adapted from ref. [48], Fig. 1 (a).

The small punch testing technique was first developed in the early 1980s by Manaham et al. [78] at M.I.T., and, since then, it has received much attention from researchers [56, 91]. The first application of this technique was the determination of mechanical properties of irradiated materials from nuclear reactor pressure vessels [78] and, in the early 1990s, Parker et al. [84] reported its use to obtain the creep properties of materials operating at high

temperature.

Two different types of SPCT exist, i.e. the test can be carried out with either a constant load (the variation of the punch displacement versus time is recorded), or a constant deflection rate(the experimental output consists of the variation of the punch load versus punch displacement) [24, 80, 91]. The constant load SPCT is similar to a standard uniaxial creep tests, while the constant displacement rate test is similar to a tensile test with a constant strain rate [80, 91].

2.6.2 Mechanisms involved in the SPCT

The typical experimental output of a constant force SPCT is the variation of the load-line displacement versus time and it can be divided into three regions, as shown in Figure 2.31 [8, 51, 56, 91]. A primary region, characterised by a decreasing deflection rate, is followed by a secondary (or steady-state) region, with a constant deflection rate, and by a tertiary stage with an increasing displacement rate leading to failure, see refs. [31, 72, 80].

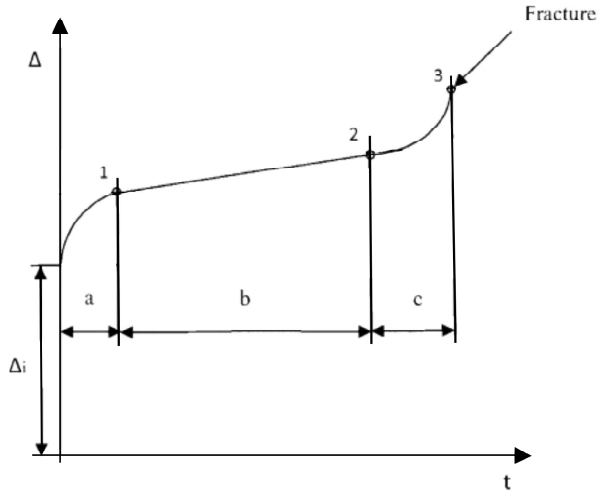

Figure 2.31: Typical SPCT output. Adapted from ref. [51], Fig. 3 (b).

When the specimen is loaded, the head of the indenter applies a contact load over a very small area of the disc specimen. In view of the highly localised contact loading, the stress field in the proximity of the punch/specimen contact area is characterised by remarkably high stresses and strains which will most likely be higher than the yield stress of

the tested material [31]. This generates local plasticity and an initial, large deformation of the specimen. In view of the effects discussed in Section 2.4, the large plastic deformation occurring at the beginning of the test, in localised regions of the specimen, can significantly modify the creep response of the material in those locations. When the deformation of the specimen progresses, the flat disc specimen turns into a conical sample and, as a consequence, the main deformation mechanism, governing the structural behaviour of the specimen, changes from bending to membrane stretching [56]. Furthermore, at this stage of the test, the displacement rate is approximately at its minimum, see Figure 2.31. Kobayashi et al. defined the secondary SPCT region as the time interval in which the deflection rate is less than twice the minimum deflection rate and they reported that this region constitutes most of the test duration [59, 60, 91].

Some authors argued that the secondary SPCT region is characterised by similar mechanisms to those of the steady-state region of a uniaxial creep test curve [16, 76, 91]. However, investigations on interrupted tests, such as that by Kobayashi et al. on super duralumin (A2024B) [59], revealed that circumferential cracks start to nucleate during the primary stage of the test, near the contact edge between the specimen and the punch. The nucleation of these cracks is related to the ductility of the material, and it suggests that the primary and secondary regions of the SPCT curve are not only due to the mechanisms involved in steady-state creep, such as strain hardening and creep recovery (see Section 2.3.1), but they are rather the result of concurrent mechanisms which take place in the specimen, such as geometric stiffening, as the sample undergoes a drastic change in shape from a flat disc to a cone, dislocation creep together with material degradation and crack nucleation and propagation.

In the final stages of the test, the SPCT curve exhibits an increase of displacement rate, which leads to the failure of the specimen [91]. In a standard uniaxial creep test, tertiary creep, characterised by an increasing strain rate, is commonly attributed to the formation and coalescence of voids and intergranular cavitation, that is, material deterioration processes, see Section 2.3, which cause a reduction of the load carrying section and, eventually, rupture of the specimen [6, 91]. In an SPCT, the tertiary region of the deformation curve is related

to several factors, such as material deterioration, macro-cracks propagation in the through-thickness direction and specimen's necking (i.e. geometrical softening) [91].

2.6.3 Analytical modelling procedures of SPCT

The Chakrabarty theory for stretch forming of a rigid-plastic circular blank over a rigid hemispherical punch [13] is the most relevant theoretical study to model the SPCT problem [51, 91].

In Chakrabarty's theory, a thin blank is stretched over a static hemispherical punch and the material of the blank is taken to be isotropic rigid/plastic, in view of the large deformations involved in the problem [13]. The stress and strain fields are influenced by the friction conditions between the punch and the blank, since the maximum thinning location in the membrane moves away from the punch axis of symmetry when friction increases [13]. The punch is assumed to be well lubricated so that friction can be neglected. In contrast to the simpler case of hydrostatic bulging of circular diaphragms, in the stretch forming problem, the boundary conditions are not constant during the process, since the contact edge between the blank and the punch, i.e. the boundary between the supported and the unsupported regions of the blank, changes with the deformation of the blank [13].

Figure 2.32 shows a schematic representation of Chakrabarty's model, where R_s is the punch head radius, a_p is the receiving hole radius, $\phi_{1,Ch}$ and $\phi_{2,Ch}$ indicate the angle between the direction normal to the blank and the axial direction (defined as the *normal angle*) for the supported and the unsupported regions, respectively, r_1 and r_2 represent the radial position of a generic point of the blank for the supported and the unsupported regions, respectively, θ_{Ch} is the normal angle at the clamped edge of the blank, $\theta_{0,Ch}$ is the normal angle at the contact boundary between the membrane and the punch, z and h are the axial position of a generic point of the blank in the unsupported and the supported regions, respectively [13, 91]. For the geometry shown in Figure 2.32, when the thickness of the blank is much smaller than the punch radius, the deformation mechanism of the blank can be considered as purely membrane stretching governed [13].

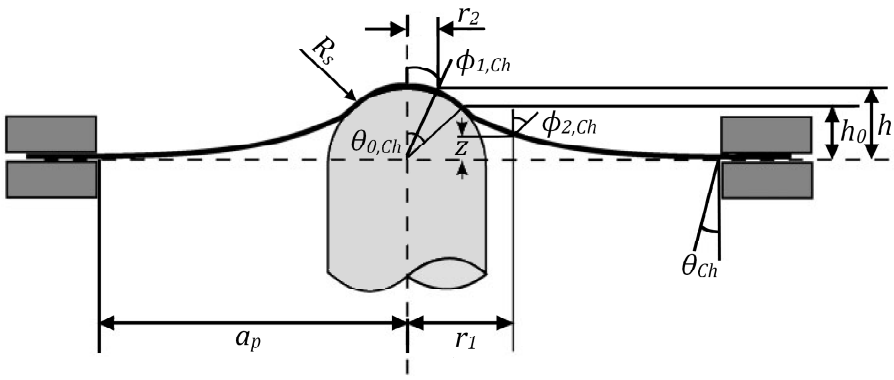

Figure 2.32: Schematic representation of Chakrabarty's model. Adapted from ref. [91], Fig. 3.

The main radii of curvature in the radial and circumferential directions are given in equations (2.48) (a) and (b), respectively [13] and, for the supported region, they degenerate into equation (2.49) [13].

$$\rho_{r,i} = \frac{\partial r_i}{\partial \phi_{i,Ch}} \sec phi_i, i = 1, 2 \tag{2.48a}$$

$$\rho_{c,i} = r_i \csc \phi_{i,Ch}, i = 1, 2 \tag{2.48b}$$

$$\rho_c = \rho_r = R_s \tag{2.49}$$

Equations (2.50) (a) and (b) represent the equilibrium in the normal direction in the supported and unsupported regions, respectively, where σ_c and σ_r are radial and circumferential stresses, respectively, and t_h is the thickness of the blank, while equation (2.51) represents the meridional equilibrium (in both regions of the blank) [13].

$$t_h(\sigma_c + \sigma_r) = pR_s \tag{2.50a}$$

$$\frac{\sigma_c}{\rho_c} + \frac{\sigma_r}{\rho_r} = 0 \tag{2.50b}$$

$$\frac{\partial(t_h \sigma_r)}{\partial r_1} = \frac{t_h}{r_1}(\sigma_c - \sigma_r) \tag{2.51}$$

Equation (2.50) shows that the radii of curvature, ρ_r and ρ_c, have opposite signs in the unsupported region, since σ_r and σ_c are both positive. However, in the supported region, both radii are positive, see equation (2.49), therefore one of them discontinuously changes sign at the edge of contact between the blank and the punch. In view of equation (2.48) (b), ρ_c is continuous over the blank, since $\phi_{1,Ch}$ and $\phi_{2,Ch}$ exhibit the same value at the contact edge, while ρ_r has a discontinuous variation from R_s to a negative value, at the contact boundary [13, 91].

In Chakrabarty's work, the solutions for the strain field in the supported and the unsupported regions of the blank are provided [13]. In the unsupported region, balanced biaxial tension occurs because of the membrane stretching deformation mode and the circumferential and radial stress components, σ_c and σ_r, are equal, as indicated in equation (2.52), where $H(\varepsilon)$ is a strain hardening function. Furthermore, the circumferential and radial strain components, ε_c and ε_r, are equal and are reported in equation (2.53) (a), while the through-thickness strain component, ε_t, is the sum of ε_c and ε_r, as equation (2.53) (b) shows [13, 91].

$$\sigma_c = \sigma_r = H(\varepsilon) \tag{2.52}$$

$$\varepsilon_c = \varepsilon_r = \ln\left[\frac{r_2}{r_{2,0}}\right] = \ln\left[\frac{1+\cos\theta_{Ch}}{1+\cos\phi_{2,Ch}}\right] \tag{2.53a}$$

$$\varepsilon_t = \ln\left(\frac{t_{h,0}}{t_h}\right) = \varepsilon_c + \varepsilon_r = 2\ln\left[\frac{1+\cos\theta_{Ch}}{1+\cos\phi_{2,Ch}}\right] \tag{2.53b}$$

In the Chakrabarty solution, friction in the contact region is neglected and the stress field can be considered as balanced biaxial (as in the unsupported region), see equation (2.52), and, also in this case ε_c=ε_r and ε_t is their sum [13]. Equation (2.54) (a) and (b) report the

solutions for the strain components in the supported region of the blank, where $t_{h,0}$ is initial thickness.

$$\varepsilon_c = \varepsilon_r = \ln\left(\frac{r_1}{r_{1,0}}\right) = \ln\left[\frac{(1+\cos\phi_{1,Ch})(1+\cos\theta_{Ch})}{(1+\cos\theta_{0,Ch})^2}\right] \tag{2.54a}$$

$$\varepsilon_t = \varepsilon_{EQ} = \ln\left(\frac{t_{h,0}}{t_h}\right) = \varepsilon_c + \varepsilon_r = 2\ln\left[\frac{(1+\cos\phi_{1,Ch})(1+\cos\theta_{Ch})}{(1+\cos\theta_{0,Ch})^2}\right] \tag{2.54b}$$

The maximum value for the through-thickness strain component, $\varepsilon_{t,MAX}$, was found at the centre of the blank [13], and it is shown in equation (2.55), which was obtained by replacing $\phi_{1,Ch}$=0 in equation (2.54) (b), while, equation (2.56) shows the through-thickness strain component at the contact edge, $\varepsilon_{t,EDGE}$, where $\phi_{1,Ch} = \phi_{2,Ch} = \theta_{0,Ch}$.

$$\varepsilon_{t,MAX} = 2\ln\left[\frac{2(1+\cos\theta_{Ch})}{(1+\cos\theta_{0,Ch})^2}\right] \tag{2.55}$$

$$\varepsilon_{t,EDGE} = 2\ln\left[\frac{1+\cos\theta_{Ch}}{1+\cos\theta_{0,Ch}}\right] \tag{2.56}$$

From the relationship between $\theta_{0,Ch}$ and θ_{Ch}, reported in equation (2.57), the central displacement, h_{punch}, can be calculated by equation (2.58), while equation (2.59) represents the mathematical link between the punch load and the deformation of the blank, where σ_{EDGE} and $t_{h,EDGE}$ are the radial (or circumferential) stress component and the thickness, respectively, at the contact edge [13, 91].

$$\sin\theta_{Ch} = \frac{R_s}{a_p}\sin^2\theta_{0,Ch} \tag{2.57}$$

$$h_{punch} = a_p \sin\theta_{Ch}\ln\left[\frac{\tan\left(\frac{\theta_{0,Ch}}{2}\right)}{\tan\frac{\theta_{Ch}}{2}}\right] + R_s\left(1-\cos\theta_{0,Ch}\right) \tag{2.58}$$

$$P = 2\pi R_s t_{h,EDGE} \sigma_{EDGE} \sin^2 \theta_{0,Ch} \tag{2.59}$$

Chakrabarty's theory was formulated by using an exponential hardening law, from which the relation of σ_{EDGE} with θ_{Ch} and $\theta_{0,Ch}$, reported in equation (2.60), where A_{Ch} and m_{Ch} are material constants, was obtained. This plastic constitutive model does not reflect the behaviour of any real material, but it can be considered an acceptable approximation to describe the response of metallic materials exhibiting various hardening properties [13, 91].

$$\sigma_{EDGE} = A_{Ch} \left[2 \ln \left(\frac{1 + \cos \theta_{Ch}}{1 + \cos \theta_{0,Ch}} \right) \right]^{m_{Ch}} \tag{2.60}$$

The Chakrabarty model can be used to describe the deformation of a SPCT specimen in the advanced stages of the test, that is, when the disc specimen has turned into a conical shape and its deformation can be assumed to be governed by membrane stretching, see also Section 2.6.2 [91]. Yang and Wang [109] compared the results obtained from an FE model of a SPCT with those of Chakrabarty's theory and they showed that the variation of the central strains versus the central displacement of the specimen, obtained by FE analyses, are in good agreement with the membrane stretching results [91, 109]. Yang and Wang also proposed a polynomial fitting, reported in equation (2.61) between the central displacement, h_{punch}, and the central through-thickness strain component, $\varepsilon_{t,MAX}$, derived from the membrane stretching theory for a small punch test set-up with a_p=2.5 [mm] and R_s=1.2 [mm] (see Figure 2.30). Also in the calculations by Yang and Wang, the maximum thinning of the specimen is located at the centre, as friction between the punch and the sample was neglected [109].

$$\varepsilon_{t,MAX} = 0.2111 h_{punch}^2 + 0.3299 h_{punch} \tag{2.61}$$

However, several authors have shown that, when friction between the punch and the specimen is accounted for, the critical location of a SPCT specimen is the edge of contact

between the punch and the specimen, where the maximum necking and material damage occurs [24, 51, 59, 72, 91]. In view of these observations, Li and Sturm [69] derived a third order polynomial relation, reported in equation (2.62), between h_{punch} and the equivalent strain at the contact edge between the punch and the specimen, for an experimental set-up with a_p=2 [mm] and R_s=1.25 [mm] [48, 69, 91].

$$\varepsilon_{EQ,EDGE} = 0.17959 h_{punch} + 0.09357 h_{punch}^2 + 0.0044 h_{punch}^3 \tag{2.62}$$

It should be noted that equations (2.61) and (2.62) were obtained by applying the membrane stretching theory and they are not valid at the beginning of the test, when this deformation mode does not govern the response of the specimen [1, 69, 109].

2.6.4 Finite element modelling of SPCT

During SPCT, various interacting non-linear mechanisms govern the deformation of the specimen, such as non-linear material behaviour, non-linear contact conditions between the specimen and the test rig components, large deformations and large strains [51, 91]. Therefore, in view of the complexity characterising the test, the finite element (FE) method has proved to be a useful tool for the investigation of the mechanisms which take place during the test. In view of the axial symmetry of the problem, the models reported for SPCT are mostly 2D with axisymmetric elements, adopted for computational cost efficiency with respect to 3D models [31, 51, 91, 109, 113].

Different meshes have been developed for FE models of SPCT specimens and the simplest one consists of a uniform distribution of elements, and nodes, over the specimen, such as that reported by Dymacek et al. in ref. [24]. Also, refined meshes have also been reported in the literature with higher node densities in critical areas of the specimen such as, for example, the expected location for the edge of contact between the specimen and the punch or the regions where bending mainly occurs at the beginning of the test [91]. Ma et al. [76] developed an 'optimised' mesh for SPCT finite element modelling, obtained by

elastic/plastic FE analyses, which consists of four node (linear shape function) axisymmetric elements. They suggested that a relatively large element size can be used in the clamped region of the specimen, in the region under the punch and in the unsupported region [76]. A finer mesh was implemented at the contact boundary between the the punch and the specimen which was identified as a critical location. Experiments also showed that the punch/specimen contact edge is the location where necking usually takes place, therefore, in this region, the highest deformation is expected and smaller elements are required in order to avoid numerical inaccuracies [76, 91]. Figure 2.33 shows the finite element mesh developed by Ma et al. [76]. The use of refined meshes just in specific locations of the specimen (with a coarser element distribution in the remaining regions of the specimen) leads to computational costs reduction, with an increase in the accuracy of the numerical solution for the critical locations of the specimen [91].

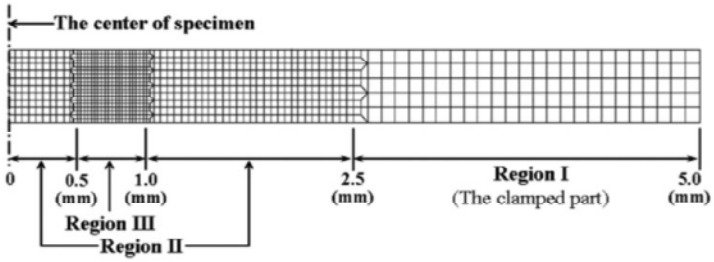

Figure 2.33: Mesh proposed by Ma et al. in ref. [76]. Ref. [76], Fig. 3.

Another critical feature of SPCT FE modelling is the contact interaction between the specimen and the components of the test rig, that is, the punch and the dies. In the FE models reported in the literature, the interactions between the specimen and the components of the test rig have been modelled by using two different approaches. The first is the use a surface-to-surface contact formulation between a deformable specimen and rigid test rig components; the second consists of applying a pressure loads, boundary condition and constraints to the degrees of freedom of the nodes on the expected contact surfaces between the specimen and the components of the test rig [23, 24, 27, 31, 72, 109, 113].

Dymacek et al. investigated the effects of the contact modelling procedure by using two different FE models of a SPCT, similar to those reported in Figure 2.34 [24, 91]. In the first model, see Figure 2.34 (a), the punch/specimen interaction was approximated by a

uniform pressure load applied on the expected contact surface, while the contact between the specimen and the dies was modelled by applying suitable kinematic constraints, i.e. boundary conditions, to the degrees of freedom of the relevent nodes of the specimen [24]. This model is not capable of reproducing the variation of the contact pressure between the punch and the specimen, therefore, the loading conditions applied to the specimen cannot be considered as accurate [24, 91].

In another model developed by Dymacek et al. [24], similar to Figure 2.34 (b), all of the test rig components were modelled as elastic parts interacting with the specimen by a surface-to-surface contact with classic Coulomb's friction formulation.

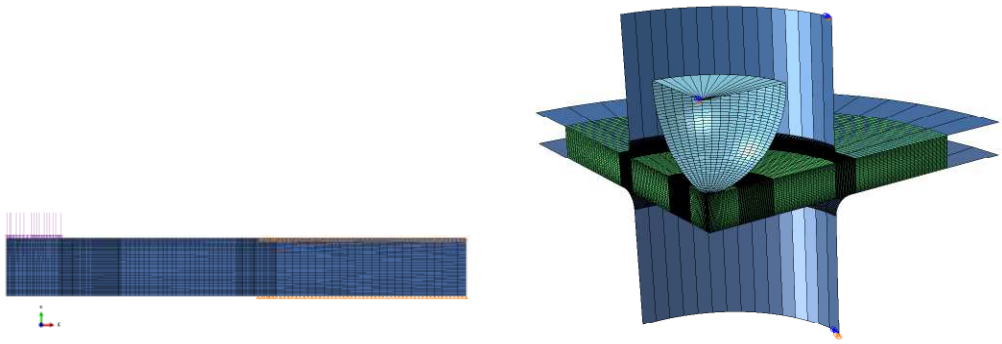

(a) (b)

Figure 2.34: (a) View of the FE meshes based on those developed by Dymacek et al. Adapted from ref. [91], Fig. 6.

The size and the computational costs of the numerical analyses were significantly reduced by the first, more approximate, approach but the second FE model can predict the primary, secondary and tertiary regions of the SPCT output, i.e. the punch displacement versus time curve, even if just the secondary creep behaviour is modelled and no material deterioration is accounted for [91]. This indicates that the numerical results are governed by the change in geometrical stiffness of the specimen, i.e. necking, which cannot be modelled with the first FE model proposed by Dymacek et al. because the constant pressure load applied to the specimen cannot accurately model the contact forces distribution generated by the punch on the surface of the specimen and, in turn, the strain and stress fields in the sample [91].

Another source of inaccuracy in the first model is given by the constraints replacing the contact of the specimen with the support. The round radius of the support influences the strain and stress fields in the specimen and, when boundary conditions are used instead of a contact interaction, those distributions are not accurate. Generally, this approximation leads to a reduction in the estimated time to rupture with respect to that obtained when surface-to-surface contact is used [91]. Also, Dymacek et al. [24] reported that the test rig components are generally not deformed during the test, therefore, in order to reduce the computational costs, they can be modelled as rigid bodies [91].

The work reported by Dymacek et al. also showed that friction between the punch and the specimen strongly influences the numerical results [91]. The stress and strain fields in the specimen are directly influenced by the loading conditions, including the friction forces which act on the contact surfaces. As a consequence, the thickness variation and, generally, the deformed shape of the specimen, is influenced by friction [24, 25].

The use of a frictionless contact model was found to generate an almost constant thickness of the specimen during the analyses and a drastic reduction in the estimation of the rupture time [24, 91]. When the value of the friction coefficient is increased to 0.5, a more realistic variation of the thickness is obtained, but the accuracy of the time to rupture decreases. A friction coefficient of 0.1 was found to be suitable for room temperature cases, but it is not accurate when temperature is increased, therefore, Dymacek et al. [24], adopted a friction coefficient of 0.3 [91].

In view of these effects on the deformed shape of the specimen, Dymacek et al. [24] proposed a method to estimate the friction coefficient by comparing the thickness variation obtained by numerical analyses with the corresponding experimental observations. However, this procedure is not completely accurate, because the friction coefficient is assumed to be constant over the punch/specimen contact surface during the test. That is not necessarily the case because its value also depends on several factors which change during the test, such as the local loading conditions, i.e. the contact pressure and the properties of the interacting surfaces, such as the surface roughness [2, 61, 65, 99, 100].

Guan et al. reported the use of 3D FE models of small punch specimens to investigate the effect of voids, directly modelled into the mesh, during testing by use of elastic/plastic FE analyses [33, 91]. Failure ductility and ultimate tensile stress appeared to be dependent on the defect size, while the initial elastic deformation was generally identical for all cases. The location of failure in the specimen was found to be strongly influenced by defects inclusion [33].

Several authors used secondary creep constitutive models, see Section 2.3.2, in the finite element analyses of SPCT [91]. These models have the advantage that they can be implemented as standard creep constitutive models which exist in commercial FE software. Therefore, there is no need to develop a user subroutine for example. However, as mentioned in Section 2.3.2, the use of just the secondary creep region can be modelled, by neglecting the tertiary creep and material deterioration which occur. The steady-state creep approximation can be useful in some practical situations where creep deformations are not excessive but it can introduce large inaccuracies for those cases where large creep strains and material damage are expected, as for SPCT [91].

Ma et al. used a Norton's creep law, see equation (2.18), for elastic/plastic/secondary creep FE analyses of a SPCT for a Gr91 steel [76]. The contact formulation used by Ma et al. is similar to that shown in Figure 2.34 (b), with a friction coefficient of 0.2. The weakest section of the SPCT specimen was identified as the maximum thinning region, located in the annular region at approximately 0.7 [mm] from the axis of the specimen in the deformed configuration. The critical region also corresponds to the peak equivalent stress and the peak equivalent creep strain location and it is in agreement with the location of creep cracking initiation observed from experiments [16, 59, 76, 91].

Dymacek and Milicka compared the results of FE analyses of a SPCT for a low alloy steel, obtained by using the exponential creep law reported in equation (2.63), where C_e and k_e are material constants, and a Norton's power law, equation (2.18) [23, 24, 91].

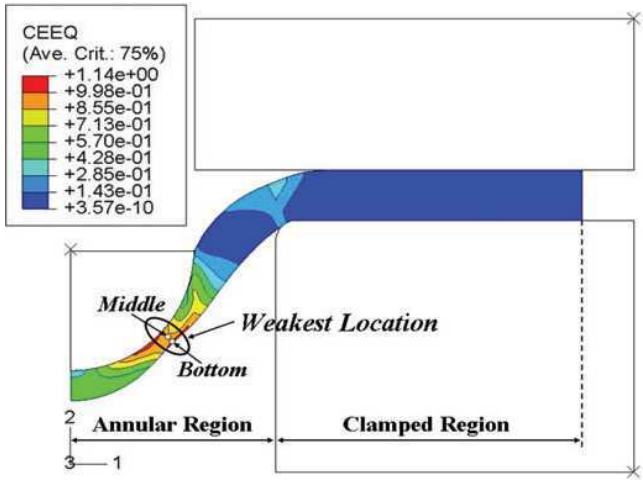

Figure 2.35: Critical region of the SPCT specimen identified by Ma et al. Ref. [76], Fig. 5.

$$\dot{\varepsilon}^c = C_e exp\left[\frac{\sigma}{k_e}\right] \tag{2.63}$$

The results obtained by both these constitutive models were not accurate with high load levels, while, for lower loads, Norton's law led to acceptable results for the failure time, assumed to take place when the tertiary region of the SPCT displacement curve is reached, while equation (2.63) led to conservative results [24, 91].

Dymacek et al. identified three possible sources of inaccuracy for the SPCT FE model proposed in ref. [24], i.e. the constant friction formulation, the neglect of plasticity in the constitutive model which causes an overestimation of the stress field for high loads, and the use of the secondary creep approximations [91].

Norton's creep law was also used by Yang and Wang [109] to developed an SPCT elastic/plastic/creep finite element model and investigate the relationship between the central displacement in the specimen and the central strain described in Section 2.6.3 [91].

The steady-state creep approximation, used in the models reported in refs. [16, 23, 24, 76, 110] leads to unavoidable inaccuracy generated by neglecting the effects of large plastic deformations, observed at the beginning of the test, and creep damage on the subsequent creep behaviour of the specimen [34, 36, 91].

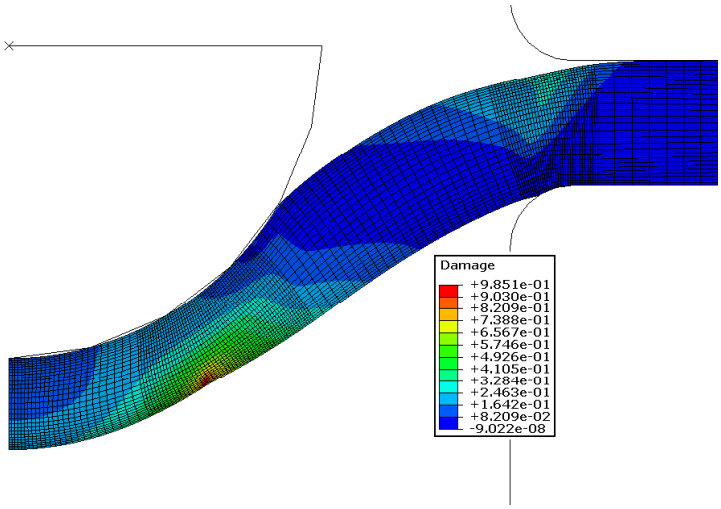

Figure 2.36: (a) Damage contour plot obtained from an SPCT FE analysis based on the work by Ling et al [72]. Ref. [91], Fig. 9 (a).

An FE model of SPCT in which a creep damage constitutive model is used was developed by Ling et al. [72]. They used a single internal variable Kachanov-Rabotnov constitutive model, reported in equations (2.23)-(2.25). Figure 2.36 is a contour plot of the damage variable, defined by equation (2.22), obtained from FE analyses with the same constitutive model as that used by Ling et al. [72, 91]

The final deformed shape obtained by damage FE analyses agrees with experimental evidence, as localised necking is also evident in Figure 2.36 [91]. The peak damage location is close to the lower surface of the specimen at about 0.8 [mm] from the central axis and it corresponds approximately to the critical location, characterised by the maximum creep strain, found by Ma et al. and by Dymacek et al. [24, 76, 91]. Also, the location where cracks initiate in experiments [59] was found to agree well with that shown in Figure 2.36.

Zhou et al. used continuum damage mechanics FE analyses to investigated the effects of test parameters such as the specimen thickness, the punch load, the diameter of the punch head and the specimen's diameter on the experimental output of SPCT [113]. Predicted failure life and punch displacement versus time curves were significantly influenced by the specimen thickness and the load level, as Figure 2.37 shows [91, 113]. Zhou et al. also reported that the specimen diameter does not significantly influence the SPCT output because, for a constant receiving hole diameter, a variation in the specimen diameter affects

the response of the clamped region, which was found to not largely influence the output of the test [113].

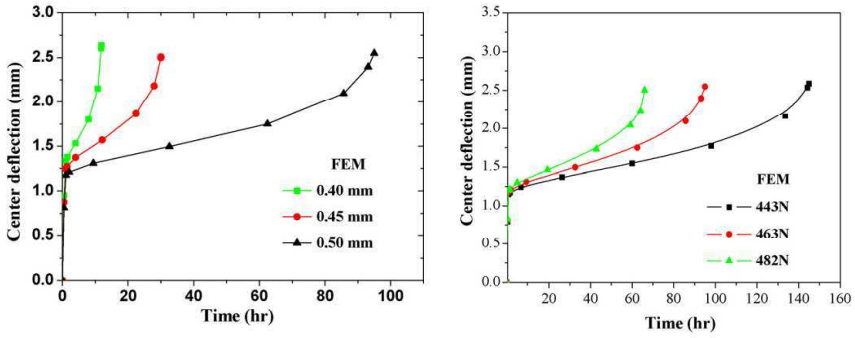

(a) (b)

Figure 2.37: (a) Effects of the thickness of the specimen and (b) of the punch load on the SPCT output. Ref. [113], Figs. 4 and 8, respectively.

A different investigation by Zhuang et al. pointed out that the friction formulation highly influences the tertiary SPCT region obtained from damage mechanics FE analyses [114]. This effect indicates the importance of the inclusion of friction modelling for showing the interaction which occurs between the punch and the specimen [91].

Hyde et al. [51] reported the results of finite element elastic/creep analyses of a SPCT and they compared two different material creep models, i.e. steady-state creep Norton's law, equation (2.18), and Kachanov's creep damage mechanics model, equations (2.23) and (2.24). When Norton's law was used, the plot of the minimum displacement rate versus the load showed an almost constant slope for different displacement levels. These gradients varied for different displacement values when the KR damage mechanics model was used. Hyde et al. used the FE calculations to obtain the reference stress method parameters [51]. These were found to vary considerably during the test, due to the significant change in shape of the specimen, therefore their application to SPCT was revealed to be not convenient.

A phenomenological creep constitutive model (the θ-projection method) was used by Evans and Evans to develop a finite element model of SPCT [27, 29–31]. By use of a stochastic approach, the authors obtained confidence intervals for the SPCT output and the material properties calculated by using it. Figure 2.38 shows the variation of the failure

time versus the punch load obtained by using the θ-projection constitutive model with the relevant confidence intervals, compared with the relevant experimental results [29, 91].

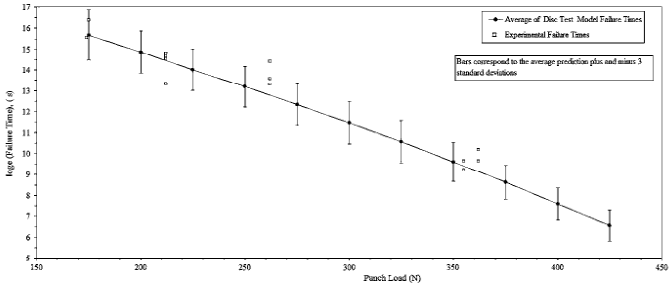

Figure 2.38: Variation of SPCT time to failure versus punch load obtained by FE calculations with corresponding confidence intervals and experimental results. Ref. [29], Fig 3.

2.6.5 CEN code of practice for SPCT for metallic materials

With the aim of developing a universally accepted testing procedure and a technique to convert SPCT output into conventional uniaxial creep test results, in 2006, the European Committee for Standardisation (CEN) published the *CWA 15627 Workshop agreement: Small Punch Test Method for Metallic Materials* [1]. This draft code of practice is the result of an inter-laboratory experimental programme agreed in the framework of a collaborative project involving different institutions, that is, JRC (in the Netherlands), CESI (in Italy), and the University of Swansea (in the UK) [91]. A recommended geometry range for the specimen and the test apparatus was also proposed, in order to improve the reproducibility of the technique [1]. The recommended specimen is a small disc with a thickness of 0.5 [mm], the receiving hole radius is 2 [mm] with a 45° chamfer (0.2 × 0.2 [mm]), while the punch head radius ranges between 1 and 1.25 [mm] [1].

The interpretation technique reported in the CEN draft code of practice [1] is based on Chakrabarty's analysis described in Section 2.6.3 [1, 13, 91]. A method to relate the punch load, *P*, used in a SPCT to the equivalent uniaxial stress, σ_{EQ}^{UNI}, that is, the stress applied during a uniaxial creep test leading to the same time to rupture, was developed and is reported in equation (2.64), where b_1, b_2 and b_3 are parameters depending on the experimental set-up geometry [1, 7].

$$\frac{P}{\sigma_{EQ}^{UNI}} = b_1 a_p^{b_2} R_s^{b_3} t_h \tag{2.64}$$

Alternatively, when uniaxial creep data is available, the load to be applied during a small punch creep test, in order to obtain the same rupture time as in the uniaxial tests, can be calculated by this correlation method [91]. In ref. [1], a fitting of equation (2.64) to the recommended geometry is presented, see equation (2.65), where K_{SP} is a constant which depends on temperature and on the ductility of the material [1].

$$\frac{P}{\sigma_{EQ}^{UNI}} = 3.332\ K_{SP}\ a_p^{-0.2} R_s^{1.2} t_h \tag{2.65}$$

When the K_{SP} factor is not known and uniaxial creep data is available, a first SPCT is performed with a load calculated by assuming K_{SP}=1 and, then, at least 5 additional tests are performed and the rupture behaviour of the material is compared to uniaxial creep test results [1]. It should be noted that equation (2.65) refers to the unclamped disc condition and, when the disc is clamped in the testing rig, the $\frac{P}{\sigma_{EQ}^{UNI}}$ ratio should be reduced by approximately 20% [1].

The draft code of practice also provides a relation, reported in equation (2.66), between the punch load and the meridional stress component, σ_m, at the punch/specimen contact edge, with the punch displacement, h_{punch}. The minimum value of the meridional stress can be used as an approximation of σ_{EQ}^{UNI} [1, 7, 38, 91].

$$\frac{P}{\sigma_m} = 1.725 h_{punch} - 0.056 h_{punch}^2 - 0.177 h_{punch}^3 \tag{2.66}$$

It should be noted that equations (2.65) and (2.66) were obtained by use of the membrane stretching theory [1, 13]. Therefore they are valid after the initial, bending-governed, stages of the test. In the draft code of practice, use of equations (2.65) and (2.66) is recommended for punch displacements larger than 20% of the receiving hole diameter, i.e.

the maximum structural dimension [1, 7, 38]. Furthermore, equation 2.66 is valid for the European Round Robin geometry, i.e. $R_s = 1.25$ [mm], $a_p = 2$ [mm] and t_h.

CHAPTER 3

EXPERIMENTAL INVESTIGATIONS

3.1 Introduction

In Chapter 2, the effects of plastic deformation on the subsequent creep behaviour of various metallic materials is discussed. However, no investigation on the effects of large plastic pre-straining on the creep response of a P91 steel is reported in the open literature.

In this chapter, the results of uniaxial creep tests performed on a P91 steel at 600°C after high temperature tensile pre-straining are reported.

Furthermore, SPCTs were performed on the same material at the same temperature of the pre-strained creep tests, and the results were used to calculate the empirical parameters proposed in the CEN draft code of practice [1].

3.2 Uniaxial pre-strained creep tests of P91 steel at 600°C

3.2.1 Tested material and experimental procedures

Conventional uniaxial specimens were machined from a P91 power plant steam pipe section, with an outer diameter of 298.5 [mm] and a wall thickness of 55 [mm], with the axes of the specimens parallel to the axial direction of the pipe section. Table 3.1 shows the chemical

composition of the P91 steel used [92].

P91 steel is a 9Cr ferritic-martensitic steel modified by the addition of Nb and V (see Table 3.1). These two elements form precipitates that increase the creep properties of the material by opposing dislocation and grain motion and delaying the beginning of tertiary creep [4, 94]. Ferritic-martensitic steels were developed in the 1960s [94], while P91 steel has been used for fossile fuelled power plant components in the USA since the 1970s and it was introduced in the UK power plants in the 1990s [50].

In view of the requirement for improved power plant efficiencies, that is, higher operating temperatures and pressures, P91 has become a potential material for GEN IV nuclear reactor components [8], because, compared to stainless steels, it presents higher resistance to creep and radiation swelling and higher stress corrosion resistance in aqueous environments [94].

Figure 3.1 contains the conventional specimen adopted, together with dimensions in [mm]. The length of the effective section of the specimen, that is, the gauge length, is 50 [mm], with a diameter of 10 [mm]. Two ridges are located at the end of the effective section of the specimen where the extensometer is attached. Hyde [44] reported that the presence of the ridges does not significantly alter the creep response of the specimen.

Before manufacturing the specimens, the blanks, from which the specimens were machined, were tempered at 760°C for 3 [h] and, then, they were cooled to room temperature at a rate of 0.8 [°C/min].

Table 3.1: Chemical composition [wt %] of P91 steel [92].

Cr	Mo	C	Si	S	P	Al	V	Nb	N	W	FE
8.60	1.02	0.12	0.34	< 0.002	0.017	0.007	0.24	0.070	0.060	0.030	*Bal*

A Mayes EN250 machine was used for all of the pre-strained creep tests. The deformation of the specimen was monitored by use of an extensometer with a gauge length of 50 [mm], while the temperature was kept constant to within ± 1°C by the furnace controller of the machine. For each test, the specimen was plastically pre-strained under displacement

control conditions. Subsequently, the configuration of the machine was changed to load control and constant load creep tests were carried out. The load levels used during the creep tests were corrected in order to account for the reduction of the cross sectional area due to plastic pre-straining. When plastic deformation takes place, the volume of the specimen is constant, see Section 2.2, therefore, equation (3.1) holds, where Ω_{pre} and L_{pre} are the cross section area and the length of the specimen at the end of pre-straining, while Ω_{yield} and L_{yield} are the cross section area and the specimen length at yielding.

$$\Omega_{pre} L_{pre} = \Omega_{yield} L_{yield} \tag{3.1}$$

The load, *P*, applied to the specimen is then obtained by equation (3.2) where σ is the stress applied, d_0 is the initial diameter of the specimen's effective section, $\varepsilon_{el,yield}$ is the elastic engineering strain at yielding and ε_p is the plastic pre-strain.

$$P = \sigma \Omega_{pre} = \sigma \, \pi \, \frac{d_0^2}{4} \, \frac{\varepsilon_{el,yield}}{\varepsilon_p + \varepsilon_{el,yield}} \, (1 - \nu \varepsilon_{el,yield})^2 \tag{3.2}$$

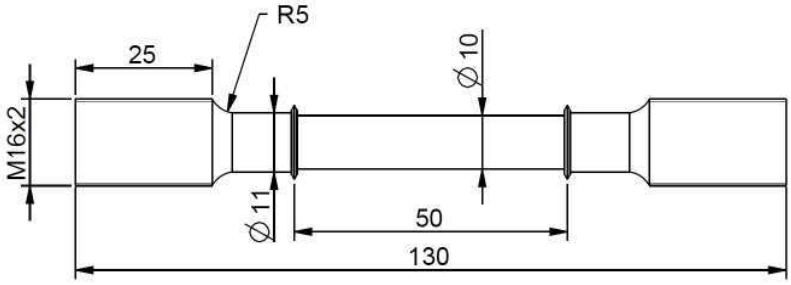

Figure 3.1: Conventional uniaxial creep test specimen adopted for pre-strained creep tests.

The stress levels used for the creep tests are 150, 160 and 170 [MPa]. For the 150 [MPa] tests, the engineering pre-strain levels were 5, 10 and 20%, while, for the other two stress levels, the pre-strain levels were 0.5, 5, 10 and 20%. Uniaxial creep data at 600°C was also available for the P91 steel and was used to provide 0% pre-strain creep results [92].

3.2.2 Experimental results

Figure 3.2 shows the variation of the creep strain versus time obtained from the pre-strained creep tests performed at 150, 160 and 170 [MPa], where ε_{pre} is the total engineering pre-strain. All of the plots exhibit the typical three regions of creep curves, i.e. primary, secondary and tertiary regions, see Section 2.3, and the experimental output was found to be significantly influenced by the plastic pre-straining carried out before creep testing.

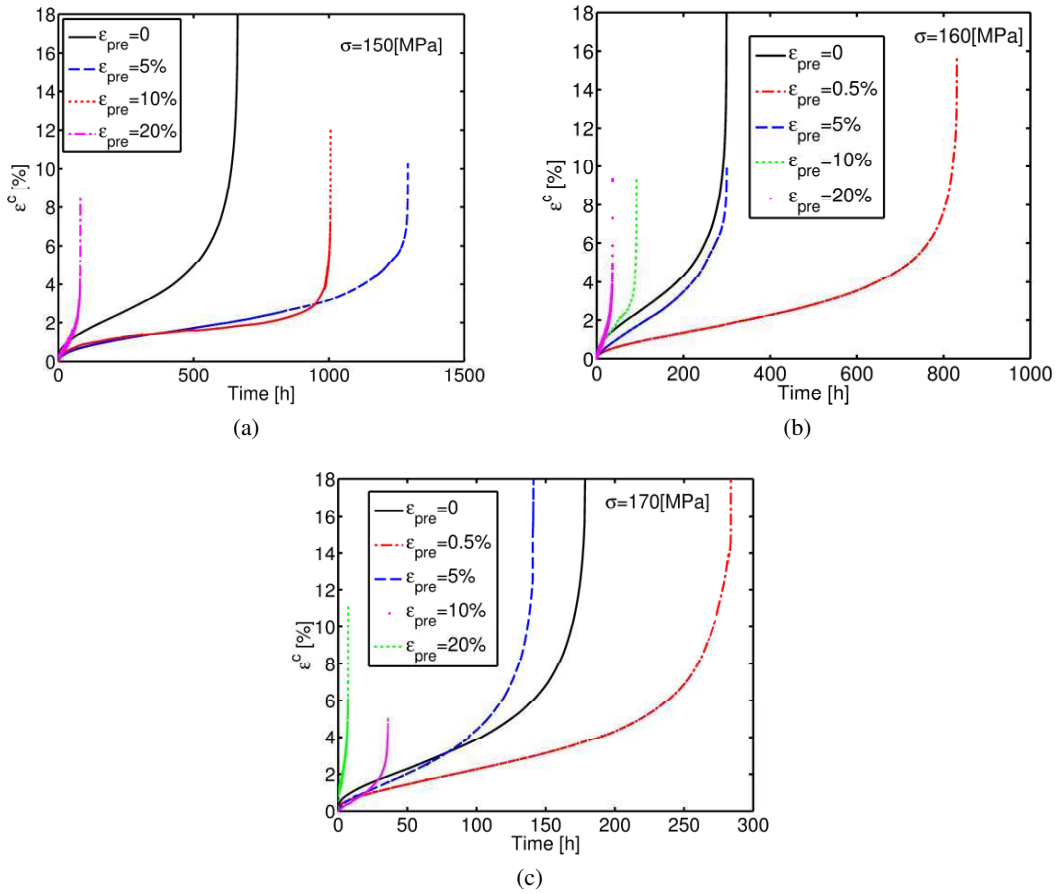

Figure 3.2: Results of pre-strained creep tests at (a) 150 [MPa], (b) 160 [MPa] and (c) 170 [MPa].

The results of the tests performed at 150 [MPa] (Figure 3.2 (a)), show that the material exhibited a creep resistance effect, i.e. the minimum creep strain rate decreases and the time to failure increases, for pre-strain levels of 5 and 10%, while, with a pre-strain level of 20%, a creep enhancement effect was found (i.e. the minimum creep rate increased and the time to rupture decreased). When the stress level was 160 [MPa], see Figure 3.2 (b), creep resistance effects were found for pre-strains of 0.5 and 5%, and creep enhancement

was observed for 10 and 20% pre-straining. For the tests at 170 [MPa], the material showed creep resistance effects for 0.5% pre-strain only, while, for all of the other cases, creep enhancement occurred, as reported in Figure 3.2 (c).

In view of the results shown in Figure 3.2, the effects of high temperature plastic pre-strain on creep response of P91 steel can be quantified by two parameters, that is, ϕ and ψ, which take into account the variation of the minimum creep strain rate and the time to failure, respectively, after applying a total engineering pre-strain level, ε_t. Equations (2.31) [101] and (3.3) define the ϕ and ψ parameters, respectively, where $\dot{\varepsilon}^c_{min,0}$ and $t_{f,n-p}$, are the minimum creep strain rate and the failure time of material in a 0 pre-strain condition, while $\dot{\varepsilon}^c_{min,p}$ and $t_{f,p}$ refer to the material after pre-straining.

$$\psi = \frac{t_{f,n-p}}{t_{f,p}} \tag{3.3}$$

In ref. [101], Tai and Endo used the ϕ parameter in order to model the variation of the minimum strain rate after pre-creep deformation was performed on a 2.25Cr-1Mo steel. However, in the present work, prior deformation is due to plasticity only because time dependent creep deformation is negligible during pre-straining.

For each stress level, the variation of the ϕ parameter with the plastic pre strain, $\varepsilon_{p,pre}$ expressed as a percentage, was fitted by an equation of the form of equation (3.4). The values of each fitting coefficient, obtained for each stress level, were averaged over the three stress levels, in order to obtain an average fitting surface. Table 3.2 lists the average coefficients of equation (3.4) for the P91 steel results.

$$\phi = \frac{\dot{\varepsilon}^c_{min,p}}{\dot{\varepsilon}^c_{min,0}} = \exp\left[a_\phi\ \varepsilon_{p,pre}\right] + b_\phi \varepsilon^2_{p,pre} + c_\phi \varepsilon^3_{p,pre} + d_\phi \varepsilon^4_{p,pre} \tag{3.4}$$

Figure 3.3 shows the variation of the ϕ parameter versus the engineering plastic pre-strain and the stress obtained from the experiments, together with the average fitting surface

Table 3.2: Fitting coefficients for equation (3.4).

a_ϕ	b_ϕ	c_ϕ	d_ϕ
-5.9534	6.690×10^{-2}	-8.800×10^{-3}	3.236×10^{-4}

represented by equation (3.4).

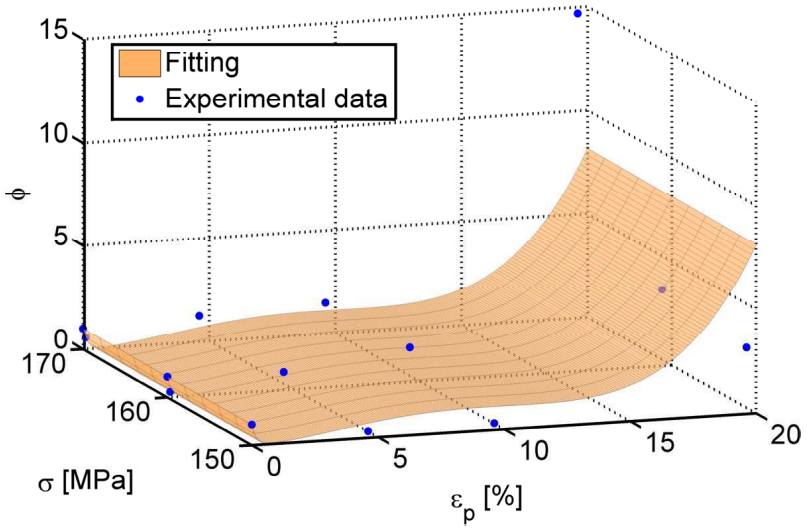

Figure 3.3: Variation of the ϕ parameter with the engineering plastic pre-strain, expressed in percentage, and the stress level, in [MPa], with an average fitted surface to the experimental data.

Similarly, the rupture data for the pre-strained creep tests was used to investigate the variation of the ψ parameter. Equation (3.5) is the fitting equation used to model the ψ variation versus ε_p, for each stress level, and Table 3.3 lists the coefficients of the average fitting.

$$\psi = \exp\left[a_\psi \, \varepsilon_p\right] + b_\psi {\varepsilon_p}^2 + c_\psi {\varepsilon_p}^3 \tag{3.5}$$

Table 3.3: Fitting coefficients for equation (3.5).

a_ψ	b_ψ	c_ψ
-3.241	2.610×10^{-2}	-4.763×10^{-4}

Figure 3.4 shows the variation of the ψ parameter with the engineering plastic pre-strain and stress obtained from the experiments, and the average surface fitted to the experimental results (equation 3.5).

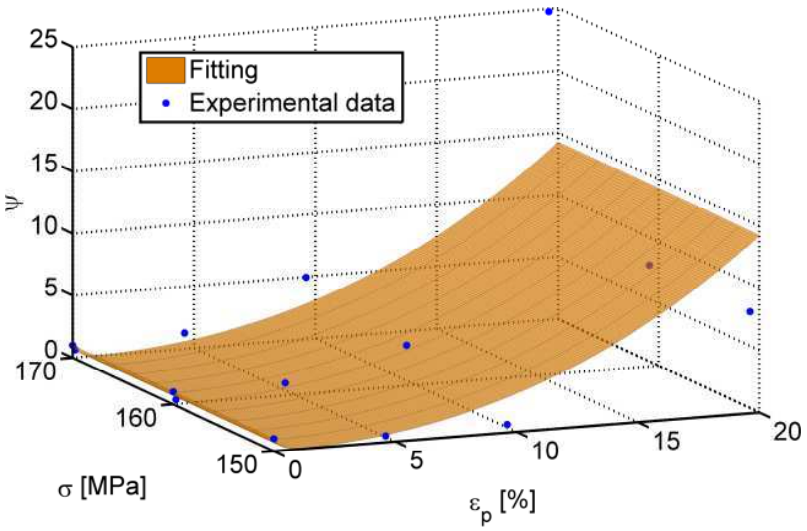

Figure 3.4: Variation of the ψ parameter with the engineering plastic pre-strain, expressed in percentage, and the stress level, in [MPa], with an average fitted surface to the experimental data.

When ϕ>1, the material shows an increase of the minimum creep strain rate when compared with the 0% pre-strained condition (hence it exhibits a creep enhancement effect). When ϕ<1, a creep resistance effect occurs. Similarly, when ψ<1 the failure life of the specimen increases (creep resistance effect) while, for ψ>1, the failure time decreases (creep enhancement effect). Both equations (3.5) and (3.4) lead to ϕ=ψ=1 when the plastic pre-strain equals 0, i.e. for the 0% pre-strained condition.

3.3 Small Punch Creep Tests

3.3.1 Tested material and experimental procedure

The small disc specimens were machined from the same section of P91 steel used for power plant steam pipes, as described in Section 3.2.2. Also in this case, several blanks were machined from the pipe section, with the largest size parallel to the axis of the pipe, and they have been tempered at 760°C for 3 [h] and cooled down to room temperature at a rate of 0.8 [°C/min]. Cylindrical bars, with their axis parallel to the axial direction of the pipe and a diameter of 8 [mm], were manufactured from the heat treated blanks. Disc specimens with a thickness of 0.540 [mm] were machined from the bars by using wire cutting, and these were then polished and lapped to the final thickness of 0.500±0.001 [mm] and a

surface roughness R_a=0.202 [μm] by using 1000 grit and, subsequently, 1500 grit abrasive paper. Figure 3.5 is a schematic representation of the procedure adopted to remove the bars from the pipe section.

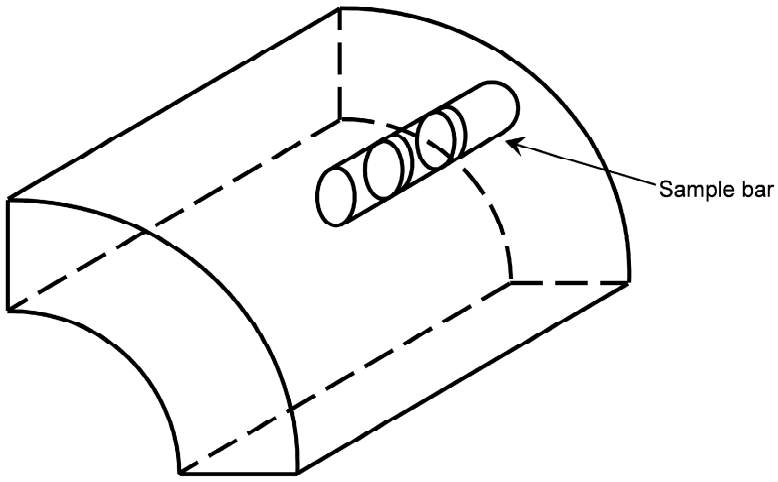

Figure 3.5: Schematic representation of the specimens manufacturing from the P91 steel pipe.

A dead-weight machine, developed by Eo.N., was used for the SPCTs. Figure 3.6 is a schematic cross section of the experimental set-up and of the specimen location, with the corresponding dimensions. The testing assembly consists of the specimen, the punch, the insert tube, a clamping ring and an outer tube. The material used to manufacture the punch and the clamping set-up is a high temperature resistant steel. The outer tube and the clamping ring have holes for the top thermocouple to be inserted. In Figure 3.6, the relevant dimensions of the testing set-up, expressed in [mm] are also shown.

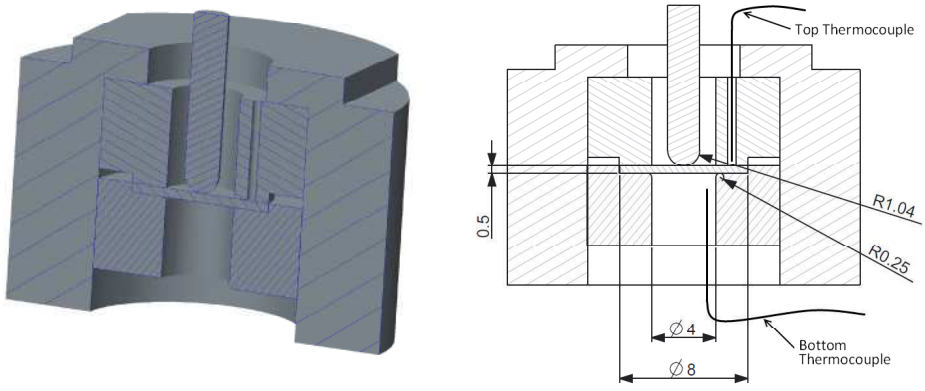

(a) (b)

Figure 3.6: Cross section of the experimental set-up used for the SPCTs with dimensions in [mm].

The specimen was clamped by applying a clamping torque to a metric M25 thread, with a pitch of 1.5 [mm], connecting the outer tube and the insert tube. The value of the clamping force was controlled by monitoring the applied torque and setting it to 10 [Nm] for all of the tests, in order to obtain consistent experimental conditions.

The set-up represented in Figure 3.6 was located in a furnace with a single-zone temperature controller. During the tests, the temperature was kept constant to $600 \pm 1^{\circ}$C by use of the controller of the furnace. Furthermore, two thermocouples were inserted in the testing set-up, these being located at the top surface of the specimen and approximately 10 [mm] below the specimen, respectively, in order to record any temperature fluctuations, in the proximity of the specimen, using a data acquisition system.

The central deformation of the specimen was monitored by use of a linear variable differential transducer (LVDT), which measures the displacement of the punch indenter during the test. The variation of displacement with testing time was also recorded using the data acquisition system.

3.3.2 Experimental results

The SPCTs of P91 steel were performed at a temperature of 600°C with punch loads of 25, 28, 30, 34 and 40 [kg], respectively. Figure 3.7 shows the experimental output of the tests carried out, that is, the variation of the central displacement of the specimen versus time.

Figure 3.8 shows the variation of the minimum displacement rate (*MDR*) versus the load level, *P*, on logarithmic scales.

A power law correlation relating *MDR* and the load level, *P*, was found and it is represented by equation (3.6), where *MDR* is expressed in [mm/h] and *P* in [kg].

$$MDR = 6.457 \times 10^{-15} \times P^{7.790} \tag{3.6}$$

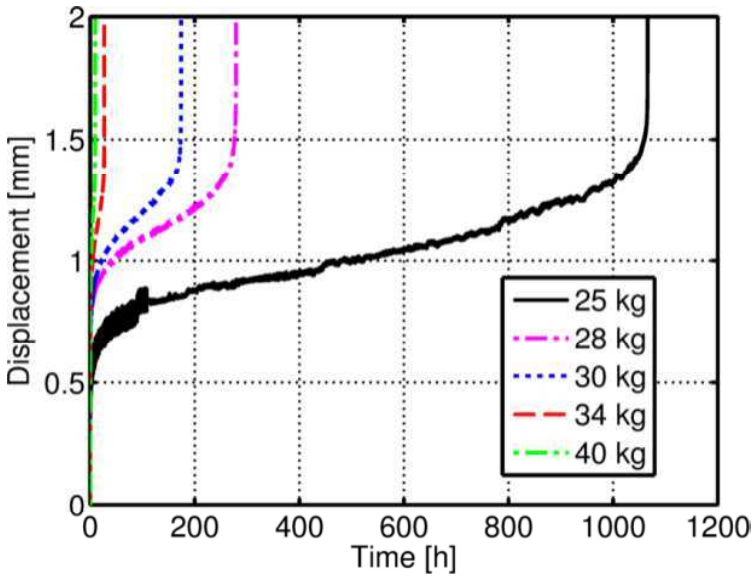

Figure 3.7: Variation of the central specimen deformation versus time for a P91 steel at 600°C with different load levels.

Figure 3.9 shows the variation of the failure time, t_f, versus load level using logarithmic scales. A power law correlation of t_f with load level, given by equation (3.7), was obtained.

$$t_f = 1.995 \times 10^{17} \times P^{-10.24} \tag{3.7}$$

The load level, *P*, was correlated with the equivalent uniaxial stress, σ_{EQ}^{UNI}, defined in Section 2.6.5. The dimensions of the testing set-up, i.e. R_s=1.04 [mm], a_p=2 [mm] and t_0=0.5 [mm], were replaced in equation (2.65), and the multiplication factor of 0.8 was included because the disc specimens were clamped into the experimental set-up, see ref. [1]. The K_{SP} parameter was then calculated for each load level and it was found to increase with the load, in agreement with the results of ref. [34], and the average K_{SP}, for the load range used in the investigation, is $\overline{K}_{SP}$=1.353.

Interrupted tests were also performed using a load of 25 [kg], in order to investigate the evolution of microscopical features in the specimen during the test. Figure 3.10 is a plot of the output of the 25 [kg] completed and interrupted tests. As with previous investigations,

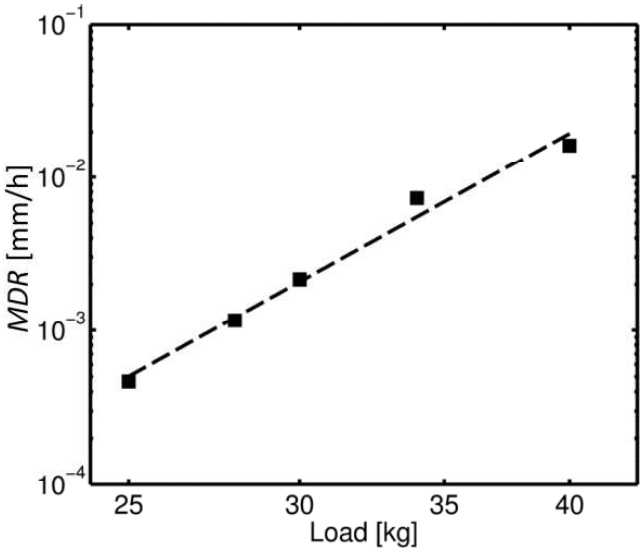

Figure 3.8: Variation of the central specimen deformation versus time for a P91 steel at 600°C with different load levels.

a significant amount of data scatter in the experimental results was found to exist [31]. In the present investigation, the scatter appeared to be related to the characteristics of the testing machine, and to slight misalignment of the loading punch with respect to the axial direction of the test rig. Detailed numerical investigations of this misalignment are reported in Chapter 6.

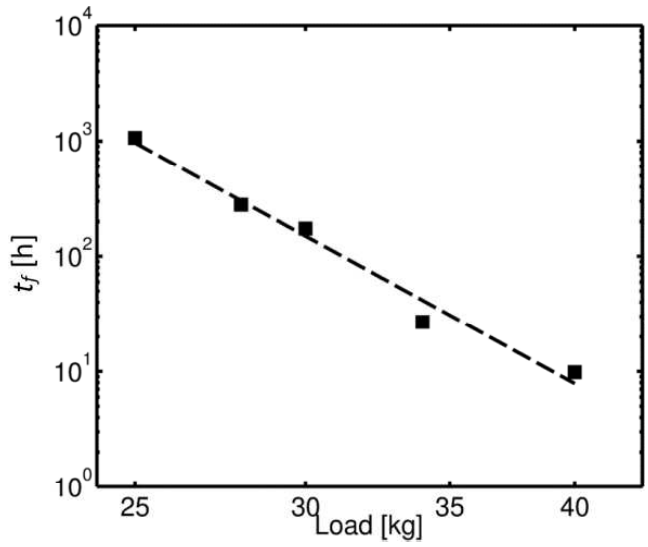

Figure 3.9: Variation of the time to failure (t_f) versus load level, plotted on logarithmic scales.

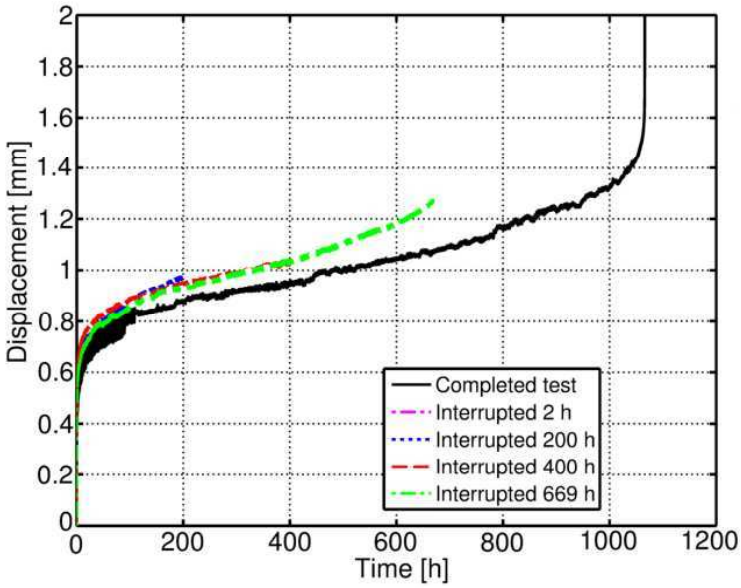

Figure 3.10: Variation of the central deformation of the specimen versus time for the interrupted tests. The punch load is 25 [kg] for all of the tests.

CHAPTER 4

MICROSCOPICAL INVESTIGATIONS

4.1 Introduction

The complex behaviour of a SPCT specimen, as described in Chapter 2, has an influence on the failure mechanisms governing the rupture of the specimen.

Various authors have investigated the failure mechanisms which characterise the behaviour of small disc specimens when tested with constant displacement rate (CDR). Madia et al. [77], studied the failure mechanisms of constant deflection rate (CDR) small punch test specimens for as-received and service-aged 1Cr-Mo-V steel at room temperature. By use of fractographic analyses, they identified ductile failure fracture surfaces on the small punch specimens; there was no evidence of brittle failure and no difference in the failure modes of new and service-aged material. The results shown by Madia et al. agree with those published by Bulloch in refs. [10, 11], where small punch test data, obtained from various turbine components, were reviewed and a detailed fractographic study is reported. A fully through-thickness ductile crack growth failure was found for bainitic and ferritic steels in the upper shelf energy region [10]. Furthermore, Guan et al. investigated the fracture modes of low alloy Cr-Mo steels by fracture toughness tests and CDR small punch tests carried out in air at room temperature [32]. They also pointed out that the fracture surfaces of the small punch specimens showed ductile fracture features, with dimples distributed throughout the whole thickness of the specimen and a circumferential macro crack at the punch/specimen

contact edge, whereas fracture toughness tests exhibited a mixed (ductile/brittle) mode of fracture [32].

However, by contrast, only a limited amount of work has been published for SPCT with constant loading conditions. The deformation and fracture evolutions for SPCT of superduralumin alloy were investigated by Kobayashi et al. [59]. Their work highlighted the presence of micro voids and a circular crack at approximately 20% of the time to rupture, i.e. at the end of the primary region of a SPCT curve, described in Section 2.6.2. In view of Kobayashi's findings, the fracture mode and the evolution of the deformation and of microscopical features characterising the specimen's behaviour need accurate investigation, in order to take them into account when the experimental output is analysed.

No investigations have been reported in the open literature on the failure behaviour of constant force SPCT specimens of P91 steel. In this chapter, the results of a study of the fracture surfaces of P91 steel SPCT specimens tested with the experimental conditions reported in Section 3.3.1, are included. A scanning electron microscope (SEM) was used to analyse the effects of the load on microstructural features. By the use of the interrupted tests described in Section 3.3.2, the evolution of the deformation and of the microstructural features during the tests are identified.

4.2 Effects of load level on fracture surface features

The punch load, ranging between 25 and 40 [kg] (see Section 3.3), governs the amount of initial plastic deformation occurring in the specimen, the creep rate and the duration of the tests. It also influences the failure mode of the specimen.

Figure 4.1 shows the fracture surface of the specimen tested with a load of 25 [kg]. The test failed after 1066 [h] and, since all of the SPCTs were carried out in air, the fracture surface shows evidence of oxidisation, as Figure 4.1 (a) shows. In Figures 4.1 (a) and (c), a circumferential macro-crack is visible at some distance from the centre of the specimen. Tertiary creep features such as creep voids and intergranular separation were observed on the

fracture surface of this specimen, as shown in Figure 4.1 (d). Also, secondary microcracks, propagating in the radial direction on the bottom surface of the specimen, were found. In Figure 4.1 (b), the location of final fracture is shown. This region is less than 5% of the total fracture surface and it is characterised by the presence of fresh dimples, indicating the onset of large plastic deformation.

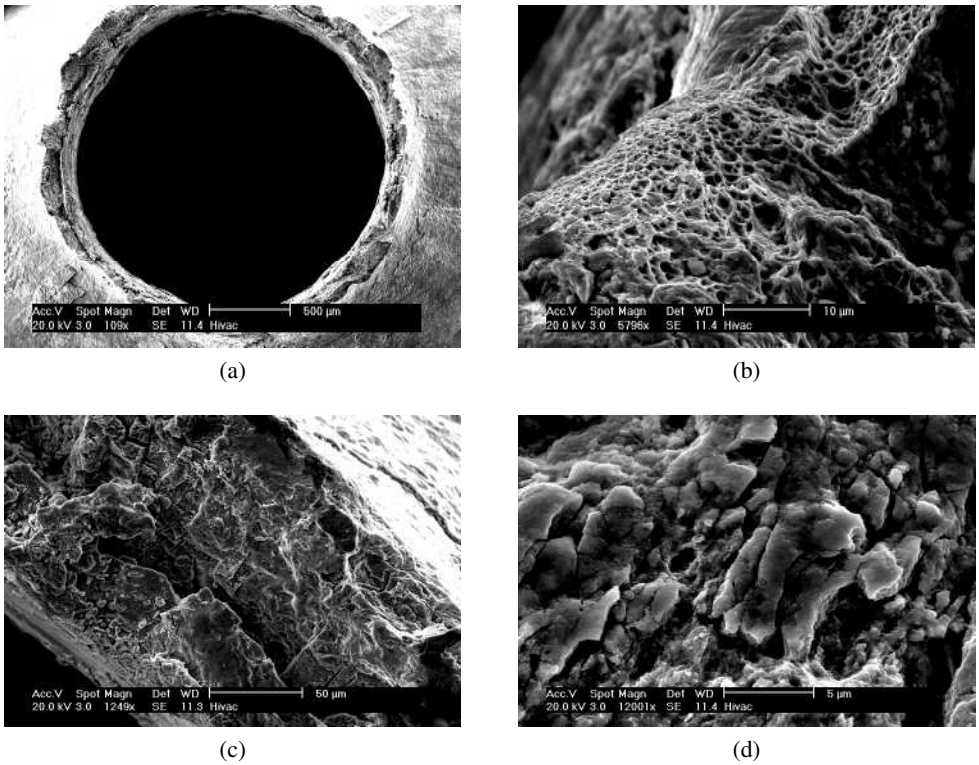

Figure 4.1: SEM images of the fracture surface of an SPCT specimen tested with a 25 [kg] punch load:(a) a global view, details of (b) final fracture region, (c) circular micro-crack and (d) tertiary creep features.

Figure 4.2 shows the fracture surface of the specimen tested with a load of 30 [kg]. The duration of the test was 173 [h] and the presence of oxide on the fracture surface was found to be greatly reduced. A circumferential crack is still visible in Figure 4.2 but the presence of dimples, indicating large initial plastic deformations in the specimen, is, as expected, larger than in the case of the 25 [kg] test.

With load levels of 34 and 40 [kg], the durations of the tests were 27 and 9.8 [h], respectively. The presence of oxidisation on the fracture surface was further decreased for higher load levels, and almost no oxide was found on the specimen tested at 40 [kg], as a

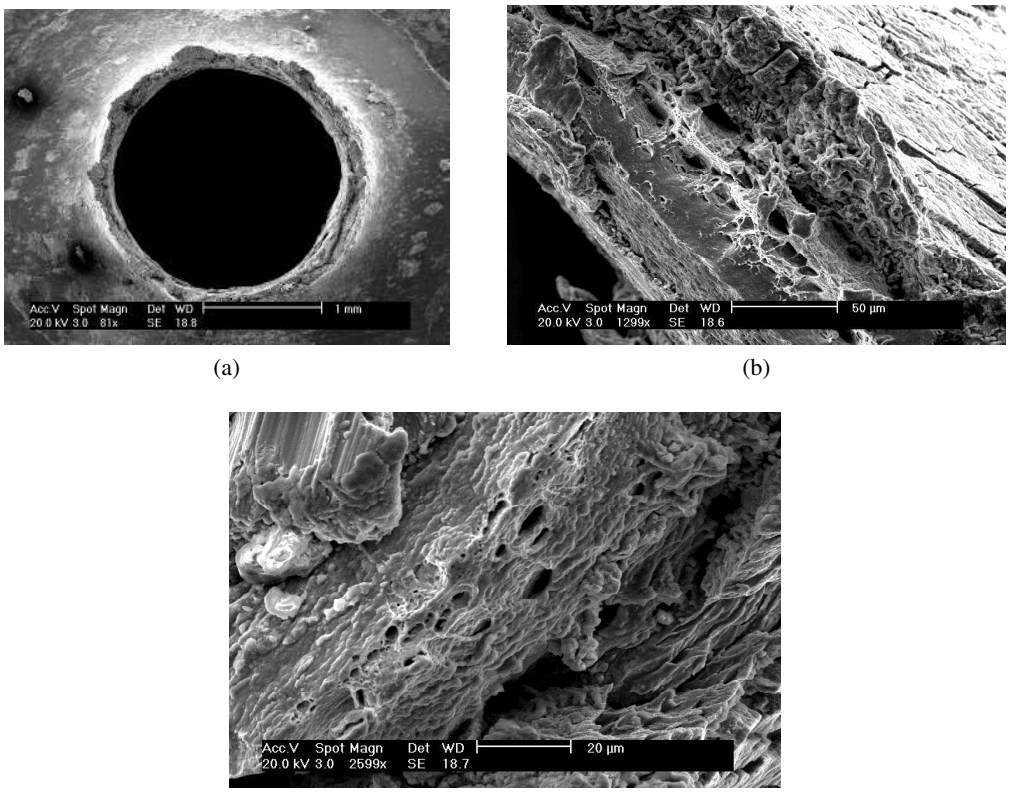

(a) (b)

(c)

Figure 4.2: SEM images of the fracture surface of an SPCT specimen tested with a 30 [kg] punch load:(a) global view and (b)-(c) details.

result of the shorter test duration. In Figures 4.3 and 4.4, details of the fracture surfaces of the specimens tested at 34 and 40 [kg], respectively, are reported. Similarly to the tests with the lower load levels, a circular macrocrack was found in these specimens, as Figures 4.3 (a) 4.4 (a) show. Also, on the bottom surfaces of the specimens, secondary microcracks were observed.

Figures 4.1-4.4 show that the presence of dimples increases as the load is increased from 25 to 40 [kg]. This indicates that, when the load level increases, the fracture mechanism changes from intergranular cavitation-dominant to dimple-dominant, as fracture is mainly governed by plastic deformation, rather than creep. The fracture surfaces of the high load level tests show ductile fracture features, which are also in agreement with the findings reported in refs. [10, 32, 77].

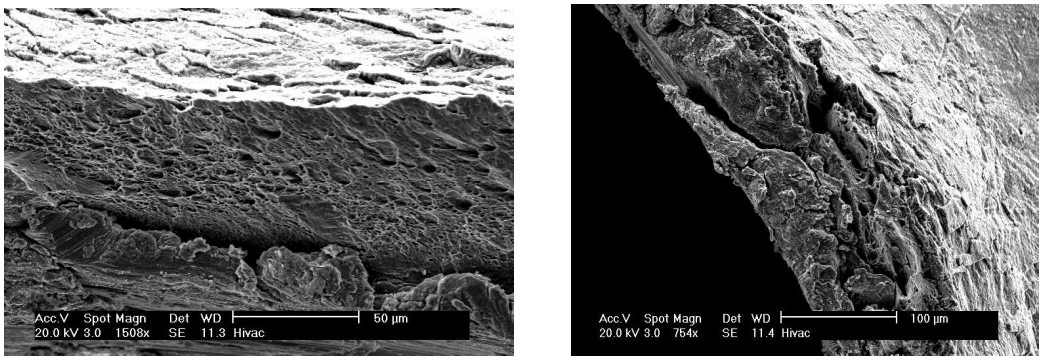

(a) (b)

Figure 4.3: SEM images of the fracture surface of an SPCT specimen tested with a 34 [kg] punch load.

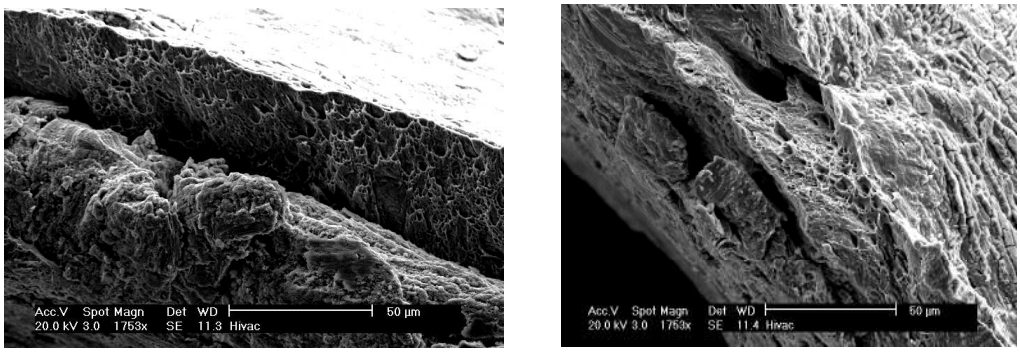

(a) (b)

Figure 4.4: SEM images of the fracture surface of an SPCT specimen tested with a 40 [kg] punch load.

4.3 Effects of load level on specimen deformation and material characteristics

Microstructural investigations of the cross sections of small punch creep test specimens were also performed by use of SEM and the effects of the loading level on microscopical features of the specimens have been studied.

Figure 4.5 shows the cross section microstructure of the failed specimens tested with loads of 25 and 40 [kg]. In Figure 4.5 (a), which shows the microstructure of the 25 [kg] test specimen, the subgrains near the fracture surface location appear elongated. Since large creep deformation occurs, voids and microcracks were found along grain or subgrain boundaries, as Figure 4.5 (b) shows. Microcracks were found near the fracture surface, propagating in the material, and in the unsupported region, where membrane stretching is

dominant (see Figure 4.5 (b)). Oxidisation was found on most of the fracture surface, with the largest oxide thickness being near to the top surface of the specimen, where severe contact loading conditions between the punch and the specimen occur.

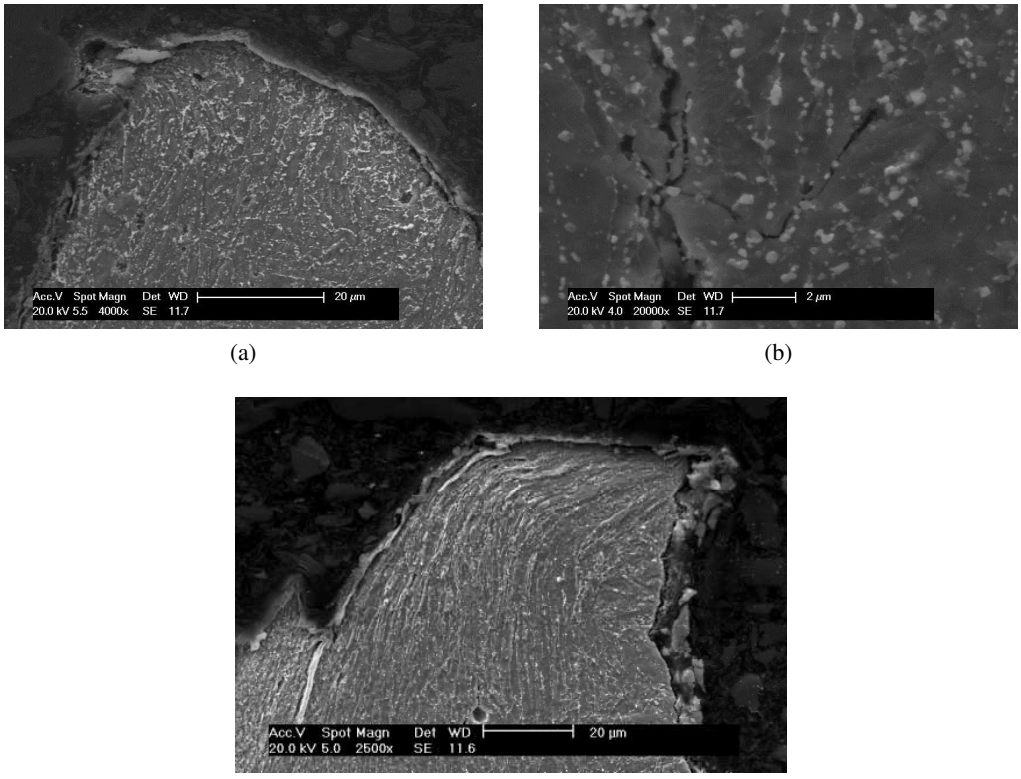

(a) (b)

(c)

Figure 4.5: SEM images for (a) subgrain deformation, micro voids and (b) microcrack along subgrain boundary with a load of 25 [kg] and (c) subgrain deformation with a load of 40 [kg].

During the 40 [kg] test, the elongation and the rotation of subgrains are more significant than in the 25 [kg] test, as shown in Figure 4.5 (c), and voids and microcracks hardly occurred, because plasticity governs the deformation and the failure of the specimen.

The large subgrain rotation found in the 40 [kg] test, which is in agreement with the findings reported in ref. [32], is related to the high initial plastic deformation, since, for the 25 [kg] test, characterised by smaller plastic deformations, such rotation is smaller.

4.4 Evolution of the specimen deformation and material features during the test

A microscopical investigation was also carried out on the 25 [kg] interrupted test specimens (see Section 3.3.2), in order to establish the microstructural evolution of the material during the test. Figure 4.6 shows the microstructure of the heat-treated virgin P91 steel, which consists of homogeneous tempered martensite lathes with a number of finely distributed carbides, nitrides or carbo-nitrides along grain and subgrain boundaries. The virgin material structure was obtained from the clamped, undamaged, region of the 40 [kg] test specimen. This can also be used as the reference material for the interrupted tests because the clamping load is the same for all of the performed tests and the deformation of the material in the clamped region of the specimen is assumed to be negligible in all of the tests.

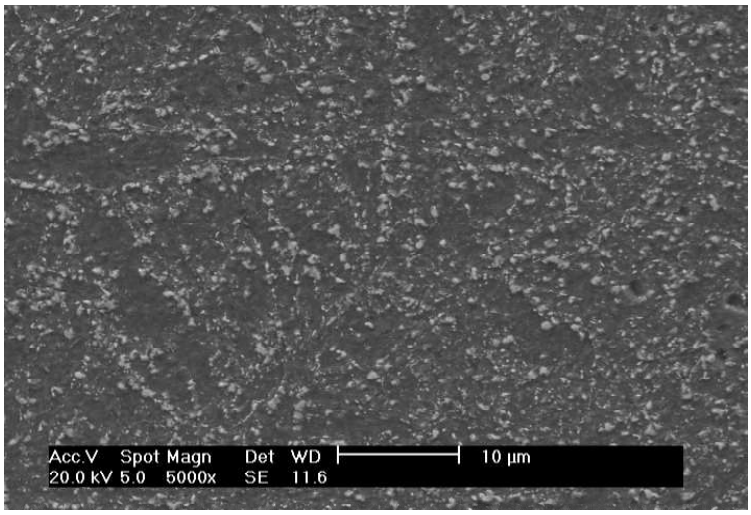

Figure 4.6: Microstructure of virgin P91 steel, taken from the undamaged region of the 40 [kg] test specimen.

Figure 4.7 shows the cross section SEM images, with relevant detailed pictures, of the specimens for the tests interrupted at 2, 200 and 669 [h]. As discussed in Section 4.3, for the 25 kg tests the fracture mechanism is intergranular cavitation and void formation. The specimen fails because a circumferential macro crack, starting from the bottom surface of the specimen (visible in Figures 4.7 (c) and (d)), propagates through the thickness with a direction following the maximum shear stress, i.e. at 45° with respect to the symmetry axis of the specimen (Figures 4.7 (c)-(f)).

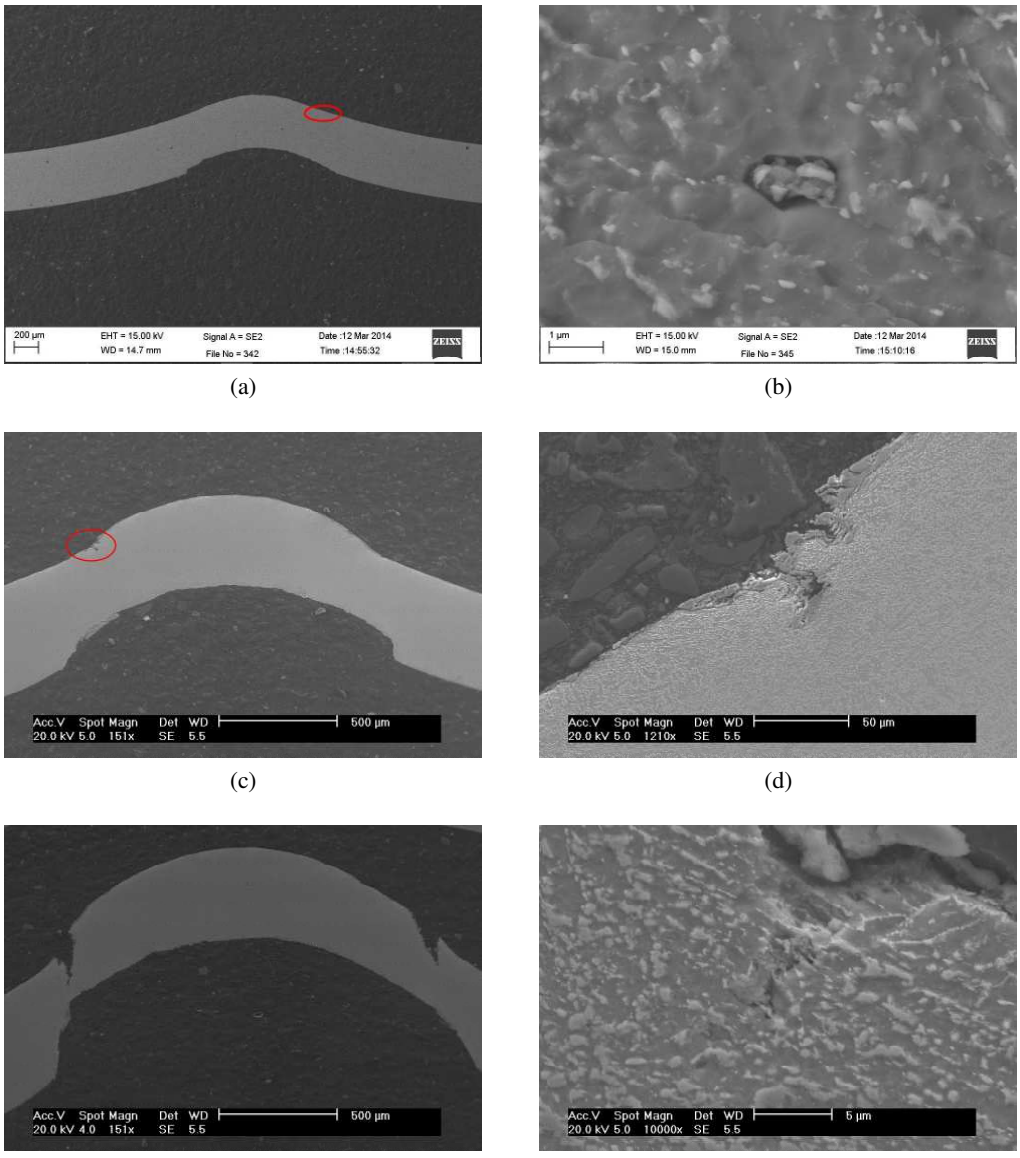

(a) (b)

(c) (d)

(e) (f)

Figure 4.7: SEM images of 25 [kg] interrupted test specimens after (a)-(b) 2 [h], (c)-(d) 200 [h] and(e)-(f) 669 [h].

For the 2 [h] interrupted test, the deformation of the specimen mainly occurred in its central region (Figure 4.7 (a)). In the cross section there is no trace of any macro or micro cracks, but metal solution started to develop along the carbide boundary, as Figure 4.7(b), showing the details of the region close to the bottom surface of specimen highlighted in Figure 4.7 (a), indicates.

For the test interrupted at 200 [h], the deformation of the specimen is larger and a macro crack initiated at the peak stress location, that is, on the bottom surface of the specimen (see Figures 4.7 (c) and (d)).The macro crack is still not completely circumferential, as Figure 4.7 (c) shows. After 669 [h], the macro crack has propagated around a circumference on the bottom surface of the specimen, and its growth in the through-thickness direction is also significant (see Figure 4.7 (e)). Furthermore, microcracks can be observed at the tip of the macrocrack (Figure 4.7 (f)).

4.5 Conclusions

In this Chapter, a microscopical investigation of SPCTs of a P91 steel at 600°C has been reported. The study was mainly concerned with the determination of the influence of the punch load on the fracture mechanism of the specimen and the evolution of microstructural features during the test.

When the load was increased from 25 [kg] to 40 [kg], the fracture mechanism changed from intergranular cavitation to dimple governed rupture, because, for a load of 40 [kg], failure is mainly controlled by plasticity rather than creep (as also the short duration of the high load tests shows). Furthermore, in the region adjacent to fracture, the subgrain rotation increases with the increase of load level.

From the interrupted test results, it was observed that a macrocrack initiated at the bottom surface of the specimen, at about 20% of the failure time. The crack then propagates through the thickness of the specimen, leading to failure. After 669 [h], micro cracks were also found at the tip of the circumferential macro crack.

In the present investigation, the tests were performed in air, without the use of a protective atmosphere, e.g. argon. Dymacek and Dobes investigated the influence that the atmosphere has on SPCT output and reported that, for P91 steel at 600°C, when the rupture time is within about 500 [h], the atmosphere does not have a very significant effect on the experimental results [22].

For P91 specimens, in the present study, different degrees of oxidisation were observed for the various load levels adopted and, for the longest creep test (25 [kg] punch load), extensive oxidisation was found on the fracture surface. As the load was increased, the oxide presence on the fracture surface decreases.

CHAPTER 5

EFFECTS OF INITIAL PLASTIC DEFORMATION ON SPCT OUTPUT

5.1 Introduction

The experimental results reported in Section 3.2, showed that prior plastic deformation can significantly alter the subsequent creep behaviour of a P91 steel at 600°C. Also, the microscopical investigations included in Chapter 4 indicated that, in a SPCT specimen, large plastic deformations occur at the beginning of the test, especially for higher load levels which induce large grain rotations in the material. Therefore, the effects of large plasticity on the output of the test need to be investigated in order to improve the understanding of the behaviour of the specimen.

In this Chapter, the results of the uniaxial pre-strained creep tests discussed in Section 3.2 will be used to develop a modified creep damage constitutive model that will be implemented in a FE model of a SPCT capable of accounting for the effects of initial plastic deformations on the subsequent creep response of the material. Finally, the numerical results obtained by use of the modified constitutive model will be compared with those obtained without the modification in the constitutive equations.

5.2 Small punch creep test FE modelling

5.2.1 Material constitutive model

As mentioned in Section 5.1, an elastic/plastic/creep constitutive model, capable of accounting for the effects of plastic deformations on subsequent creep material behaviour, was used for the FE analyses.

The true stress/strain curve was approximated from the engineering tensile curve obtained using a stress/strain test of a P91 steel at 600 °C, and it was implemented, in a tabular form, in the FE solver (ABAQUS). Table 5.1 reports the true stress/strain curve implemented in the FE calculations.

Table 5.1: Tabular form of the true stress/strain curve, for a P91 steel at 600 °C, implemented in ABAQUS. The stresses are expressed in [MPa] while the plastic strains are given in percentage.

σ [MPa]	ε_p [%]
275.0	0.00
275.9	0.63
281.2	0.65
283.9	0.67
288.4	0.78
297.0	0.95
294.5	1.13
292.9	1.29
296.1	1.63
301.9	3.22
299.3	4.25
298.5	5.44
300.0	8.24
305.0	11.58
340.0	29.29
365.0	40.00
390.0	52.03

The creep behaviour of the material was modelled by use of a modified Liu & Murakami constitutive model, which was implemented by use of a CREEP User Subroutine to be linked to ABAQUS for the analyses [19, 73]. The modified constitutive equations allow the effects of plastic pre-strain on the minimum creep rate and the failure life to be included and they were obtained by modifying the Liu&Murakami constitutive model, represented

by equations (2.27) and (2.28), by use of the ϕ and ψ parameters defined in Chapters 2 and 3 by equations (2.31) and (3.3), respectively. Equations (5.1) and (5.2) show the evolutions of creep strain rate (in multiaxial form) and of damage rate, respectively, of the creep constitutive model adopted for the FE calculations, where and σ_{RUP} is the rupture stress, defined by equation (2.25) in Chapter 2. In order to include the variations of ϕ and ψ with the plastic strain, equations (3.4) and (3.5) were also implemented in the constitutive model, while the maximum damage value was limited to ω_{MAX}=0.9901, in order to avoid numerical problems which arise when ω_{MAX} approaches unity. This value was chosen as a compromise between the accuracy of the solution, which is be optimised when ω_{MAX}=1, and the numerical costs of the analyses, which increase when and $\omega_{MAX} \rightarrow 1$.

$$\dot{\varepsilon}_{ij}^{c} = \frac{3}{2}\phi B \sigma_{EQ}^{n} \frac{S_{ij}}{\sigma_{EQ}} exp\left[\frac{2(n+1)}{\pi\sqrt{1+\frac{3}{n}}}\left(\frac{\sigma_1}{\sigma_{EQ}}\right)^2 \omega^{\frac{3}{2}}\right] \tag{5.1}$$

$$\dot{\omega} = \psi A_{LM} \frac{1 - exp[-q_2]}{q_2} \sigma_R^{\chi} exp[q_2 \omega] \tag{5.2}$$

In order to account for the loss of load carrying capability, due to material creep deterioration, the creep constitutive model is fully coupled with the elastic material properties [73]. The decrease of the stiffness of damaged elements with the increase of ω is governed by equation (5.3), where E_0 is the Young's modulus of undamaged material, and E is the instantaneous modulus corresponding to a damaged element.

$$E = E_0(1 - \omega) \tag{5.3}$$

Table 5.2 lists the elastic properties and the material constants for the Liu & Murakami creep constitutive model obtained from tests of a P91 steel at 600°C, in a none pre-strained condition, for the same composition and the same heat treatment used for the present study [92].

Table 5.2: Material constants for a P91 steel at 600°C, with stress [MPa] and time [h] [92].

E_0 [MPa]	ν	B	n	A_{LM}	χ	q_2	α_d
1.500×10^5	0.3	1.510×10^{-30}	11.795	2.120×10^{-27}	10.953	5.3	0.3

The correlations between the pre-strain levels and the ϕ and ψ parameters (given by equations (3.4) and (3.5), respectively) were obtained by using the experimental results, where strain levels were given by the engineering total strain for the specimen. In reality however, local strains (particularly in the necked regions) can be far greater than the average engineering strain of the uniaxial specimens discussed in Chapter 3. This is especially true for the high pre-strain level tests, therefore, in order to account for this mismatch and to implement a correlation between the true strains and the pre-strain parameters (i.e. ϕ and ψ) in the SPCT model, an additional FE calculation of a uniaxial tensile test of a P91 steel at 600°C was carried out by use of the tensile curve reported in Table 5.1. The model used for the additional FE calculation is shown in Figure 5.1, and it consists of 2974 axisymmetric quadrilateral elements. In view of the symmetry of the uniaxial creep test specimen (see Figure 3.1) just a half of its section was modelled. By using the geometry non-linear approach which updates the stiffness matrix of the structure at each time increment during the analysis, the uniaxial specimen FE model can take into account the large deformations and the necking occurring for large engineering strains. Figure 5.2 is a contour plot of the plastic equivalent strain, expressed in absolute value, for an engineering strain level of 0.122.

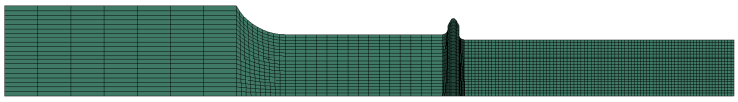

Figure 5.1: FE mesh used for the additional calculation of a uniaxial tensile test for a P91 steel at 600°C.

From the results of the additional FE analysis, the variation of the total engineering strain, $\varepsilon_{t,eng}$, was related to that of the true equivalent plastic strain, $\varepsilon_{p,true}$, in the necked section of the uniaxial specimen. Equation (5.4), was fitted to the FE results, with both $\varepsilon_{t,eng}$ and $\varepsilon_{p,true}$ expressed in absolute value, and the fitting constants are listed in Table 5.3. Figure 5.3 (a) shows the comparison of the experimental engineering stress/strain curve, obtained from a tensile test of a P91 steel at 600°C, with the corresponding numerical re-

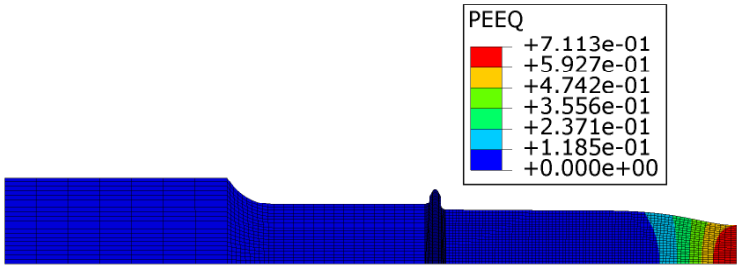

Figure 5.2: Contour plot of the equivalent plastic strain expressed in absolute value for an engineering strain of 0.122.

sults, while Figure 5.3 (b) shows the variation of the engineering total strain, $\varepsilon_{t,eng}$, with the plastic true strain, $\varepsilon_{p,true}$, obtained from the additional FE analysis, together with the plot of equation (5.4) with the fitting parameters of Table 5.3.

$$\varepsilon_{t,eng} = a_{corr}\varepsilon_{p,true} + b_{corr}\varepsilon_{p,true}^{m_{corr}} \tag{5.4}$$

Table 5.3: Fitting constants for equation (5.4).

a_{corr}	b_{corr}	m_{corr}
0.052	0.118	0.508

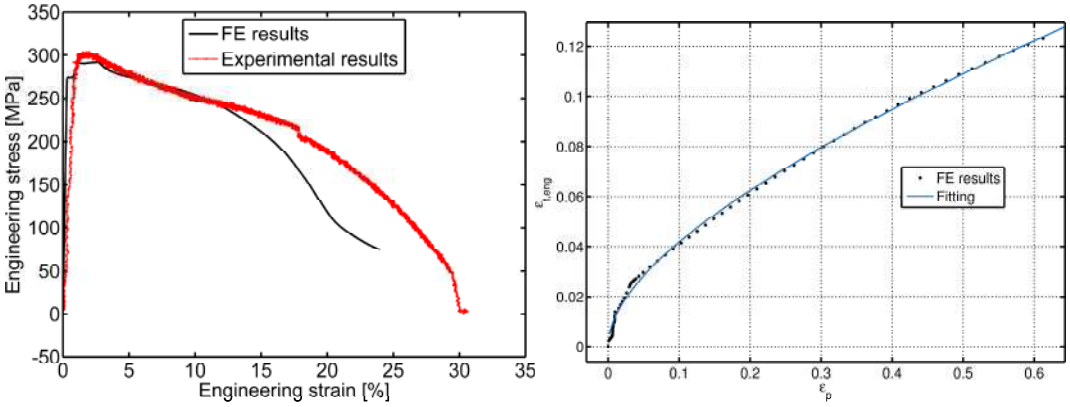

(a) (b)

Figure 5.3: Experimental and numerical engineering stress/strain curves (a) and variation of the engineering strain versus the true strain, in absolute value, obtained from the additional FE analysis of a tensile test for a P91 steel at 600°C (b).

5.2.2 Geometry, loads and boundary conditions of the SPCT FE model

In view of the symmetry of the problem, a 2D axisymmetric FE model was developed for the analyses, where the specimen was modelled as a deformable part while the punch, the support and the upper clamp were modelled as rigid bodies.

The geometry of the model conforms with the range of geometries recommended in the CWA 15627 draft code of practice by CEN [1] on small punch testing of metallic materials, with a specimen thickness, t_h, and diameter, D_{SPT}, of 0.5 and 8 [mm], respectively, punch radius, R_s, of 1.04 [mm], receiving hole radius, a_p, of 2 [mm] and lower clamp radius of 0.25 [mm]. Figure 5.4 (a) shows the solid model of a quarter section of the test rig, while Figure 5.4 (b) is the corresponding section with dimensions.

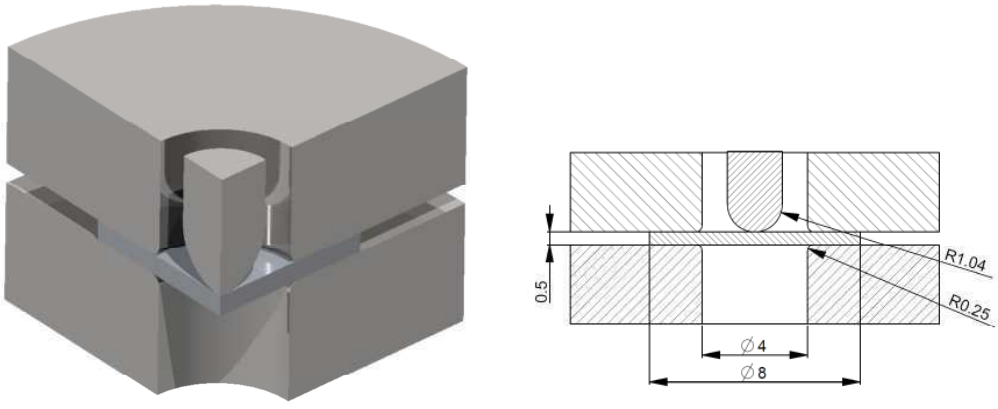

(a) (b)

Figure 5.4: SPCT configuration: (a) rendering of the section of the solid model; (b) dimensions of the test rig in [mm].

Three load levels, of 25, 28 and 30 [kg] respectively, were applied to the punch in the analyses and suitable boundary conditions were imposed to the degrees of freedom of the rigid bodies which model the components of the test rig. The radial and axial translations and the rotation around the axis of symmetry of the support were blocked. The horizontal translation and the rotation of the punch and of the upper clamp were also constrained. A load of 500 [kg] was applied to the point identifying the displacements of the rigid holder, in order to clamp the specimen between the two dies. Figure 5.5 schematically shows the loads and the boundary conditions applied to the model.

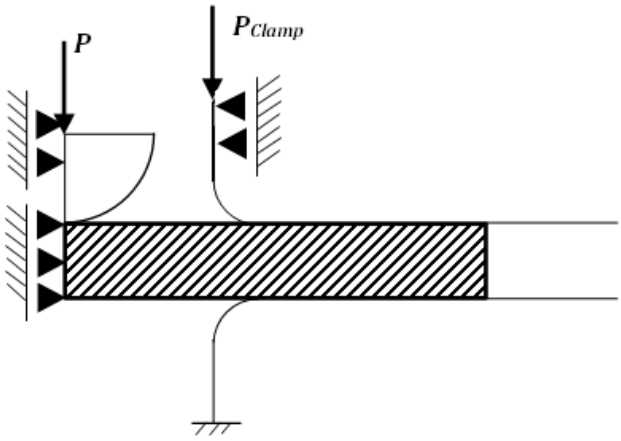

Figure 5.5: Loads and boundary conditions applied to the FE model of SPCT.

5.2.3 Element choice and meshing

Since the behaviour of the specimen is characterised by large incompressible deformations, due to creep, and by severe local loading conditions at the contact edge between the punch and the specimen, the FE mesh adopted to model the SPCT specimen consists of 883 nodes and 790 bilinear axisymmetric 4-node elements. Figure 5.6 shows the mesh used for the FE analyses.

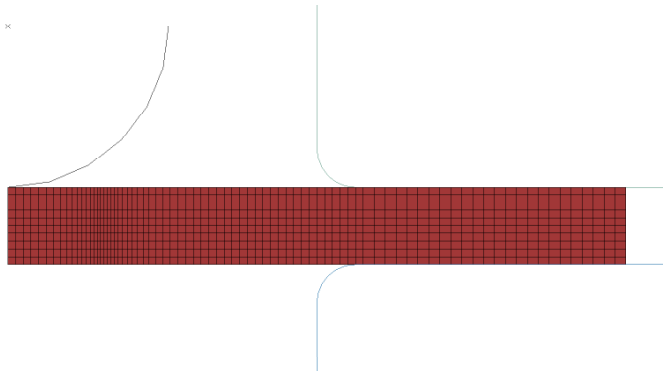

Figure 5.6: FE mesh used fotr the numerical calculations.

Quadratic elements (second order formulation) were avoided because, for the present work, they lead to a larger computational cost without producing any increase in the accuracy of the FE solutions as significant plastic deformations occur in the model. The reduced integration formulation was used, in order to avoid "locking" problems and convergence difficulties encountered when "fully integrated" linear elements were adopted. These

problems are due to a non-physical increase of the stiffness of the elements ("parasitic stiffness components" [19]) when bending deformation occurs, such as at the beginning of the creep step in the SPCT analyses, and generate the non-convergence of the solution. Hybrid formulation elements were adopted in order to avoid numerical singularities, which can occur when standard constant strain elements (such as the 4-node axis symmetric bilinear elements) are used with incompressible deformation fields. The hybrid formulation processes the pressure stress as an independently interpolated solution variable, coupled with the displacement solution [19]. Thus, unstable solutions for the displacement field after an infinitesimal increase of the pressure stress are avoided. In view of these requirements, the CAX4HR element type, available in ABAQUS, was used. The elements are refined near the edge of the unsupported region of the specimen, where significant bending deformation take place, and in the region close to the contact edge between the punch and the specimen, which was identified as the most critical location in the specimen [24, 72, 76].

5.2.4 Modelling procedure of the contact interaction

Surface-to-surface contact interactions have been used for all of the contacting pairs. The contact elements were automatically generated by the solver and consist of stiff springs which, once activated, apply the contact forces to the contact nodes on master and slave surfaces (see also ref. [70]). The activation of contact elements occurs when the interference between the contact nodes is less than the specified tolerance (0 in the present analyses). The stiffness of the contact elements varies non-linearly with the contact penetration, i.e. the non-linear penalty contact formulation was used, and it was found to be a critical feature of the FE analyses when material flow, due to plasticity and/or creep, is included, as it directly influences the convergence rate and the accuracy of the solution. Also the slip tolerance under stick conditions (identifying the stiffness of tangential contact elements) significantly affects the convergence rate of both the elastic/plastic and creep steps of the FE analysis. The Coulomb classical friction formulation was used and the friction coefficients were 0.3 and 0.8 for the punch/specimen and the punch/clamps interactions, respectively.

Furthermore, during the test, the small disc specimen undergoes severe changes in its

shape, since it gradually turns into a conical shape. In order to account for large deformation, the geometrical non-linearity formulation (GNL in ABAQUS) has been used for all of the analyses.

5.3 FE results and discussion

As mentioned in Section 5.2.2, elastic/plastic/creep damage FE analyses of SPCT were performed with three different punch loads, i.e. 25, 28 and 30 [kg]. The results obtained by using the modified Liu & Murakami constitutive model, reported in equations (5.1) and (5.2), were compared with those obtained without including the pre-straining effects, i.e. with ϕ=ψ=1 during the whole creep calculation.

Figure 5.7 shows the contour plots of the equivalent plastic strain at the beginning of the creep step. The peak plastic strains ranged from about 23%, for a punch load of 25 [kg], to about 29%, when the punch load was 30 [kg]. Therefore, the initial plastic strains are significant in the specimen for all of the load levels used in the calculations. When the load increases from 25 to 30 [kg], the location of the peak equivalent plastic strain moves from the region close to the punch/specimen contact interface to the bottom surface of the specimen, at approximately 0.5 [mm] from the axis of symmetry (see Figure 5.7).

The effects of initial plastic deformations on the creep behaviour of the material are shown in Figures 5.8 and 5.9, showing the contour plots of the ϕ and ψ parameters at the beginning of the creep step, respectively.

In the region close to the punch/specimen contact edge, which is characterised by the peak plastic deformation, the ϕ parameter is 1 when the punch load is 25 [kg], while it is larger than unity for higher load levels. Therefore, a creep enhancement of the material occurs in that region for loads of 28 and 30 [kg]. The region on the middle plane of the specimen, close to the clamps, exhibits ϕ=1 for all of loads levels used in the calculations because it corresponds to the neutral plane of bending deformation, where the material is not plastically deformed at the beginning of the test for any of the load levels adopted (see

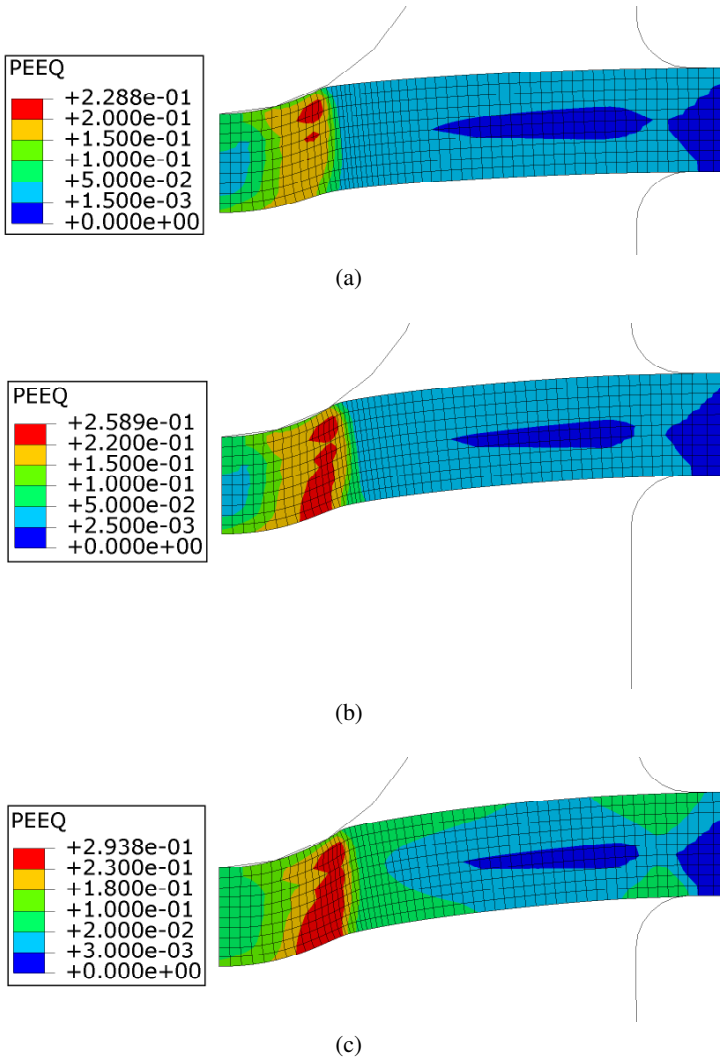

Figure 5.7: Contour plots of the initial equivalent plastic strains for punch loads of (a) 25, (b) 28 and (c) 30 [kg].

also Figure 5.7 for comparison), and, for $\varepsilon_{p,pre}$=0, equation (3.4) leads to ϕ=1. The material surrounding this area of the specimen exhibits relatively small plastic strains, showing creep resistance effects (ϕ<1) for all of the load levels.

The variation of ψ shows that, due to plastic strains, the creep damage rate is enhanced in the area close to the punch/specimen contact edge (ψ>1). A resistance effect is observed in the unsupported region, between the punch and the clamps (ψ<1). In Figure 5.9, the region of material on the middle plane of the specimen, close to the clamps, is characterised by ψ=1 for all of load levels because, in this region, ε_p=0 (see Figure 5.7), and equation (3.5) leads to ψ=1 for ε_p=0. In the clamped region of the specimen the material

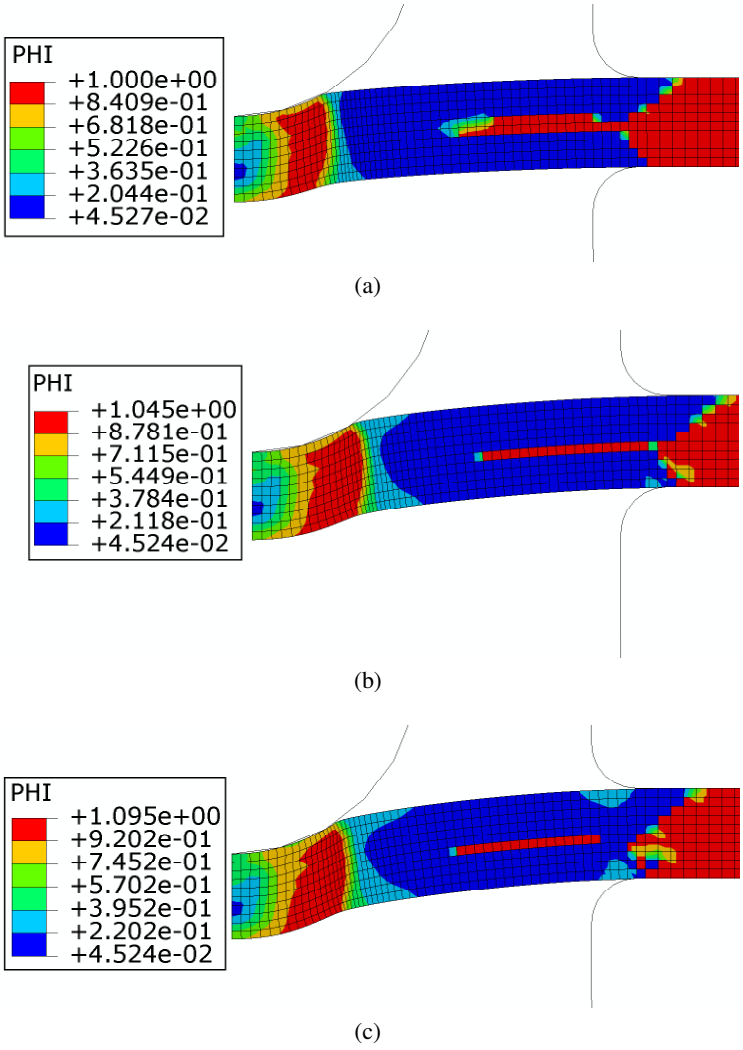

Figure 5.8: Contour plots of the ϕ parameter for punch loads of (a) 25, (b) 28 and (c) 30 [kg].

does not experience any significant plastic deformation, therefore ϕ=ψ=1.

Figure 5.10 shows the punch displacement variation versus time obtained, for the three load levels, by use of the modified constitutive model. The results are also compared with the analogous FE analyses performed without including any pre-straining effect.

From the results reported in Figure 5.10, when the effects of initial plastic deformation on the creep response of the specimen are taken into account, a global creep resistance effect can be observed, with a significant decrease of the minimum displacement rate and an increase of the time to failure, compared to the results of the analyses obtained without the inclusion of pre-straining effects. The global creep resistance of the specimen is related to

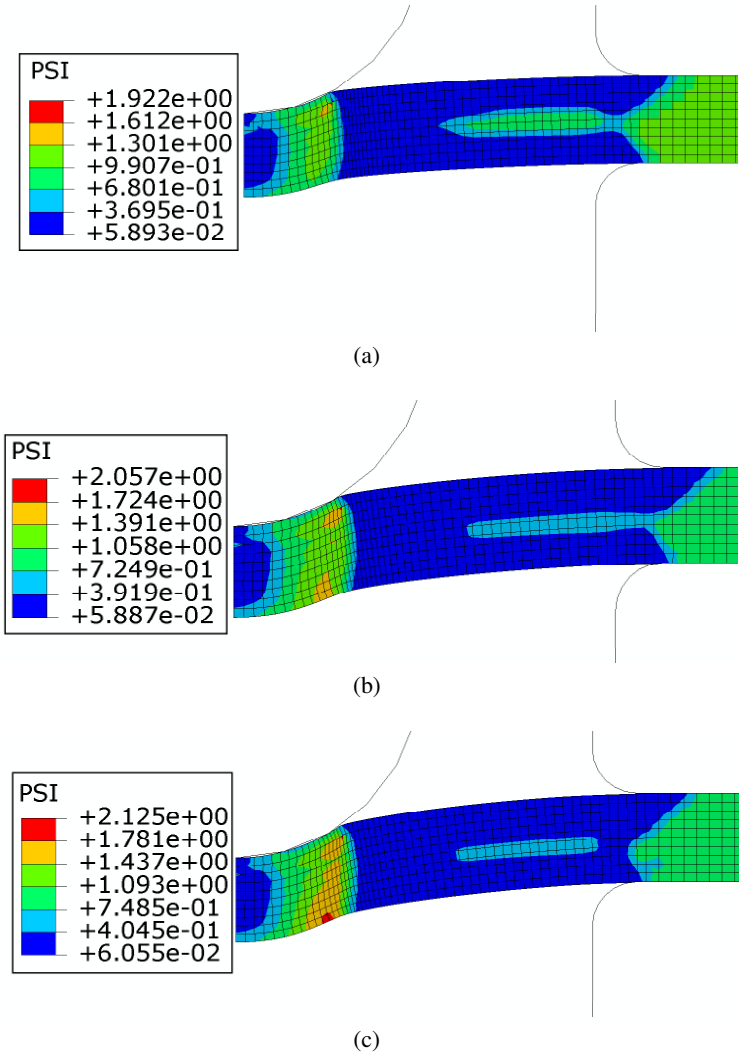

Figure 5.9: Contour plots of the ψ parameter for punch loads of (a) 25, (b) 28 and (c) 30 [kg].

the fields of the ϕ and ψ parameters, which show values less than 1 in most of the specimen, except from the region close to the contact edge between the punch and the specimen.

Figure 5.11 shows a comparison of contour plots of creep damage for a punch load of 25 [kg]. These plots show the results obtained with the modified constitutive model at 25% of the failure life (i.e. 462 [h]) and those of the FE analysis without the inclusion of the plastic deformation effects at the same failure life fraction, which is 42 [h] in this case.

It should be noted that the high damage locations indicated in Figure 5.11 are compatible with the region of the specimen where crack initiation and propagation was found during the interrupted tests discussed in Chapter 4, see Figure 4.7.

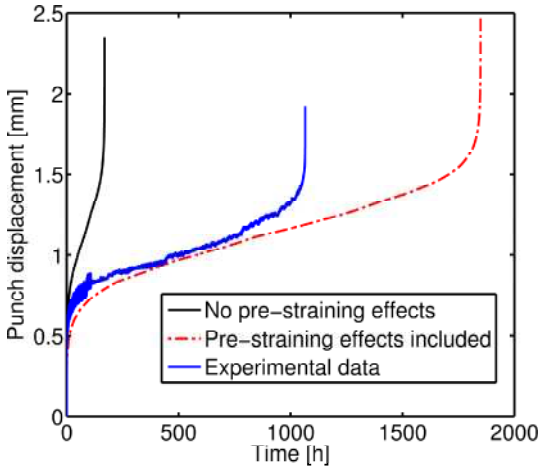

(a)

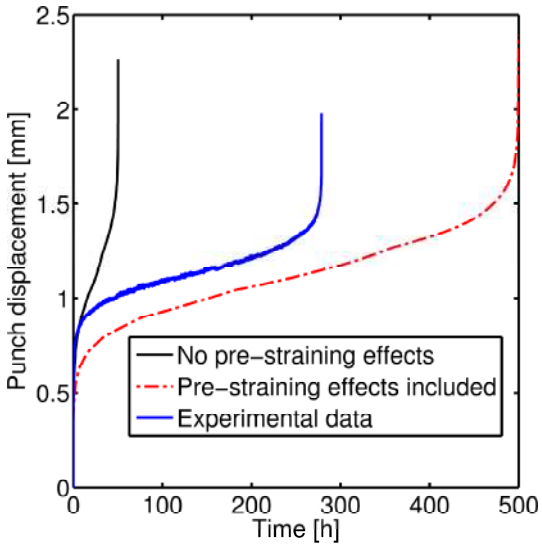

(b)

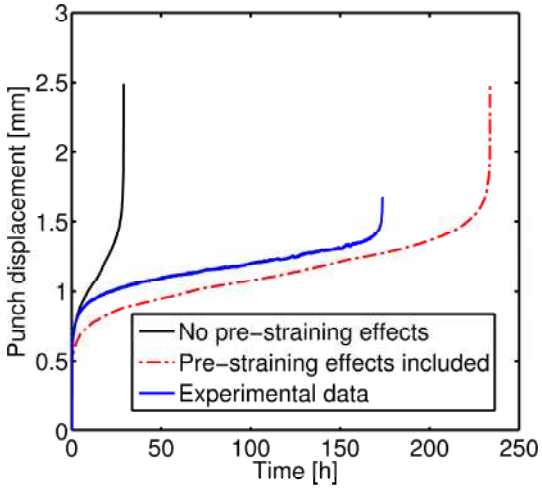

(c)

Figure 5.10: Variation of the punch displacement versus time with punch loads of (a) 25, (b) 28 and (c) 30 [kg].

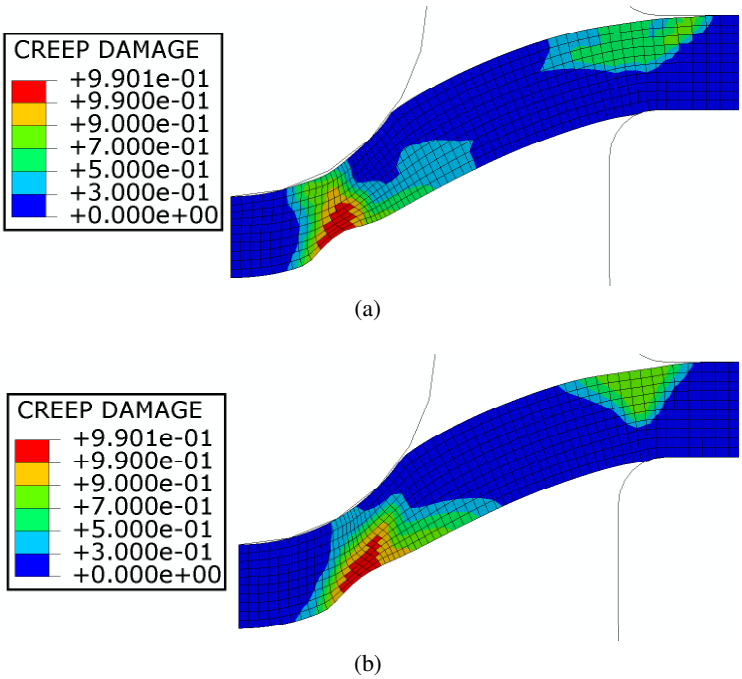

Figure 5.11: Contour plots of creep damage at 25% of the failure life for a load of 25 [kg] (a) with and (b) without including the effects of initial plastic deformations on material creep behaviour.

The results of the FE calculations show that the peak damage location is, in both cases, near the bottom surface of the specimen, near the contact edge between the punch and the specimen, similarly to the results reported in refs. [29, 72]. The region where peak damage is located, defined in refs. [24, 76] as the most critical location of the specimen, exhibits a global creep enhancement, and the region where the elements are fully damaged is larger when the plastic deformation effects are considered. The propagation of the high damage region is not identical in both cases, as a result of different creep damage evolution properties, generated by plastic deformation, in the various elements of the model when initial plasticity effects are included.

When the effects of pre-straining are taken into account, the damage level in the region close to the clamps is lower than that obtained from the non-modified Liu & Murakami constitutive model, since the elements in that area exhibit a creep resistance effect and the damage rate evolution process becomes slower.

In spite of the larger high damaged region found at 25% of the failure time, the analyses with the inclusion of the plastic deformation effects show a global creep resistance,

because the global behaviour of the specimen is governed by the combination of creep resistance effects, occurring in most of the specimen for this load level, and creep enhancement effects, found in the critical region of the specimen. For the loads of 28 and 30 [kg], a creep resistance effect was also observed because ϕ and ψ are less than unity in the majority of the specimen, as Figures 5.8 and 5.9 show.

Tables 5.4 and 5.5 show the comparison between the numerical results obtained by the FE analyses, performed with and without pre-straining effects, and the corresponding experimental results, discussed in Chapter 3.

Table 5.4: Comparison of the minimum displacement rates (MDR), expressed in [mm/h], obtained from the FE analyses with and without pre-straining effects included and experimental results reported in Chapter 3.

Load [kg]	FE MDR no pre-straining	FE MDR with pre-straining	Experimental MDR
25	3.621×10^{-3}	3.214×10^{-4}	4.638×10^{-4}
28	1.032×10^{-2}	9.643×10^{-4}	1.160×10^{-3}
30	1.736×10^{-2}	2.057×10^{-3}	2.150×10^{-3}

Table 5.5: Comparison of the times to failure, expressed in [h], obtained from the FE analyses with and without pre-straining effects included and experimental results reported in Chapter 3.

Load [kg]	FE t_f no pre-straining	FE t_f with pre-straining	Experimental t_f
25	169.0	1848.3	1066.0
28	50.4	499.8	278.7
30	29.0	233.8	173.7

CHAPTER 6

EFFECTS OF GEOMETRICAL INACCURACIES OF THE EXPERIMENTAL SET-UP ON SMALL PUNCH CREEP TEST RESULTS

6.1 Introduction

One of the limitations discussed in Chapter 2 concerns the test repeatability, as the experimental results are geometry dependent and a significant amount of scatter was found in the experimental results [27–29].

In this Chapter, the results of elastic/creep finite element analyses for the SPCT geometry, using two different creep constitutive models, i.e. a Norton's law and the Liu & Murakami creep damage model, are reported. The results have been used to investigate the effects of inaccuracies in the initial position of the punch and in the loading direction, both of which can affect the overall response of the SPCT, and therefore, the test repeatability.

6.2 Finite element model used for the analyses

In contrast to the model described in Chapter 5, the problem discussed in this Chapter includes situations in which the loading conditions are not axisymmetric, therefore, a 3D FE model of a small punch creep test is needed for the numerical calculations. The test rig components, i.e. the punch, the upper clamp and the support, were modelled as rigid bodies, while the specimen is allowed to deform as an elastic/creep part.

6.2.1 Material behaviour model, loading and boundary conditions

The Norton creep law used in the present analyses is represented in Chapter 2 by equation (2.19), in the multi-axial form.

Although a constitutive model which was capable of taking into account creep damage, plastic deformations and their effects on the creep behaviour of the material (as that used in the simulations discussed in Chapter 5) would be more accurate for the SPCT FE modelling, the Norton creep approximation is acceptable for the present investigation, since only the relative effects of different loading conditions and geometrical configurations, on the behaviour of the specimen, are analysed in this case.

Furthermore, in order to evaluate the application of the secondary-creep approximation, an additional set of FE analyses was performed using the Liu & Murakami creep damage model, which is reported in in Chapter 2 by equations (2.25) and (2.27), (2.28) [73]. Also in these calculations, in order to avoid possible computational problems, the maximum damage value was limited to ω_{MAX}=0.9901. The reduction of the load carrying capability of damaged elements is represented by equation (5.3), also reported below.

$$E = E_0(1 - \omega)$$

Table 6.1 shows the Poisson's ratio, ν, the Young's modulus for undamaged material, E_0, and the material creep constants for the Norton and Liu & Murakami constitutive models, obtained for a P91 steel at 650°C, with the stress in [MPa] and time in [h] [68].

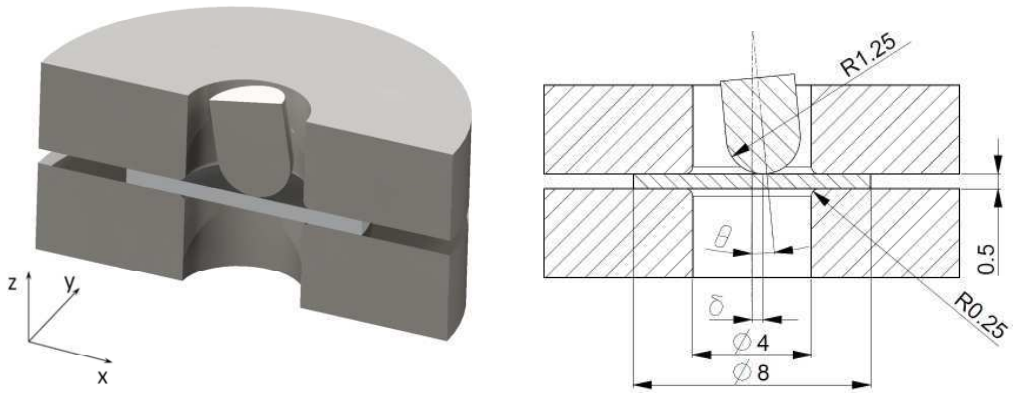

(a) (b)

Figure 6.1: (a) Meridional section of the test set-up with the x-z cutting plane and (b) geometric dimensions in [mm].

The non-linear geometry formulation was used because the specimen exhibits large deformations and a significant shape change during the creep analyses.

Table 6.1: Material constants for a P91 steel at 650°C, with stress [MPa] and time [h] [68].

E_0 [MPa]	ν	B	n	A_{LM}	χ	q_2	α_d
1.500×10^5	0.3	1.092×10^{-20}	8.462	2.952×10^{-16}	6.789	3.2	0.215

In Figure 6.1, the section of the test set up and the relevant dimensions are shown; the x-z plane is the cutting plane. Also in this case, the dimensions of the test set-up conform with the CEN draft code of practice CWA 15627 [1], with a punch radius, R_s, of 1.25 [mm], a receiving hole radius, a_p, of 2 [mm], a specimen thickness, t_h, of 0.5 [mm] and a specimen diameter, D_{SPT}, of 8 [mm].

The initial position of the punch has been varied for each analysis. The distance, δ, of the initial punch/specimen contact point from the symmetry axis of the test set-up ranges from 0 to 0.3 [mm] (see Figure 6.1). Figure 6.2 shows the loads and the boundary conditions applied to the model on the x-z plane. The axis of the punch is in the x-z plane in all of the analyses and this was rotated, with respect to the axis of symmetry of the test rig, by varying the angle, θ, from 0 to -3°. The θ angle has been shown as a negative value, being opposite to the positive direction of the y-axis (see Figures 6.1 and 6.2). The punch was constrained so that it can only translate along the direction of its axis by blocking all three

of the rotational degrees of freedom and the translation in the y-direction.

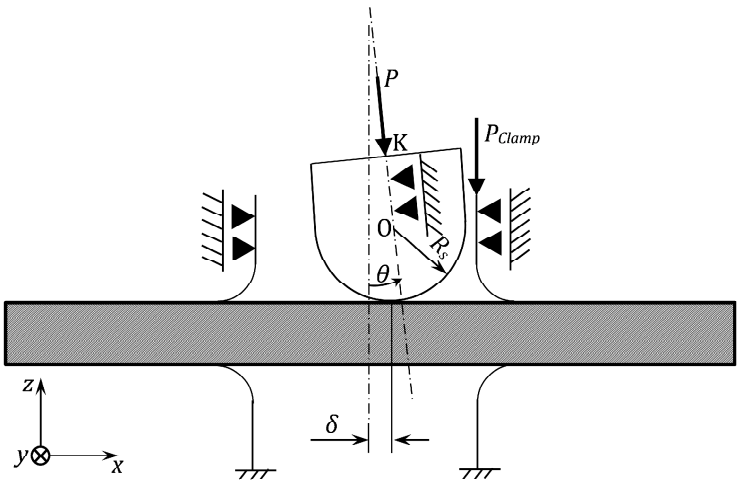

Figure 6.2: Schematic diagram showing the loads and boundary conditions in the x-z plane.

For θ<0 (see Figure 6.2), the constraint represented by equation (6.1) has also been applied to the punch. It relates the horizontal and vertical displacements of the punch, u_x and u_z, respectively, to the θ angle. For the case with θ=0, the horizontal translation of the punch, u_x, has been constrained by equation (6.2).

$$u_z - tan\left(\frac{\pi}{2} - \theta\right) u_x = 0, \;\; \theta < 0 \tag{6.1}$$

$$u_x = 0, \;\; tan(\theta) = 0 \tag{6.2}$$

A constant load has been applied to the punch during the creep analyses. In all cases, the load direction is coincident with the axis of the punch and the magnitude of the load is 220 [N].

The components of the punch load in the x- and z- directions, P_x and P_z, are given by equations (6.3) and (6.4), respectively.

$$P_x = -P \sin\theta \tag{6.3}$$

$$P_z = -P\cos\theta \tag{6.4}$$

Surface-to-surface contact boundary conditions were used to model the interactions of the specimen with the punch, the support and the holder were modelled. Similarly to the model reported in Chapter 5, a non-linear penalty formulation was chosen for the normal behaviour of all of the interactions, while, for the tangential behaviour, the classical Coulomb friction theory was adopted. The friction coefficient of the punch/specimen interaction was assumed to be 0.3, while, for the support/specimen and the holder/specimen interactions, the friction coefficient was taken to be 0.8. As discussed in Chapter 2, this model is an approximation to the actual behaviour because the friction coefficient depends on various factors which characterise the local loading conditions, the status of the contact surfaces, and the material properties of the contacting bodies. However, for the analyses reported in this Chapter, the classical Coulomb theory can be considered to be acceptable because it is the relative results, corresponding to various loading conditions that are under investigation, and not the absolute values.

6.2.2 Choice of the element type and meshes

As mentioned in Chapters 2 and 5, the behaviour of the specimen is characterised by large incompressible deformations, in this case due to only creep, and severe local loading conditions at the contact edge between the punch and the specimen. When complicated loading conditions are present, especially with load singularities such as those induced by contact loads, first order elements (characterised by a constant strain), rather than quadratic elements, are generally recommended, see e.g. ref. [19]. If quadratic elements are used with a complicated stress field within the model, the linear approximation of stresses and strains within a single element can generate convergence difficulties or inaccuracies in the solution in correspondence to the loading singularities [19]. Alternatively, if linear elements are adopted, these problems can be avoided because of the constant stress formulation [19]. Generally, quadratic elements are preferred with bending dominant loading modes, or where

the stress field varies 'smoothly' in the model [19]. In view of the complexity of the loading conditions acting on the small disc specimen, 3D 8-nodes hexahedral first order elements were chosen with a reduced integration formulation, which was used to avoid 'locking' problems and convergence difficulties which may be encountered when 'fully integrated' linear elements are adopted.

For the 3D FE calculations, hybrid element formulation were chosen because numerical singularities can occur when constant strain elements are used with incompressible deformation fields (see also Section 5.2.3). In view of these requirements, the C3D8RH element type, available in ABAQUS, was chosen.

The FE results were found to be sensitive to the element size in the critical regions of the specimen, i.e. the punch/specimen contact edge and the zone adjacent to the clamped region.

Different meshes were studied, and the solution obtained with the 3D model, with δ=θ=0, was compared with that of a corresponding 2D axisymmetric model. The element sizes of the critical regions were chosen so that, between the 2D and the 3D solutions, the location of the peak levels of the von Mises equivalent stress were consistent and their difference was within a few percentage points.

The FE mesh developed for the numerical analyses is focused in the region of the initial contact point between the punch and the specimen, thus slightly different meshes have been adopted for various punch misalignments, δ. The number of elements are similar for all of the analyses, ranging from 111,675 for δ=0 to 111,630 for δ=0.3 [mm]. Figure 6.3 shows the meshes adopted for δ=0 and δ=0.3 [mm].

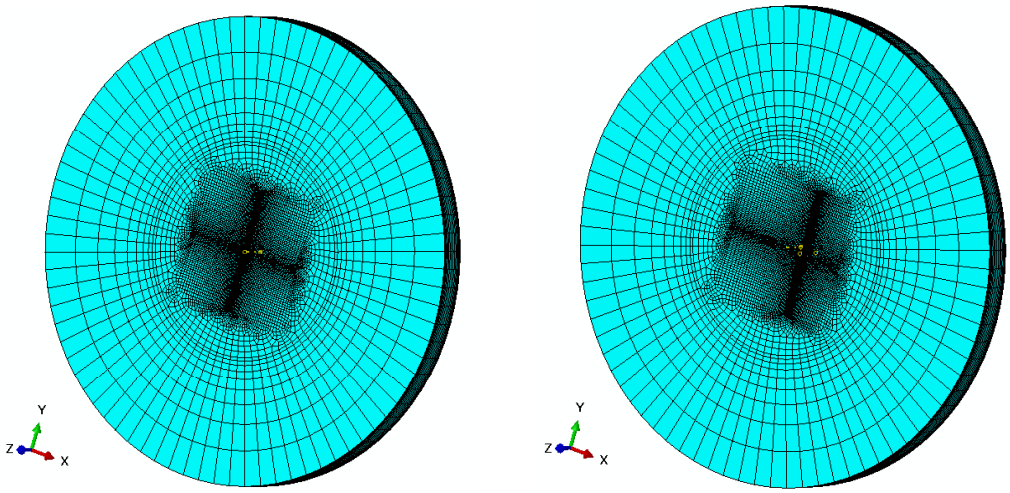

(a) (b)

Figure 6.3: Meshes adopted for δ=0 (a) and δ=0.3 [mm] (b).

6.3 Results and discussion

6.3.1 Illustrative behaviour

Elastic/secondary creep FE analyses of a SPCT specimen were performed taking into account the various loading conditions. Figure 6.4 shows a plot of the punch displacement versus time, for the case in which the punch is centred on the surface of the specimen (i.e. δ=0) with its axis parallel to that of the test set-up (i.e. θ=0°).

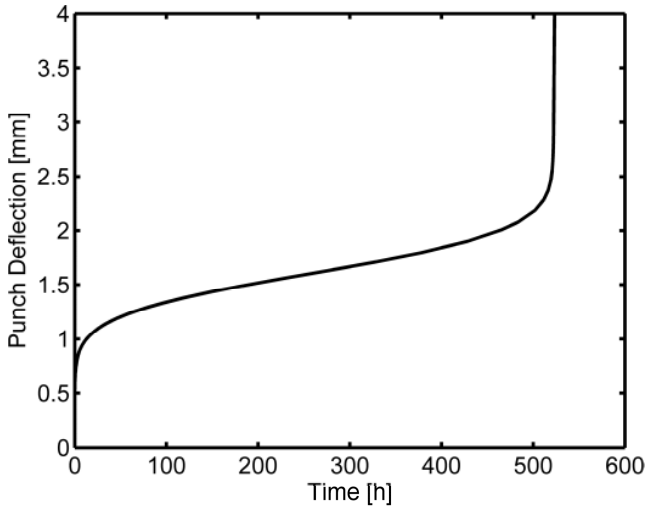

Figure 6.4: Plot of the punch displacement versus time obtained with δ=0 and θ=0°.

Also the plot shown in Figure 6.4 can be divided into three typical SPCT regions, after

the relatively large initial deformation, in agreement with the results of Chapter 5 and those of experimental and numerical investigations reported in the literature (see Section 2.6.4). However, in the model discussed in this Chapter, no initial plasticity is accounted for and the initial response of the specimen is taken to be purely elastic.

6.3.2 Effects of punch positioning and concentricity

FE analyses were performed with various configurations of the punch load. They are defined by the distance, δ, between the initial punch/specimen contact point and the specimen's centre, and the angle, θ, between the axis of the punch and the axis of the test set rig (see also Section 6.2). Figure 6.5 contains plots of the punch displacement versus time, for various values of δ, with the axis of symmetry of the punch being parallel to that of the test set-up (i.e. θ=0°).

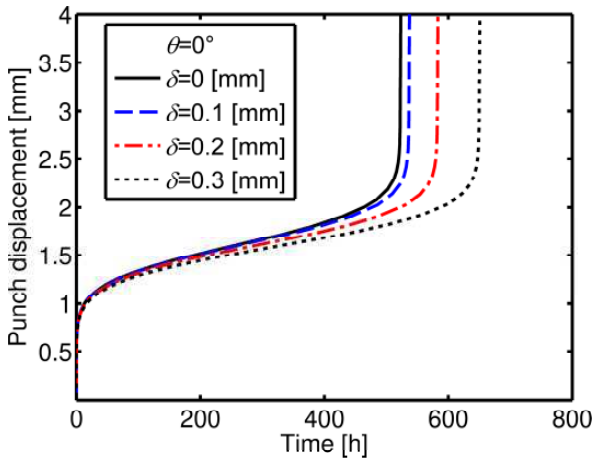

Figure 6.5: Punch displacement versus time for various values of δ, with θ=0°.

From Figure 6.5, it can be seen that, the minimum displacement rate (*MDR*) decreases and the failure time (t_f) increases as the load eccentricity is increased. This is a result of the change in stiffness at various load points of the specimen, related to the bending and membrane stretching deformation modes. The central region of the specimen is characterised by the minimum bending stiffness, because the centre of the disc, where δ=0, is at the maximum distance from the supports. Since bending deformation governs the initial stages of the SPCT, when the punch load, acting in the through-thickness direction, is applied in this

position, it generates the maximum initial central deflection in the specimen. As a consequence, when the loading eccentricity increases, i.e. δ>0, the deformation of the specimen becomes smaller.

As creep proceeds, the specimen becomes approximately conical in shape, and membrane stretching of the annular region close to the punch/specimen contact edge becomes the governing mechanism. Bending also occurs in the region near the supports but, at this stage of the test, it has a much smaller effect than that of the membrane stretching which occurs at the contact edge on the global deformation of the specimen.

When the punch is in the centred configuration (δ=0), the annular region undergoing membrane stretching has a uniform meridional length over the circumferential direction, while, for the eccentric loading configurations (δ>0), the distance between the loading region and the supports is not constant. In view of the material continuity conditions, the region of the specimen where the punch is closest to the supports, characterised by the minimum meridional length, governs the global creep deformation of the specimen. Therefore, in view of the geometry of the problem, when δ increases, the size of the region governing creep deformation is smaller than that corresponding to the axisymmetric case with δ=0.

Figure 6.6 shows the contour plots of the maximum principal stress, σ_1, on a section of the specimen (where the cutting plane is x-z), with θ=0, for (a) δ=0 and (b) δ=0.3 [mm] at creep times of 278.5 and 407.9 [h], respectively. In the annular region around the punch/specimen contact area, σ_1 is predominantly that of a meridional membrane stress situation. The two loading configurations of Figure 6.6 exhibit similar peak values of σ_1 during the secondary region of the SPCT curve. The location where the stress field is most severe is on the bottom surface of the specimen, near the specimen/punch contact edge, in the critical region which was also pointed out in Chapters 2-5.

Since Norton's constitutive model is used, the creep strain rate is governed by the stress state. The local creep strain rate field is similar for the two configurations of Figure 6.6, but, when δ=0, the global creep deformation is larger, because the region of the specimen which governs the creep deformation, i.e. the annular region where membrane

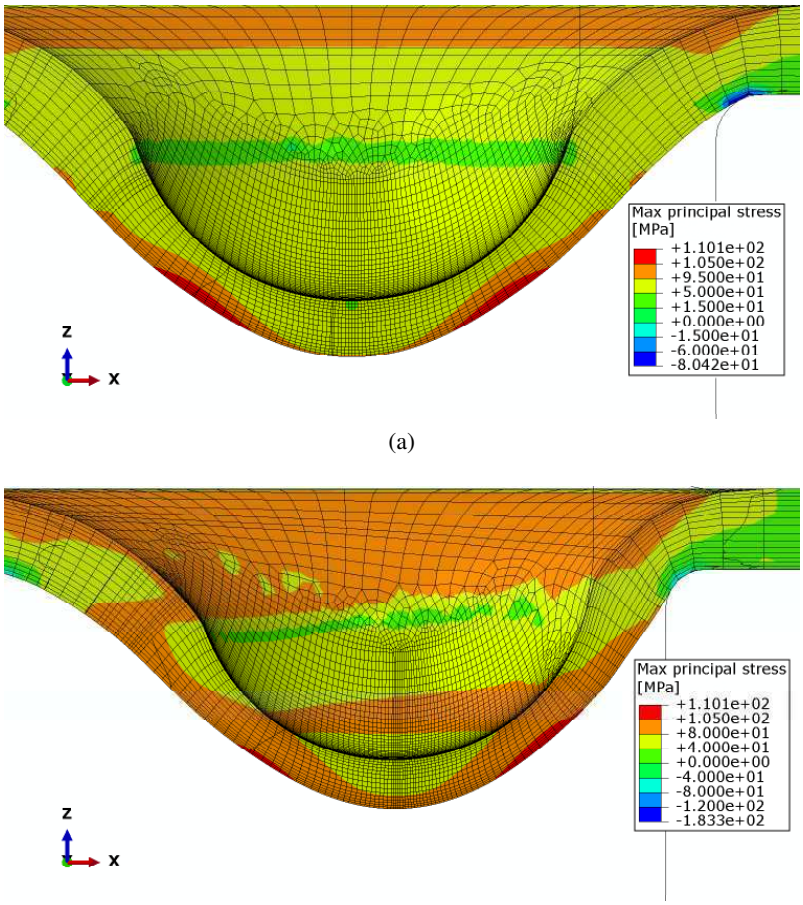

Figure 6.6: Contour plots of the maximum principal stress (a) δ=0 and t=278.5 [h]; and (b) δ=0.3 [mm] and t=407.9 [h], with θ=0°.

stretching takes place, is larger than in the asymmetric load case. Also the time to failure, defined in this Section as the creep step time at which the solution did not converge, is affected by δ (see Figure 6.5). When the effects of material creep damage are not included in the SPCT FE model, the stage of the punch displacement curve characterised by increasing deformation rate is governed by geometrical softening only, that is, necking in the critical region of the specimen. When δ increases from 0 to 0.3 [mm], the global creep deformation, and necking, of the specimen exhibits a lower rate, hence the time to failure increases.

Figure 6.7 shows the variations of the punch displacement with time for different values of θ, with δ=0 and δ=0.3 [mm]. For a given value of δ, the test output changes with θ because the stiffness of the specimen increases when the load is not parallel to the axis of the test rig, i.e. when $\theta \neq$0. For δ=0, the θ angle does not significantly affect the SPCT

output, as shown in Figure 6.7 (a), while, when δ increases, the effect of θ becomes more marked (see Figure 6.7 (b)).

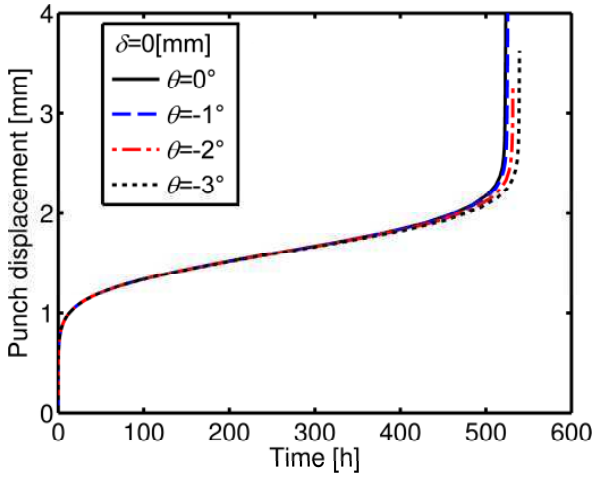

(a)

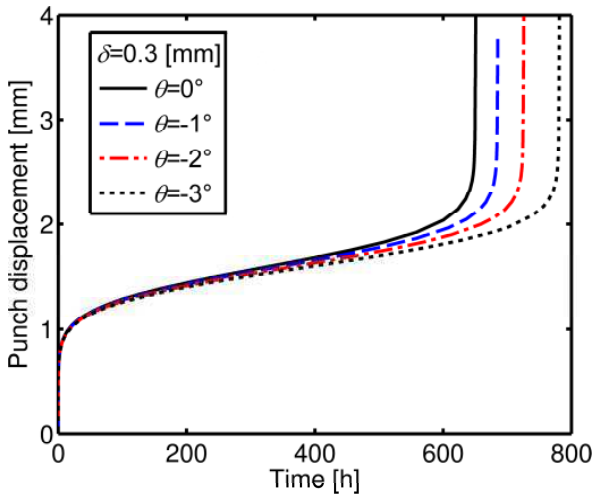

(b)

Figure 6.7: Plot of the punch displacement versus time for different θ values, with (a) δ=0 and (b) δ=0.3 [mm].

Figure 6.8 represents the contour plots of σ_1 on a cross section of the specimen, where the cutting plane is x-z. Also for Figure 6.8, σ_1 can be considered as a close approximation of the meridional membrane stress component in the proximity of the punch/specimen contact edge.

When the loading direction is not parallel to the axis of the test rig, i.e. $\theta \neq 0$, the component of the load that generates the increase of the global deformation of the specimen, i.e. P_z, decreases, while P_x increases (see equations (6.3) and (6.4)). When Figure 6.6

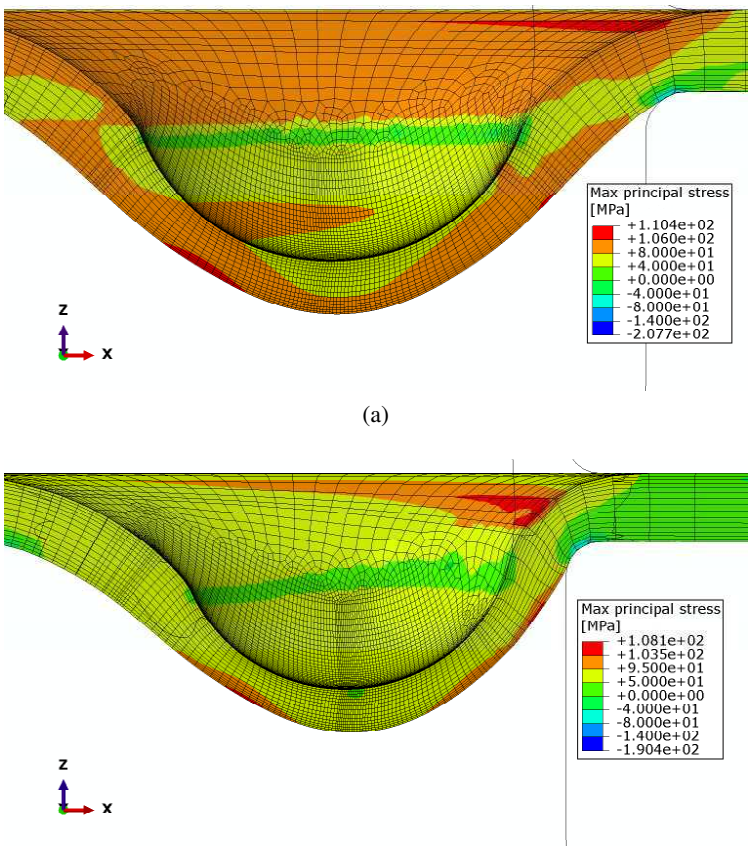

Figure 6.8: Contour plot of the maximum principal stress for θ=-3° with (a) δ=0 and (b) δ=0.3 [mm], at creep times of 217.6 and 378.6 [h], respectively.

(a) is compared with Figure 6.8 (a) (i.e. for δ=0), it can be observed that, when $\theta \neq 0$ the level of σ_1 slightly reduces in the region close to the punch/specimen contact edge, although the peak values exhibits a small increase. By comparing Figures 6.6 and 6.8 (b) (i.e. for δ=0.3 [mm]) it can be seen that, when the punch is in a non-centred position, the variation of the loading direction produces a more significant decrease of the level of σ_1 in the critical region of the specimen. The reduction of the stress level in the vicinity of the punch/specimen contact edge affects the test output, by reducing the creep rate and, in turn, the *MDR* and by increasing the time to failure of the specimen. Since the stress level reduction is larger when δ=0.3 [mm], the effects of the variation of θ on the test output are more significant.

When the punch is eccentric with respect to the specimen centre and the load does not act along the z-direction, i.e. $\delta \neq 0$ and $\theta \neq 0$, the effects of δ and θ, on SPCT output,

are combined (as Figure 6.7 (b) shows).

In order to investigate these effects, the minimum displacement rate obtained from the FE analyses, with θ ranging from 0 to -3° and δ from 0 to 0.3 [mm], was normalised with respect to MDR_0, that is the minimum displacement rate corresponding to the configuration with θ=0° and δ=0 [mm]. The variation of (MDR/MDR_0) versus θ and (δ/t_h), where t_h is the specimen thickness, is plotted in Figure 6.9. A third order polynomial surface, represented by equation (6.5), which is also plotted in Figure 6.9, has been fitted to the FE results and it has a correlation factor of R^2=0.994. The dimensionless fitting constants, p_{ij}, with *i*=0,1,2,3 and *j*=0,1,2, used in equation (6.5), are listed in Table 6.2.

$$\frac{MDR}{MDR_0} = 1 + p_{10}\theta + p_{01}\frac{\delta}{t_h} + p_{20}\theta^2 + p_{11}\theta\frac{\delta}{t_h} + p_{02}\left(\frac{\delta}{t_h}\right)^2 + p_{30}\theta^3 + p_{21}\theta^2\frac{\delta}{t_h} + p_{12}\theta\left(\frac{\delta}{t_h}\right)^2 \tag{6.5}$$

Table 6.2: Dimensionless constants used in equation (6.5) for the normalised *MDR* surface fitting.

p_{10}	p_{01}	p_{20}	p_{11}
2.254×10^{-2}	-2.003×10^{-2}	1.678×10^{-2}	0.151

p_{02}	p_{30}	p_{21}	p_{12}
-0.764	3.898×10^{-3}	-1.344×10^{-2}	-0.276

Figure 6.9 shows that the effect of θ on the test output increases when δ increases.

The failure time is also influenced by the loading configuration (see Figure 6.7). Figure 6.10 plots the variation of the normalised time to failure (t_f/t_{f0}) where t_{f0} is the failure time corresponding to the "base configuration" (i.e. θ=0° and δ=0), versus θ and (δ/t_h).

Also in this case, a third order polynomial surface has been fitted to the FE results. The surface is represented by equation (6.6) and it is also plotted in Figure 6.10. The correlation factor for the fitting of (t_f/t_{f0}) is R^2=0.9998, while the dimensionless constants,

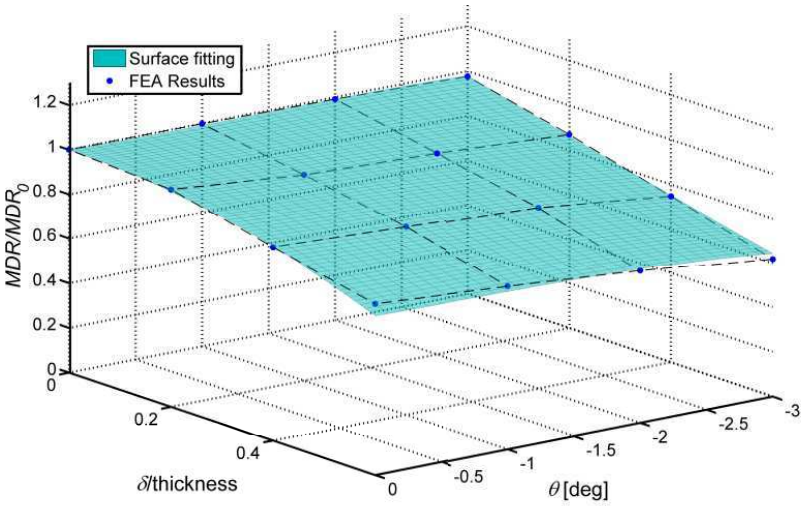

Figure 6.9: Variation of the normalised *MDR* versus θ and normalised δ.

q_{ij}, with *i*=0,1,2,3 and *j*=0,1,2, used in equation (6.6), are listed in Table 6.3.

$$\frac{t_f}{t_{f0}} = 1 + q_{10}\theta + q_{01}\frac{\delta}{t_h} + q_{20}\theta^2 + q_{11}\theta\frac{\delta}{t_h} + q_{02}\left(\frac{\delta}{t_h}\right)^2 + q_{30}\theta^3 + q_{21}\theta^2\frac{\delta}{t_h} + q_{12}\theta\left(\frac{\delta}{t_h}\right)^2 \tag{6.6}$$

Table 6.3: Dimensionless constants used in equation (6.6) for the normalised t_f surface fitting.

q_{10}	q_{01}	q_{20}	q_{11}
-8.540×10^{-3}	-8.653×10^{-3}	-4.435×10^{-3}	-6.929×10^{-2}

q_{02}	q_{30}	q_{21}	q_{12}
0.738	-1.630×10^{-3}	8.621×10^{-3}	-2.921×10^{-2}

When the loading configuration corresponding to the "least accurate" test setting, i.e. δ=0.3 [mm] and θ=-3°, is compared with the "base configuration", the minimum displacement rate is reduced by almost 40%, while the failure time increases by approximately 50%. However, Figures 6.9 and 6.10 also show that the effects of the punch positioning and loading direction are not significant for smaller magnitudes of δ and θ, since the reduction of *MDR* and the increase of t_f are less than 10% for $\delta \leq$0.2 [mm] and $|\theta|$<2°. This means

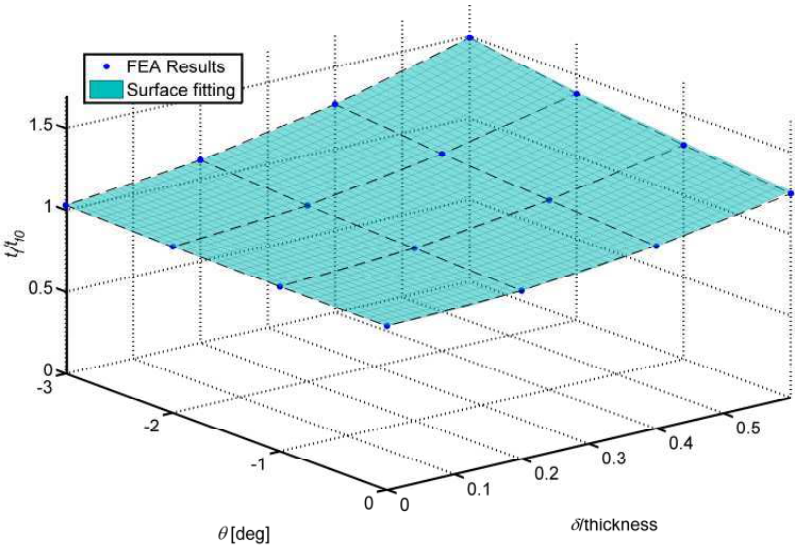

Figure 6.10: Variation of the normalised time to failure versus θ and normalised δ.

that any inaccuracies related to likely punch loading positions will not significantly affect the experimental results for the majority of the range investigated, but can lead to major deviations when δ and $|\theta|$ are on the bounds of the ranges adopted in these calculations.

6.3.3 Additional damage FE calculations

Additional FE analyses have been carried out by using the Liu & Murakami creep constitutive model (see Chapter 2, equations (2.25) and (2.27)-(2.28)) with the material constants reported in Table 6.1. For computational cost reduction, a relatively coarse mesh has been adopted for damage FE analyses, consisting of 30,525 elements of the same type as that used for Norton's creep law analyses, and 33,219 nodes. This mesh leads to stress fields comparable with those of the steady-state analyses reported in Section 6.3.2 and the peak damage location matches the experimental findings discussed in Chapter 4.

The results obtained by using the symmetric loading conditions, i.e. with δ=0 [mm] and θ=0°, were compared with those obtained by adopting the maximum punch eccentricity and misalignment, i.e. δ=0.3 [mm] and θ=-3°. Figure 6.11 is the plot of the punch displacement versus time, for the two loading configurations adopted in the damage mechanics FEAs. The effects of the punch eccentricity and misalignment obtained by using

the Liu & Murakami constitutive model are comparable with those obtained by steady-state creep calculations. When the punch load is not axisymmetric, the deformation rate of the specimen decreases and the failure time increases with respect to the axisymmetric loading conditions. In the damage mechanics analyses, the time to failure is defined as the creep time when the damage variable, ω, at the integration points of all of the elements on a through-thickness path, equals ω_{MAX}. The failure times corresponding to the centred and the asymmetric (δ=0.3 [mm] and θ=-3°) configurations are t_{f0}=43.41 [h] and t_{fa}=54.60 [h], respectively.

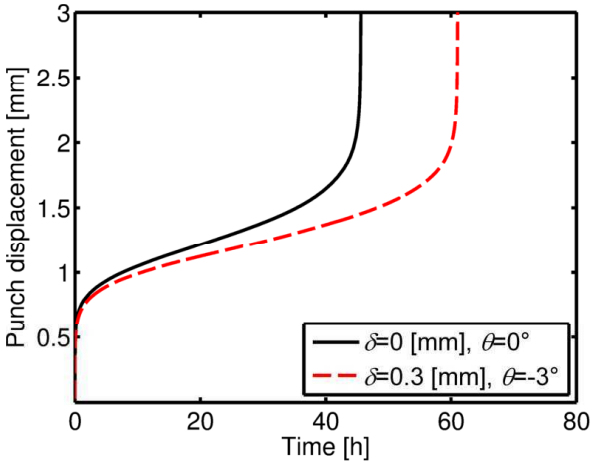

Figure 6.11: Variation of the punch displacement versus time for damage calculations.

When the Liu & Murakami model is used, the ratio between the minimum displacement rates corresponding to the two loading configurations is $(MDR_a/MDR_0|_{LM})$=0.718. This value is slightly higher than the corresponding ratio obtained by using Norton's creep law, i.e. $(MDR_a/MDR_0|_{S-S})$=0.618.

The ratio between the failure times obtained with δ=θ=0 and δ=0.3 [mm], θ=-3° is $(t_{fa}/t_{f0}|_{LM})$=1.258, while, when Norton's law is adopted, the failure time ratio, $t_{fa}/t_{f0}|_{S-S}$, is 1.491. The discrepancy between the values of the (t_{fa}/t_{f0}) ratio, obtained when the two different constitutive models are used, can also be explained by the different definitions of failure time adopted with the two approaches. In the steady-state creep analyses, failure is assumed to occur when specimen's necking (i.e. geometrical softening) does not allow an equilibrium configuration to be computed by the solver, while, when the Liu & Murakami model is used, failure is due to creep material deterioration and damage.

Contour plots of the damage variable, ω, at the failure time, are shown in Figure 6.12 for the two loading configurations investigated, respectively.

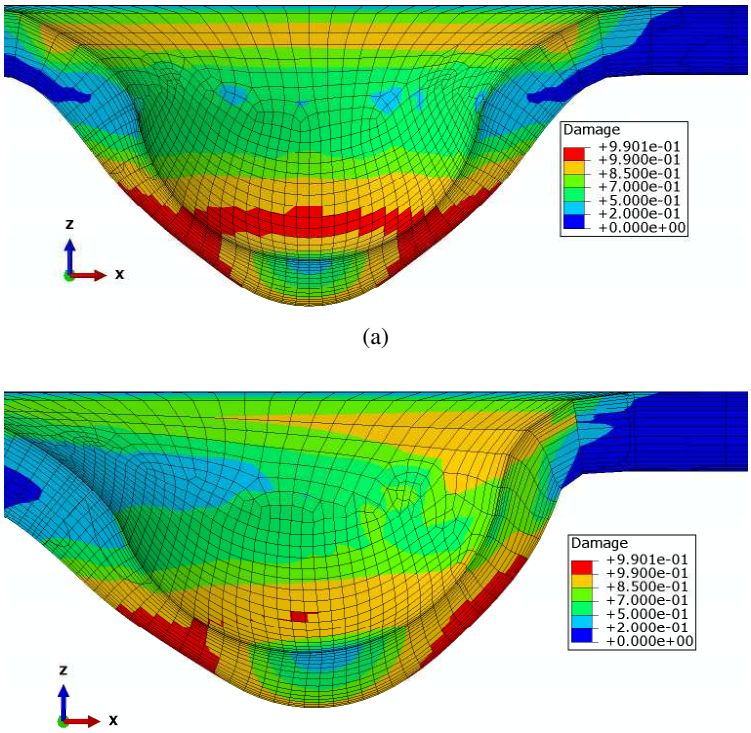

Figure 6.12: Contour plot of the damage variable at failure for (a) δ=θ=0 at t_{f0}=43.41 [h], and (b) δ=0.3 [mm] and θ=-3°, at t_{fa}=54.60 [h].

In both cases, the peak value of damage occurs at the bottom surface of the specimen, at some distance from the geometrical axis of symmetry. The contour plot shown in Figure 6.12 (a) exhibits an axisymmetric damage distribution, while Figure 6.12 (b) reflects the eccentricity and the misalignment of the punch load applied. The peak damage locations shown in Figure 6.12 match the peak stress regions reported in Figures 6.6 (a) and 6.8 (b) for the centred and the asymmetric conditions, respectively. Also, the damage field of Figure 6.12 agrees well with the location of the circumferential cracks found in the tested specimens and reported in Chapter 4 (see Figure 4.7).

Norton's law and the Liu & Murakami constitutive model lead to comparable effects of δ and θ on the minimum displacement rate. This suggests that the creep constitutive model adopted for the numerical analyses does not drastically influence the relative be-

haviour of the specimen for various δ and θ values in terms of *MDR*, while more significant discrepancies were found for the failure time.

Figure 6.13 shows the error bars, obtained by the continuum damage investigations presented in this Chapter, applied to the MDR and the time to failure obtained by the numerical analyses discussed in Chapter 5, which include the effects of pre-straining on the response of the SPCT specimen.

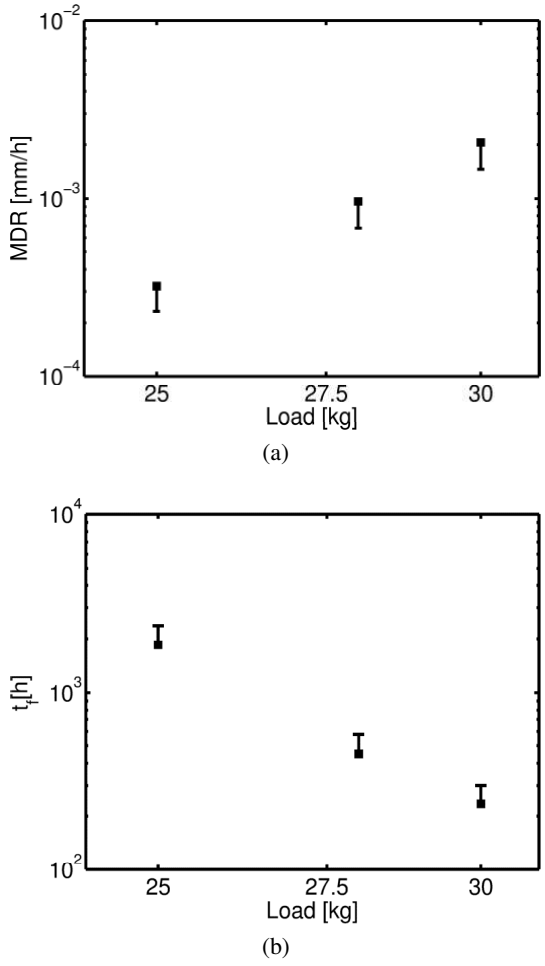

Figure 6.13: Error bars, obtained by the present study, applied to the MDR (a) and to the time to failure (b) obtained by the pre-strain FE calculations discussed in Chapter 5.

6.4 Conclusions

The main aim of this Chapter was to investigate the effects of geometrical inaccuracies on the output of a SPCT, by use of FE modelling. Various steady-state creep FE analyses have

been carried out with different loading configurations, taking into account the initial position of the punch, by the δ parameter, and the direction of the punch load, by the θ parameter. Both δ and θ are shown to have an effect on the SPCT output. When δ and $|\theta|$ increase, the minimum displacement rate, *MDR*, decreases, while the failure time, t_f, increases.

For -2° $\leq \theta \leq$ 0° and $\delta \leq$ 0.2 [mm], the variations of *MDR* and t_f are less than 10%, while, for θ=-3° and δ=0.3 [mm] they are found to significantly increase. The calculations also showed that the effects of θ are not large when $\delta \leq$ 0.2 [mm], and become more remarkable when δ=0.3 [mm]. The effects of δ are significant for the whole range of θ-values investigated.

The influence of δ and θ on the response of the specimen correlates with the variation of its stiffness at different points and along various directions, and to the size of the region governing creep membrane stretching during the test.

In order to evaluate the accuracy of Norton's creep law in the FE calculations, additional FE analyses were carried out by using the Liu & Murakami creep damage model. The results of damage calculations show that the effects of δ and θ on *MDR* are comparable to those obtained by using the steady-state creep assumption. More significant differences were found when the effects of these two parameters on the failure behaviour of the specimen were investigated. This is because different definitions of failure time were adopted for the calculations with Norton's creep law and the Liu & Murakami constitutive model.

The results reported in the present Chapter are useful for the interpretation of practical tests, as significant experimental scatter can be found in the output of SPCTs, as indicated in Chapter 3. However, the real magnitudes of δ and θ during SPCTs are usually unknown.

CHAPTER 7

EFFECTS OF FRICTION MODELLING ON THE SPCT OUTPUT

7.1 Introduction-friction modelling overview

A critical aspect of the analysis of SPCT behaviour is the friction interaction between the punch and the specimen. As mentioned in Chapter 2, this has been investigated by Dymacek et al. who showed that the chosen friction coefficient is a key factor in SPCT finite element modelling [24, 25]. However, in all of the FE models of SPCT reported in the open literature, the "classical" Coulomb's friction model was used. Typical values of μ assumed, for the high temperature, in the range between 0.1 and 0.5.

The "classical" Coulomb friction theory has significant limitations, and its application is bound to induce some degree of inaccuracy in the results obtained using SPCT finite element models.

Several researchers have shown that the interaction of two contacting rough surfaces cannot be described as an intrinsic property of the interface, as assumed in the Coulomb's model [2, 18, 61, 62]. Tabor pointed out that the friction conditions between two rough contacting bodies depends on the real area of contact and the size of the asperities (related to the local stress conditions), the nature and the strength of the bond generated at the

interface (related to the characteristics of the contacting surfaces) and the deformation and rupture modes of the material in the region in the vicinity of the contact, which is related to the local material properties [2, 62, 99, 100, 112].

Leu modified the Tabor friction model and proposed a dry friction formulation for metal forming based on a 3D stress element under a contaminant film, taking into account the real contact area, the surface roughness, the contact conditions and the contact pressure [65]. The condition under which global sliding occurs between the contacting surfaces was described as being similar to the von-Mises failure criterion.

Chang et al. developed a multi-asperities static friction model (hereafter, referred to as the CEB model) [14] for metallic rough surfaces. Spherical contacting asperities were assumed to have the same radii and randomly distributed heights (a Gaussian probability density function was used). The interface was assumed to be capable of transmitting tangential load until yield occurs in a single asperity (yielding inception), leading to global sliding (sliding inception). Kogut and Etsion [61, 62] pointed out that tangential load can also be transmitted after the inception of the yielding of the asperities, since a yielded asperity is surrounded by asperities which are subjected to elastic deformation and can still carry tangential load. In view of this, they introduced an improved multi-asperities static friction model (hereafter, referred to as the KE model) [62] for elastic-plastic contact of rough surfaces, by using finite element analysis results, and showed that the CEB model underestimates the friction coefficient. Both the CEB and KE models are multi-asperities models, and are based on different assumptions from those of Leu's formulation, i.e. the loss of tangential load carrying capability due to plastic yield of asperities.

Accurate contact modelling is of vital importance for any friction model [2]. When the "first body" approach is used, i.e. when the interacting bodies are of primary interest and are modelled without a detailed description of the interacting surfaces considered as separate bodies, finite element analysis is a useful tool for improving the understanding of the contact problem between two rough surfaces [89].

In view of the limitations of the Coulomb theory and the effects of the friction co-

efficient on the results of SPCT finite element analyses [25], more accurate procedures for friction modelling are needed for application in SPCT numerical analyses.

7.2 Leu's Friction model

In the classical Coulomb's friction model, used in all of the finite element models reported in the open literature for the small punch creep test (see Chapter 2), the interacting bodies are assumed to be in sticking conditions until the ratio of the transmitted shear stress to contact pressure equals the friction coefficient, μ, and the inception of global sliding occurs. The friction coefficient is often assumed to be constant over the interface between the contacting bodies and it is taken to be an intrinsic characteristic of the interacting surfaces.

An explanation of the friction interaction between two contacting surfaces was proposed by Bowden and Tabor [9]. They argue that, when two surfaces are in contact under normal load, the pressure at the tips of contacting asperities is, generally, high enough for plastic flow to take place. The friction between two interacting surfaces can be related to the adhesion of strong junctions which are generated at the points of real contact and must be sheared for sliding to occur [99]. The frictional force (i.e. the force needed to produce surface sliding) can be decomposed into two contributions, i.e. the shear and the ploughing components. For metal surfaces, the ploughing component is generally smaller than that related to shear and, hereafter, it will be neglected [99, 102].

Tabor pointed out that relative sliding of two contacting surfaces is related to the combination of normal and frictional stresses and, for a 2D stress element, it takes place when equation (7.1) is satisfied, where p represents the contact pressure, τ_f is the frictional stress (tangential stress at the interface due to interaction under incipient sliding conditions) and K_f is the shear strength of the softer material [65, 99].

$$p^2 + 3\tau_f^2 = 3K_f^2 \tag{7.1}$$

Equation (7.1) represents the condition of the sliding inception and does not represent the condition for an asperity to yield, as the term on the right side, K_f, is not the von Mises equivalent yield stress.

The relation between the frictional stress, τ_f, and the shear strength, K_f, is given by equation (7.2), where $\alpha_c = \Omega_R/\Omega_A$, ranges from 0 to 1, and is the ratio between the real and the apparent contact areas, Ω_R and Ω_A, respectively [65]. The condition α_c=0 represents the "free contact state", where the real contact area is zero and, as a consequence, no frictional force is transferred between the contacting bodies and therefore τ_f=0, while the condition α_c=1 represents the "fully contact state", i.e. the real and apparent contact areas are equal, and the frictional stress needed for sliding to occur is maximum.

$$\tau_f = \alpha_c K_f \tag{7.2}$$

The real contact area between two interacting surfaces is influenced by the deformation mode of the contacting asperities (hence the loading conditions and the material properties of the interacting bodies) and the surfaces topography (i.e. the surfaces roughness) [100]. However, in many practical applications for metals, plastic deformation of asperities occurs even when the contact pressure, *p*, is an order of magnitude less than the yielding pressure, p_0, of the material [100].

In ref. [65], Leu reported a hyperbolic tangent function to relate α_c to *p*, given by equation (7.3), where C_a is a factor used to control the value of the hyperbolic function (assumed to be equal to 3 in ref. [65]) and σ_u is the ultimate stress of the softer material.

$$\alpha_c = \tanh\left(C_a \frac{p}{\sigma_u}\right) \tag{7.3}$$

The C_a parameter can include the effects of eventual contaminant layers that may be present between the two contacting bodies (which can change the material plasticity

properties of the underlying metal [100]) and of the local distribution of dislocations in the metal on the real contact area ratio, α_c [65]. It needs to be accurately evaluated.

When the contact pressure increases, more asperities come into contact, and the real contact area ratio increases. Figure 7.1 shows the variation of α_c with contact pressure for a material with a nominal ultimate strength of 310 [MPa], and several values of C_a.

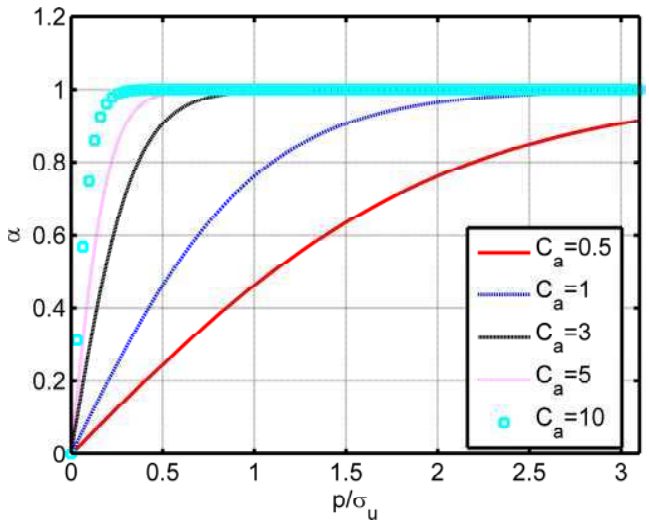

Figure 7.1: Variation of α_c with contact pressure, obtained by using equation (7.3) for a material with σ_u=310 [MPa] and different values for C_a.

In ref. [65], Leu reported an expression for the friction coefficient, μ, given in equation (7.4), obtained by using Tabor's theory. It is valid for constant friction coefficient conditions but it can be localised when the contact interface is divided into several sub-regions each one characterised by a contact pressure value.

$$\mu = \frac{F_f}{N} = \frac{\tau_f}{p} = \frac{\alpha_c}{\sqrt{3\left(1-\alpha_c^2\right)}} \tag{7.4}$$

Equation (7.4) shows the dependency of μ on the real contact area, hence on local loading conditions and plastic material properties and surface topography, by the C_a coefficient. Leu pointed out that, in "fully contact" conditions (α_c=1), the friction coefficient defined by equation (7.4) approaches infinity. This unbounded behaviour contradicts experimental evidence and, for contacting metals, the friction coefficient should be less than

0.577, if equation (7.1) is valid [65]. Furthermore, Tabor pointed out that the friction coefficient reaches values close to unity when the contacting surfaces are not placed in a vacuum and a contaminant layer is found between the contacting surfaces [99].

In order to overcome this contradiction, Leu proposed a formulation based on a 3D material element, leading to the sliding condition given in equation (7.5), where p_x=p_y=p_l is the lateral pressure acting on the material element [65].

$$(p - p_l)^2 + 3\tau_f^2 = 3K_f^2 \tag{7.5}$$

Based on equation (7.5), a modified expression for the friction coefficient was obtained by Leu [65], given in equation (7.6).

$$\mu = \frac{\alpha_c}{\sqrt{3\left(1 - \alpha_c^2\right)} + \frac{\sigma}{K_f}} \tag{7.6}$$

For a material with a power law strain hardening behaviour given by equation (7.7) in uniaxial form, where σ is the stress, ε_p is the effective strain for plastic deformation and A_p and n_p are material constants, Leu obtained a relation between μ, the real contact area ratio, α_c, and the strain hardening exponent, n_p represented by equation (7.8) [65, 88].

$$\sigma = A_p \varepsilon_p^{n_p} \tag{7.7}$$

$$\mu = \frac{\alpha_c}{\sqrt{3}\left[\left(1 - \alpha_c^2\right)^{0.5} + \alpha_c^{n_p/2}\right]} \tag{7.8}$$

Figure 7.2 is a plot of the variation of friction coefficient with contact pressure obtained by using equations (7.8) and (7.3), for a metallic material, with strain hardening exponent $n_p = 8.693 \times 10^{-2}$ and σ_u=310 [MPa], for various values of C_a.

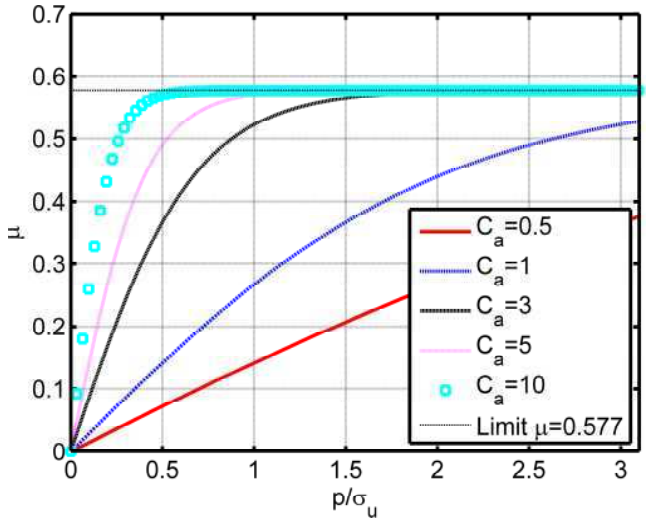

Figure 7.2: Variation of the friction coefficient with contact pressure for material with σ_u=310 [MPa], $n_p = 8.693 \times 10^{-2}$ for different values for C_a.

When the real contact area ratio approaches unity, the friction coefficient, plotted in Figure 7.2, approaches the limiting value μ_{LIM}=0.577. When the contact pressure increases, also α_c increases (see Figure 7.1), as well as the number of contacting asperities, leading to an increase of friction coefficient. The limit represented by μ_{LIM} is in agreement with practical evidence [65, 99] and has been adopted in the FE analyses presented in this Chapter. The increase of the friction coefficient with the normal load for dry contact has been related also by Hwang and Gahr to the increase of the real contact area and of the number of contacting asperities [40].

7.3 Numerical modelling of Small Punch Creep Test

7.3.1 Material constitutive model(s) used for the analyses

Elastic/plastic/creep analyses have been carried out with the time independent material behaviour being modelled as linear elastic/exponential plastic with isotropic hardening, based on equation (7.7) [65].

The creep behaviour of the material has been modelled by using the well-known Norton law (secondary creep approximation), represented by equation (2.18), Chapter 2

in uniaxial form. The material constants used for the creep and the plasticity models are reported in Table 7.1.

Table 7.1: Material constants used for the elastic/creep analyses, with stress expressed in [MPa] and time in [h].

E_0 [MPa]	ν	B	n	A_p	n_p	σ_y
1.492×10^5	0.3	9.795×10^{-32}	12.342	455.4	8.693×10^{-2}	280

7.3.2 Geometry, loads and boundary conditions

Similarly to the analyses discussed in Chapter 5, a 2D axis symmetric FE model has been adopted for the calculations because of the symmetry of the problem. The specimen has been modelled as a deformable part, while the punch, the support and the upper clamp have been modelled as rigid bodies.

The geometry of the FE model, represented in Figure 7.3, has the same dimensions as that used in Chapter 6 (in the symmetric loading configuration), i.e. the punch radius is R_s=1.25 [mm], the receiving hole radius is a_p=2 [mm], the thickness of the specimen is t_h=0.5 [mm] and the diameter of the specimen is D_{SPT}=8 [mm].

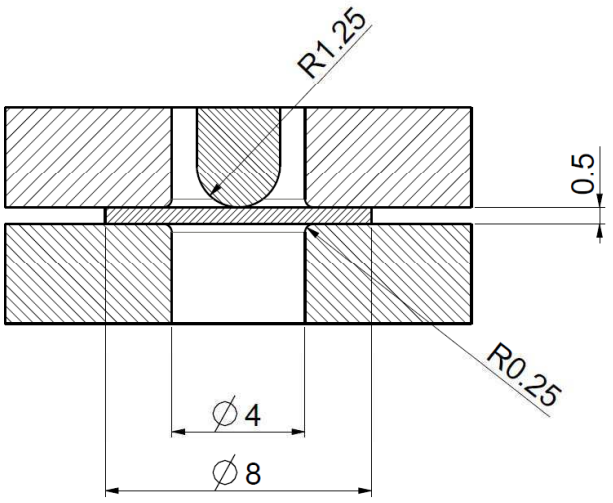

Figure 7.3: Geometry used for the FE analyses with dimensions in [mm].

Various load levels, ranging between 34 and 42 [kg], have been applied to the punch in the analyses and appropriate boundary conditions have been imposed to the rigid bodies to model the test rig.

As for the model of Chapter 5, the radial and axial translations and the rotation of the support have been constrained. The horizontal translation and the rotation of the punch and of the upper clamp have also been blocked.

The clamping load has been applied by imposing a vertical displacement of 3.419×10^{-6} [mm] to the upper clamp. Figure 7.4 schematically shows the loads and the boundary conditions applied to the FE model.

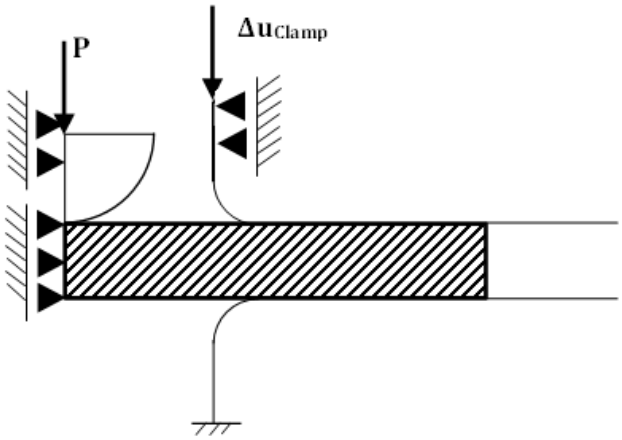

Figure 7.4: Loads and boundary conditions applied to the FE model of SPCT.

7.3.3 Meshing and element choice

The FE mesh adopted in the analyses has been developed taking into account the different stress and strain fields in various regions of the specimen and at various stages of the specimen deformation. A mesh sensitivity analysis was conducted in order to minimise numerically induced fluctuations of the contact pressure in the creep solution over the expected contact area between the punch and the specimen; this has led to an "optimised" element size equal to 0.0024 times the punch radius. As discussed in Chapter 2, accurate modelling of the region close to the edge of contact between the specimen and the punch is of critical importance in predicting SPCT behaviour [76], as well as that close to the clamps, where initial bending deformation occurs. These two regions in the specimen have relatively small element sizes, while a coarser mesh has been adopted for the other regions.

Figure 7.5 is a swept representation of the mesh used for the FE analyses. It consists

of 15,253 nodes and 14,892 quadrilateral, 2D axisymmetric, linear elements. The hybrid elements formulation has been adopted, in order to avoid the numerical difficulties which are generated when incompressible deformations occur, as for the analyses of Chapters 5 and 6. A reduced integration scheme was used in order to overcome problems related to locking of elements. As for the calculations of Chapter 5, the CAX4HR element type, available in ABAQUS, was used.

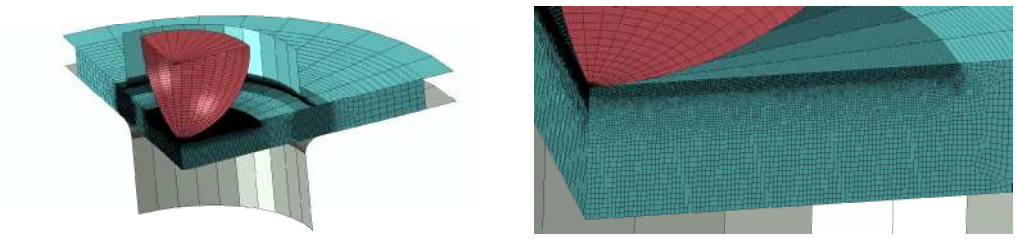

(a) (b)

Figure 7.5: (a) Swept representation of the 2D axisymmetric mesh adopted in the FE analyses and (b) detailed view of the mesh in the unsupported region of the specimen.

7.3.4 Modelling of the variable coefficient of friction

The friction interaction for the contact between the punch and the specimen has been assumed to vary with local loading conditions, according to Leu's model, equation (7.8). A FRIC_COEF user subroutine has been implemented in order to include this friction formulation into the numerical solver. The subroutine is called at each contact point and can calculate the value of μ as a continuous function of contact pressure. The FRIC_COEF subroutine has also the capability to describe the variation of the friction coefficient with the temperature and the sliding rate. In the present investigation, the temperature is assumed to be constant and the sliding rate is low, thus only the dependency of μ on the contact pressure (see equation (7.8)) has been modelled, i.e. it neglects the dependency on temperature and sliding rate.

In order for the calculation to be performed, also the derivatives of μ with respect to these three quantities (i.e. contact pressure, sliding rate and temperature) need to be input into the subroutine. The effects of eventual field variables, defined by the user, could also be taken into account.

In the present calculations, the friction coefficient between the clamps and the specimen has been assumed to be constant, because only the effects of the friction formulation between the punch and the specimen are investigated. The upper bound of equation (7.8), i.e. a constant coefficient of friction of μ_{LIM}=0.577, is used for the coefficient of friction between the specimen and the dies.

7.4 Numerical results and discussion

Several elastic/plastic/creep analyses have been carried out using the FE model described in Section 7.3, using both variable friction formulation (equation (7.8)) and classical Coulomb's theory, with μ ranging between 0.1 and 0.5, for the punch/specimen interaction. As mentioned in Section 7.3.4, the contact between the specimen and the clamps is assumed to exhibit a constant coefficient of friction, equal to μ_{LIM}, in all of the FE analyses discussed in this Chapter.

At the beginning of the creep step (elastic/plastic FE solution), the elastic and plastic deformations, occurring under the contact surface, affect the local loading conditions (i.e. the variation of contact pressure with radial position) in the contact area. These local conditions govern the value of the coefficient of friction (see equations (7.3) and (7.8)) and, in turn, the stress and strain fields resulting in the specimen.

Figure 7.6 shows contour plots of the von Mises equivalent plastic strains at the beginning of the creep step for three different load cases, with punch loads ranging from 34 to 42 [kg]. In the region close to the interface between the punch and the specimen, the plastic strains are predicted to be larger than 10% for all of the load levels, hence the effect of plasticity on the variation of the contact pressure is significant.

The maximum von-Mises equivalent plastic strain is located at the bottom surface of the specimen in an annular region approximately 0.5 [mm] away from the symmetry axis, similar to the critical region identified by Dymacek et al. for SPCT specimen [24]. In view of its magnitude, the plastic flow in the critical region of the specimen is not negligible for

all of loads used in the analyses. From Figure 7.6, it can be observed that plastic deformation influences the response of the specimen for all of the load levels, hence it is important to take it into account.

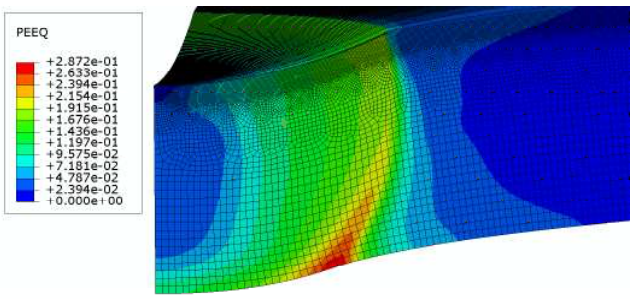

(a)

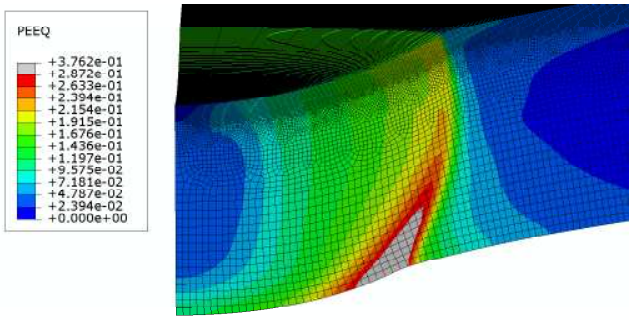

(b)

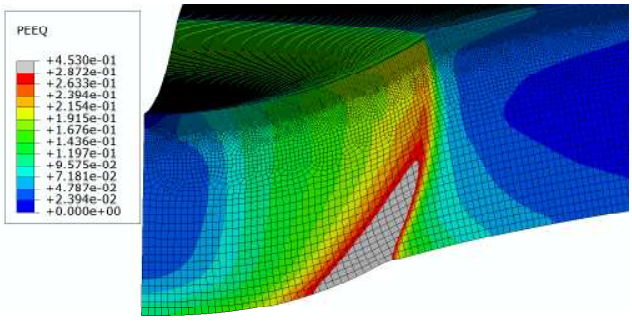

(c)

Figure 7.6: Swept view of the 2D contour plot of the von-Mises equivalent plastic strain, expressed in absolute value, at the beginning of the creep step with load levels of (a) 34, (b) 38 and (c) 42 [kg].

Figure 7.7 shows the contour plots of the von-Mises equivalent stress at the beginning of the creep step with the load ranging between 34 and 42 [kg].

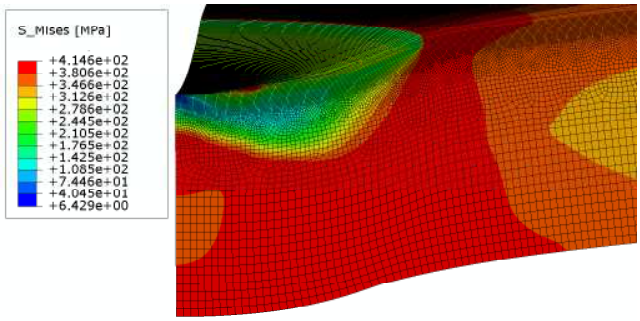

(a)

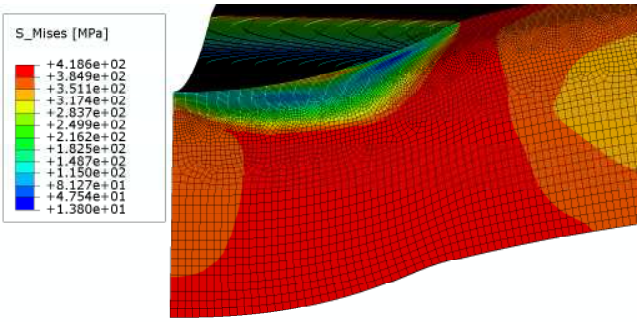

(b)

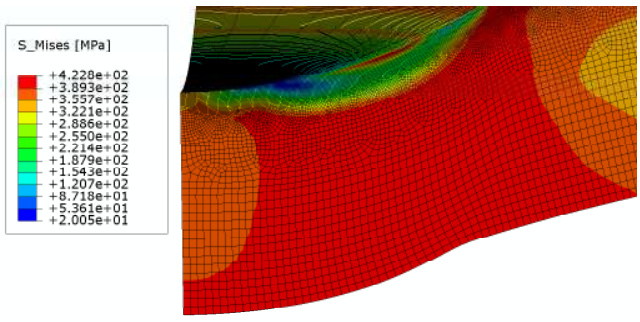

(c)

Figure 7.7: Swept view of the 2D contour plot of the von-Mises equivalent stress, expressed in [MPa], at the beginning of the creep step with load levels of (a) 34, (b) 38 and (c) 42 [kg].

During the small punch creep test, the specimen undergoes large global deformation which, indirectly, affects the local contact loading conditions, i.e. the variation of the local contact pressure, p, with radial position and time. An increase of p on an element of the contact surface brings more asperities into dry contact, thus the friction coefficient, μ, increases on that element and, hence, more tangential load can be carried before global sliding occurs [40].

Figure 7.8 shows the plots of the punch displacement versus creep time for the three load levels (34, 38 and 42 [kg]) used in the numerical analyses. The cases include both variable and constant friction coefficient conditions. C_a=3 has been used in the cases with variable friction coefficient (see equation (7.3)) for consistency with ref. [65].

From Figure 7.8, the effect of the coefficient of friction formulation on the results of SPCT FE analyses can be observed and, for the test cases with constant μ, agreement with the results reported in ref. [25] is found. For a given load level, when the coefficient of friction increases, the minimum displacement rate decreases and the failure time increases. In this Chapter, as Norton's law was used, the failure time has been defined as the creep step time when the solution did not converge.

The influence of μ on SPCT output can be explained by considering the effect of the distributed forces, generated by friction, on the stress field of the specimen. Friction forces induce a local stress field that opposes the relative global motion (sliding) of the interacting bodies (in this case, the specimen and the punch). Consequently, a bending moment, which contrasts the global deformation of the specimen, is generated in the sample because of the equilibrium of the region of the specimen in the vicinity of the contact area.

For a given punch load level, when the friction coefficient increases, the magnitude of the friction forces increases as well. In turn, the magnitude of the bending moment contrasting the global deformation of the specimen increases. This causes a decrease in the minimum displacement rate and an increase in the failure time.

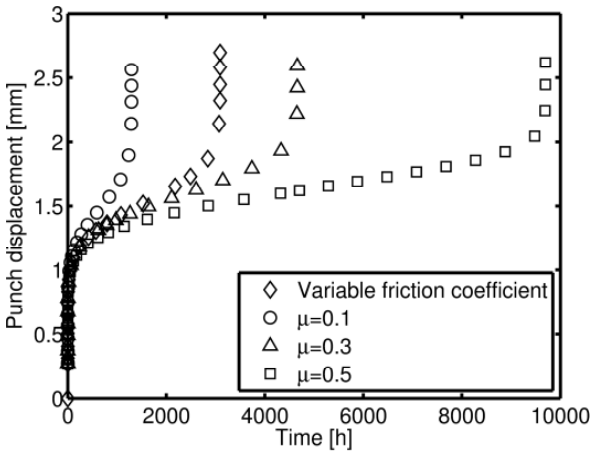

(a)

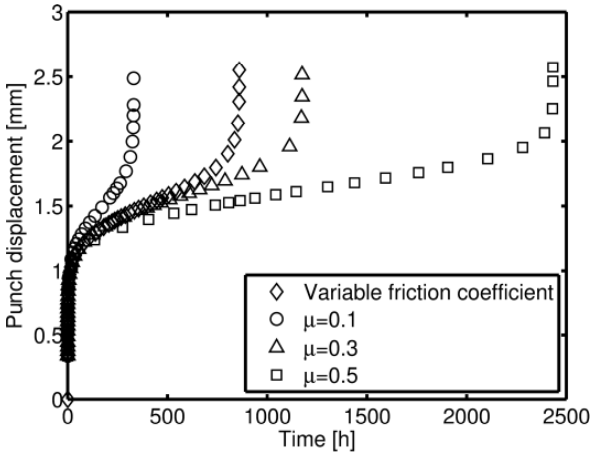

(b)

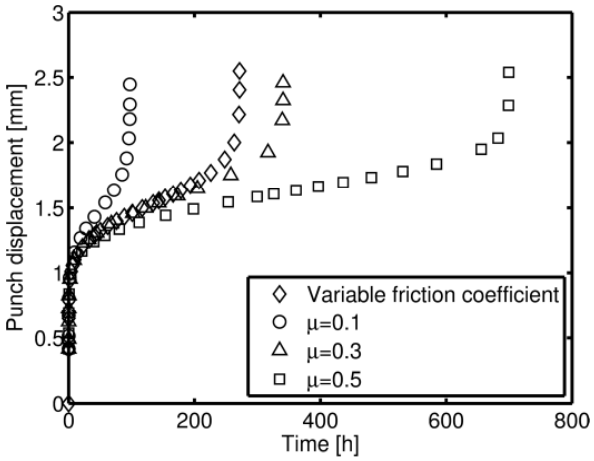

(c)

Figure 7.8: Plot of the punch displacement versus time for a load of (a) 34, (b) 38 and (c) 42 [kg]. C_a=3 for the variable friction coefficient test cases.

In order to evaluate the effects of the C_a parameter (see equation (7.3)) on the numerical results, FE analyses have been performed using the variable friction formulation, equation (7.8), with C_a ranging from 1 to 20. The results of the analyses (i.e. the variation of the punch displacement with time) are shown in Figure 7.9 for a load of 38 [kg].

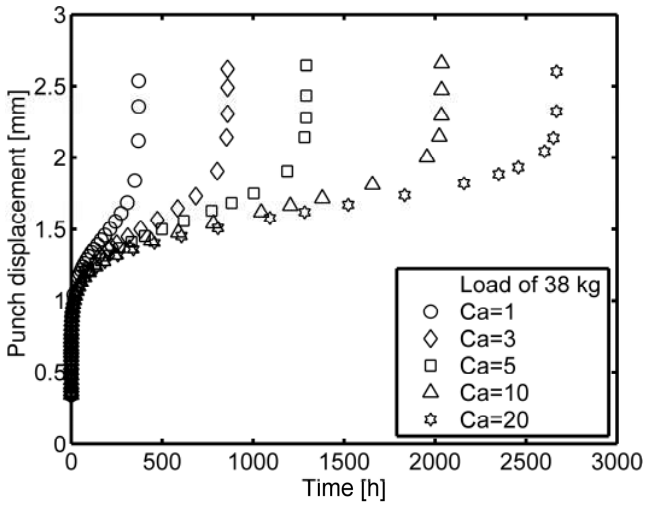

Figure 7.9: Plot of the punch displacement versus time for a load of 38 [kg] and different values of C_a.

The minimum displacement rate and the failure time were found to be sensitive to the C_a parameter, especially in the range between C_a=1 and C_a=10. When C_a increases, the failure time increases and the minimum displacement rate decreases. This behaviour is due to the effect of C_a on the real contact area ratio, α_c, (equation (7.3)), and, in turn, on the coefficient of friction (equation (7.8)). In view of the results shown in Figure 7.9, an accurate estimation of C_a, taking into account the surface roughness and the material properties of the specimen, is needed in order to obtain accurate estimations of μ [65].

The variation of the coefficient of friction on the contact surface, over the creep step, has been evaluated from the FE results performed by using Leu's friction formulation (equation (7.8)). Figure 7.10 is a plot of the coefficient of friction over a quarter of the contact region for a punch load of 34 [kg] at different creep times, while Figure 7.11 shows the variation of the friction coefficient with creep step time and the radial coordinate normalised with respect to the current contact edge radius, r_{cont}, for C_a=3.

The coefficient of friction was found to vary significantly over the area of contact and, during most of the creep step, its maximum value has been found to occur at the contact edge (see Figures 7.10 and 7.11). This variation is related to the mode of deformation of the specimen, which is characterised by the effects of material non-linearities (such as plasticity and creep), varying geometrical stiffness of the specimen (effects of large deformations and necking), and the severe loading conditions (peak contact pressure) which occur at the contact edge.

During creep deformation, at the centre of the specimen, a minimum cusp point can be observed in the distribution of μ (see Figures 7.10 and 7.11). This can be related to the global response of the small disc specimen, caused by the axisymmetric geometry and the plastic/creep material constitutive model.

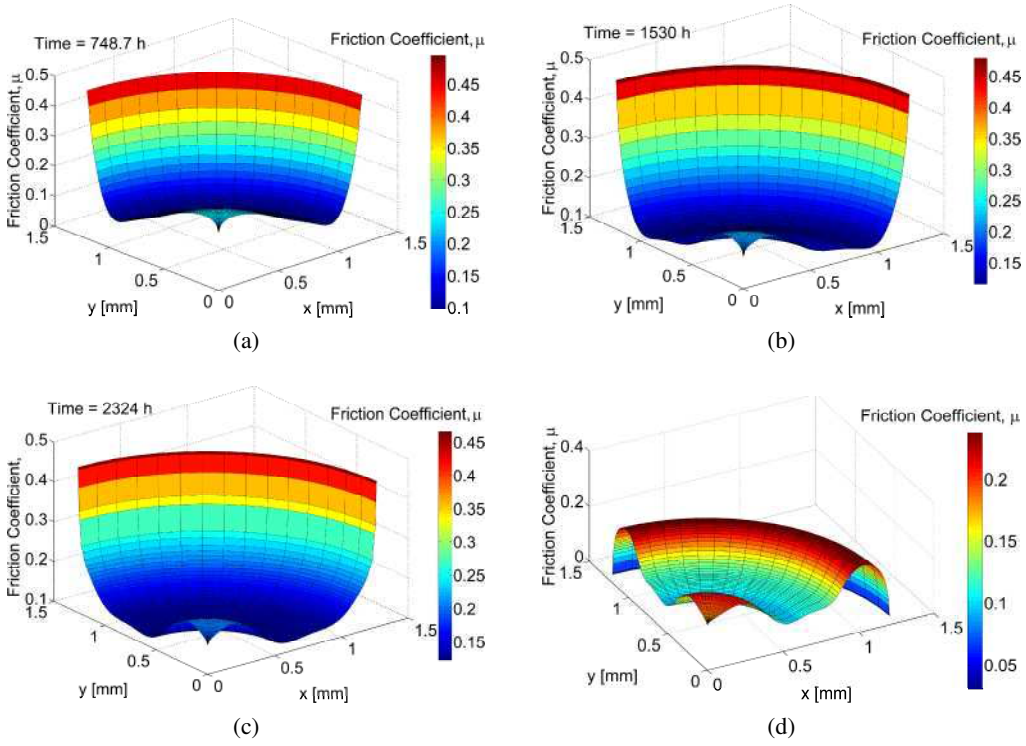

Figure 7.10: Swept plot of the distribution of the coefficient of friction, μ, at creep step time fractions of (a) t=0.25 t_f, (b) t=0.5 t_f, (c) t=0.75 t_f, (d) t=0.99 t_f, for a load level of 34 [kg], over a quarter of the contact surface.

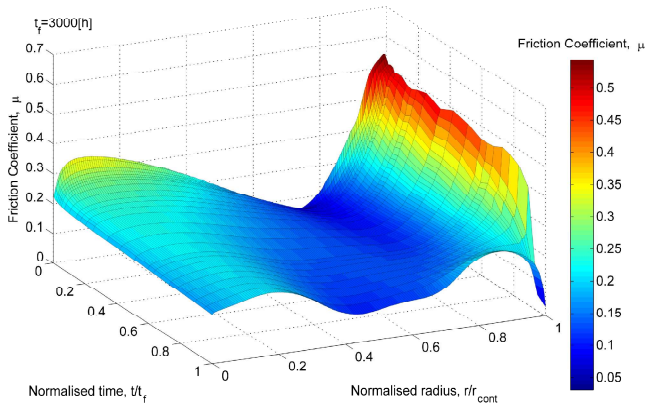

(a)

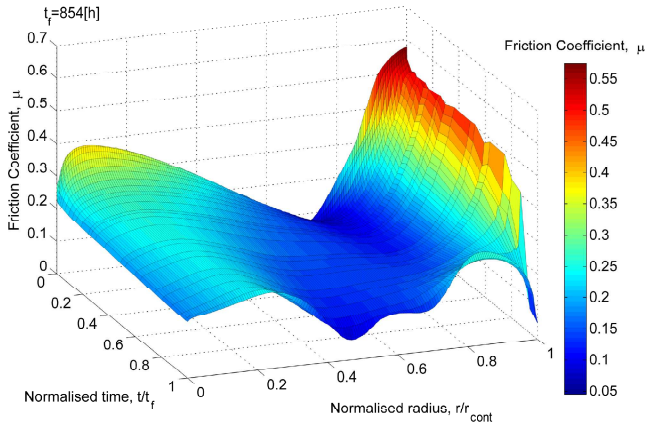

(b)

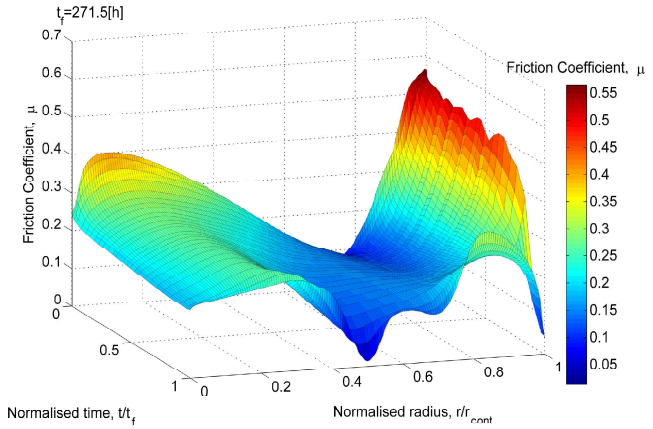

(c)

Figure 7.11: Variation of the coefficient of friction with normalised radius, r/r_{CONT} and creep step time for load levels of (a) 34, (b) 38 and (c) 42 [kg].

As creep proceeds in the specimen, the loading mode progressively changes from bending dominant to "membrane stretching" dominant and the stress field redistributes within the specimen. The effects of the transition are visible also in Figures 7.10 and 7.11. Furthermore, the average magnitude of μ decreases with time, since the apparent contact area progressively increases under a constant punch load.

The stress redistribution, occurring during the test and related to creep deformation, modifies the shape of μ=$\mu(r)$ (see Figure 7.10). After a creep step time of approximately 0.5 t_f, the friction coefficient remains almost constant at its minimum value in the annular region between 0.4 r_{cont} and 0.7 r_{cont}, where r_{cont} is the radial position of the contact edge. This region expands when the creep step proceeds. The distribution of the coefficient of friction is then drastically modified when the failure time is approached and the maximum value of μ is at the radial position $r/r_{cont} \approxeq 0.9$ (see Figures 7.10 and 7.11).

The punch load does not affect the variation of μ=$\mu(r)$ to a large extent during creep analyses, as the governing deformation modes are the same for all three load levels adopted.

In Figure 7.8, the displacement curves obtained from the cases with the variable friction formulation were found to be similar to those calculated by using a constant "equivalent" coefficient of friction. In order to investigate the possibility to identify an "equivalent friction coefficient", some additional FE analyses were performed using Coulomb's theory, with a coefficient of friction of 0.22 (for a load of 34 [kg]), 0.24 (for a load of 38 [kg]) and 0.26 (for a load of 42 [kg]). The values of minimum displacement rate and failure time obtained by these three analyses were similar to those obtained by using the variable friction formulation of equation (7.8) with the respective loads. This shows that a load-independent value of the coefficient of friction, capable of including the effects of the contact pressure on FE results, cannot be identified, as different load levels led to different values of the "equivalent friction coefficient", which was found to increase with the load.

In the regions of the specimen far from the interface with the punch, use of constant "equivalent" values of the coefficient of friction lead to stress and strain distributions similar to those obtained from the variable friction cases. However, in the vicinity of the

punch/specimen interface, the stress and strain fields differ.

Furthermore, the "equivalent" friction coefficient is not equal to the average value of the coefficient of friction, $\bar{\mu}$, obtained from Leu's formulation. The average values range from 0.19 to 0.21 for the three load levels used (see Figure 7.10). This discrepancy between the average and the "equivalent" values is related to the highly non-linear response of the specimen. It suggests that different regions of the punch/specimen contact surface have different effects on the stress and strain fields, affecting the bending and membrane stretching response. For example, the peak of the friction coefficient occurs at the contact edge and it shows there to be a higher influence on the test output than other regions of the contact area, as the "equivalent" value of μ is always higher than $\bar{\mu}$.

In the present Chapter, since Norton's creep law (steady-state creep approximation) has been used, material creep damage and deterioration are not taken into account. Therefore, the "tertiary SPCT region", i.e. the region where the punch displacement rate drastically increases (see Figures 7.8 and 7.9), is caused by progressive necking of the critical annular region of the specimen (i.e. geometrical softening, see also refs. [24, 76]), accounted for by the non-linear geometry formulation. This assumption was used because just the relative behaviour of the specimen with different friction formulation was investigated.

Figure 7.12 is an SEM image of the top surface of the specimen of a SPCT interrupted after 669 [h]. Although the load level and the geometry of the experimental apparatus used to test the specimen of Figure 7.12 (reported in Chapter 3) are different from those of the calculations discussed in this Chapter, it is visible that the location of the punch/specimen contact surface where the friction conditions are most severe is the annular region near the contact edge. These findings are in agreement with the friction coefficient maps shown in Figures 7.10 and 7.11 and confirm that the variation of μ obtained by the present calculations is accurate.

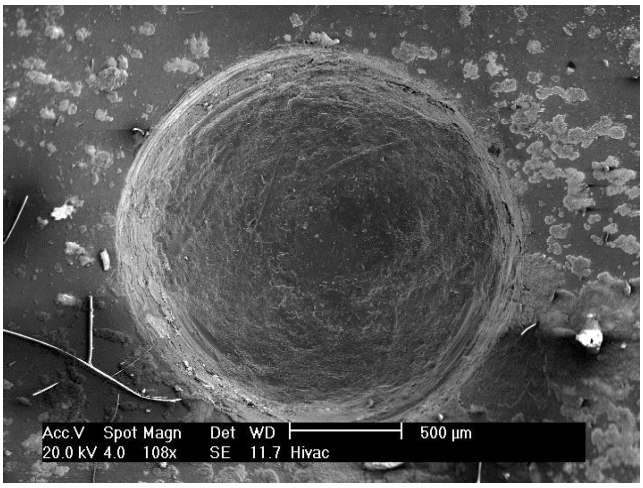

Figure 7.12: SEM image of the top surface of the specimen of an SPCT with a punch load of 25 [kg] interrupted after 669 [h] (see also Chapter 4)

.

7.5 Concluding remarks

Elastic/plastic/creep FE analyses of a small punch creep test specimen were carried out with the aim of investigating the effects of local loading conditions, i.e. contact pressure, on the distribution of the coefficient of friction. A variable friction coefficient formulation, developed for metal forming by Leu [65], linking the real contact area, thus contact pressure, the material properties and contact surfaces characteristics to the coefficient of friction, was adopted to model the tangential behaviour of the specimen/punch interaction.

The results of the analyses showed that the friction coefficient varies over the contact surface during the creep step. The large deformation of the specimen and the plastic and creep material flows govern the local contact loading conditions and, in turn, the variation of the coefficient of friction, which was found to significantly influence the variation of the punch displacement versus time. Although the variation of μ has been identified, an accurate estimation of its value is still not possible because the numerical results are affected by the C_a parameter, which is used to identify the real contact area and is related to material properties and surface characteristics of the specimen. A procedure to accurately identify this parameter is still not available; this would enable an important improvement over present FE models. The friction formulation could be improved by also taking into account the "thermally activated adhesion" and investigating its effects on FE results [93].

At the present, a definitive validation of numerical results is not possible but qualitative agreement was found with the experimental findings on an interrupted test specimen.

CHAPTER 8

NOVEL INTERPRETATION TECHNIQUE

8.1 Introduction

As mentioned in Chapters 1 and 2, one of the main limitations related to the application of the small punch creep testing technique is the absence of an established technique to convert the experimental output into that of corresponding conventional uniaxial creep tests.

The SPCT output, consisting of the variation of the punch displacement and the failure time, does not provide direct information about the creep properties of the tested material. The punch load (which has the dimensions of a force) must be related to a 'representative' stress level, while the punch displacement (having the dimensions of a length) must be converted into the creep strain (dimensionless quantity) of a conventional uniaxial creep test carried out at a stress level equivalent to the stress field acting in the small punch test specimen.

The CEN draft code of practice [1] reports an equation relating the load, applied to the SPCT disc, and the 'equivalent' stress, of a uniaxial creep test which leads to the same failure time as that of the SPCT. This equation is reported in Chapter 2, equation (2.65), for the range of geometries recommended in ref. [1], see also below.

$$\frac{P}{\sigma_{EQ}^{UNI}} = 3.33\ K_{SP}\ a_p^{-0.2} R_s^{1.2} t_h$$

The use of this equation, however, requires the uniaxial data for the tested material to be available in order to identify the K_{SP} parameter which depends on the ductility of the material at the testing temperature. An alternative to equation (2.65) is provided by equation (2.66), relating the punch load, *P*, to the meridional component of the membrane stress for the European Round Robin geometry, i.e. $R_s = 1.25$ [mm], $a_p = 2$ [mm] and $t_h = 0.5$ [mm].

No correlation of the punch displacement, with a creep strain level is reported in the CEN draft code of practice. Li et al. [69] obtained a third-order polynomial correlation, reported in equation (2.62), between the equivalent strain $\varepsilon_{EQ,EDGE}$, calculated at the punch/specimen contact edge, and the punch displacement, h_{punch} for the European Round Robin geometry. This correlation, also shown below, is based on the Chakrabarty theory for membrane stretching over a hemispherical rigid punch, which is discussed in Section 2.6.3 of the literature review (Chapter 2). It was obtained by fitting $\varepsilon_{EQ,EDGE}$ with h_{punch} for different values of the contact angle, $\theta_{Ch,0}$, in equations (2.56), (2.57) and (2.58), which are also shown below.

$$\varepsilon_{EQ,EDGE} = 2\ln\left[\frac{1+\cos\theta_{Ch}}{1+\cos\theta_{Ch,0}}\right]$$

$$sin\theta_{Ch} = \frac{R}{a}\sin^2\theta_{Ch,0}$$

$$h_{punch} = a_p \sin\theta_{Ch}\ln\left[\frac{\tan\left(\frac{\theta_{0,Ch}}{2}\right)}{\tan\frac{\theta_{Ch}}{2}}\right] + R_s\left(1-\cos\theta_{0,Ch}\right)$$

$$\varepsilon_{EQ,EDGE} = 0.17959h_{punch} + 0.09357h_{punch}^2 + 0.0044h_{punch}^3$$

The conversion techniques reported in the open literature, however, do not take into account the effects of the large initial plastic deformations on the following creep behaviour of the specimen which, in view of the findings reported in Chapters 3 and 5, have remarkable effects on the SPCT output. Also, the distribution of plastic deformation in the specimen is not uniform (see Chapter 5, Figure 5.7), therefore, the effects it has on the creep response of the specimen are not homogeneous, as Figures 5.8 and 5.9 show.

In this Chapter, a procedure to convert the displacement rates of a SPCT into the creep strain rate of a corresponding uniaxial creep test, and the punch load to a stress level representative of the behaviour of the SPCT is presented. This technique, which is capable of accounting for the effects of initial plastic deformation and the actual stress field acting in the specimen, was obtained by using the results of the numerical calculations discussed in Chapter 5 and it was adopted to convert the SPCT data reported in Chapter 3.

8.2 Conversion methodology

8.2.1 Conversion of the punch displacement rate to strain rate

The procedure developed to correlate the punch displacement, h_{punch}, to the equivalent creep strain was obtained by using the well established Chakrabarty theory, which is the most relevant analytical model for SPCT. Similarly to the fitting of equation (2.62), this technique is valid when the punch displacement is larger than 20% of the receiving hole diameter, which is the largest structural dimension of the test rig, i.e. $h_{punch} > 0.8$ [mm] for the geometry used in the present work.

By using a procedure similar to that adopted by Li and Sturm [69] and by Yang and Wang [109], equations (2.57), (2.58) and (2.56), also reported in Section 8.1, were used to fit a third order polynomial function of the form of equation (8.1) to the variation of the equivalent strain at the contact edge, $\varepsilon_{EQ,EDGE}$, versus the punch displacement, h_{punch}, for the experimental set-up used for the SPCTs reported in Chapter 3, i.e. $R_S = 1.04$ [mm] and $a_p = 2$ [mm]. Table 8.1 lists the fitting constants for equation (8.1), with the test set-up geometry used in Chapter3. Figure 8.1 shows the variation of $\varepsilon_{EQ,EDGE}$ versus h_{punch} together with the plot of equation (8.1) (with the coefficients of Table 8.1).

$$\varepsilon_{EQ,EDGE} = p_1 h_{punch}^3 + p_2 h_{punch}^2 + p_3 h_{punch} + p_4 \tag{8.1}$$

Table 8.1: Fitting constants for equation (8.1).

p_1	p_2	p_3	p_4
6.224×10^{-3}	0.1186	0.2202	7.873×10^{-3}

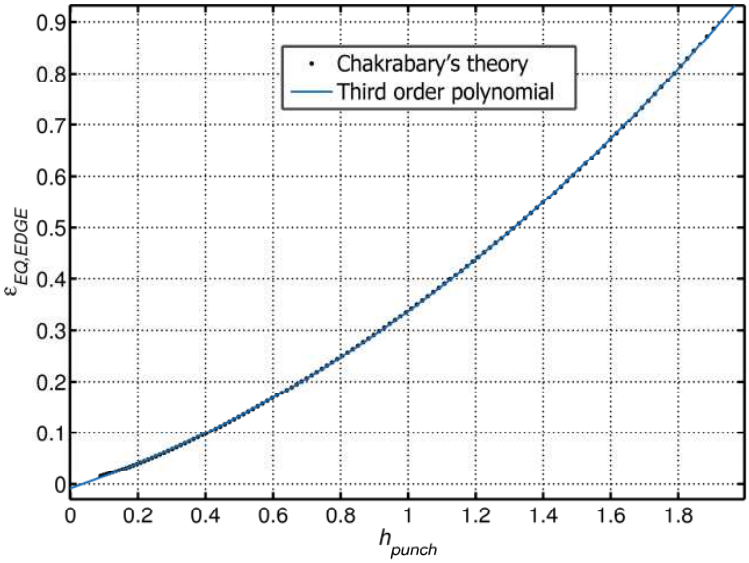

Figure 8.1: Variation of $\varepsilon_{EQ,EDGE}$ versus h_{punch} obtained by equations (2.56)-(2.58), with the plot of equation (8.1).

Along with a component generated by creep deformation, $\varepsilon_{EQ,EDGE}$ also includes the initial deformation taking place in the specimen when the punch load is applied. The strain due to the initial deformation, $\varepsilon^{in}_{EQ,EDGE}$, must be therefore subtracted from the total equivalent strain, since it is not negligible, to obtain the creep equivalent strain at the contact edge, $\varepsilon^{c}_{EQ,EDGE}$, as shown in equation (8.2).

$$\varepsilon^{c}_{EQ,EDGE} = \varepsilon_{EQ,EDGE} - \varepsilon^{in}_{EQ,EDGE} \tag{8.2}$$

In the present calculations, the initial strain, $\varepsilon^{in}_{EQ,EDGE}$ was taken to be equal to the value obtained by equation (8.1) for the initial non-zero value of the punch displacement. This approach is not completely accurate, as equation (8.1) is only valid for $h_{punch} > 0.8$ [mm] because, at the beginning of the test, the governing deformation mechanism is bending. No other analytical methods to convert the central displacement to equivalent strain at the contact edge are currently available for this stage of the test.

By using the same FE model as that of the calculations discussed in Chapter 5, additional numerical analyses of SPCT were carried out with a load of 40 [kg].

Figure 8.2 shows the plot of $\varepsilon_{EQ,EDGE}$, obtained by use of the FE results, versus time, for the 4 load levels adopted in the calculations.

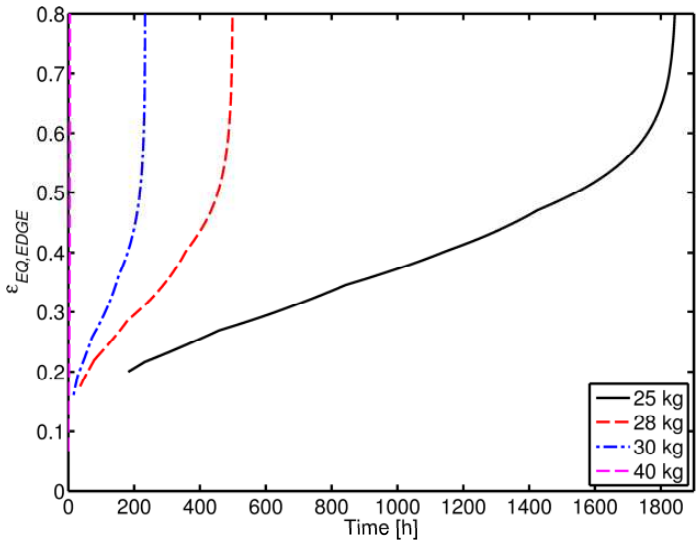

Figure 8.2: Time variation of $\varepsilon_{EQ,EDGE}$, converted from SPCT punch displacement FE results by use of equations (8.1)-(8.2).

8.2.2 Conversion of the punch load to the stress level

The punch load, *P*, can be correlated to a characteristic stress level acting during SPCTs by using a physically-based approach. However, this correlation is also not straightforward because the stress field acting in the specimen is multi-axial and not homogeneous, furthermore, it changes over the test duration. On the other hand, the stress level of a standard uniaxial creep test is uniform and constant over time. The correlation established by the CEN draft code of practice, reported in equation (2.65), between the load level and the 'equivalent uniaxial stress' is based on the equality of the time to failure of SPCT and equivalent uniaxial test, but the FE calculations discussed in Chapter 5 show that the real stress field acting in the specimen is higher than the stress calculated by using equation (2.65).

In the calculations presented in this Chapter, the load level of SPCTs was correlated to the minimum value of the peak rupture stress, σ^{p}_{RUP}, see equation (2.25) and below. The

rupture stress is capable of taking into account the effects of the stress multi-axiality in the structure and its peak value obtained when the punch displacement is larger than 0.8 [mm] (i.e. when membrane stretching becomes the governing deformation mechanism) can be assumed to characterise the multi-axial stress field acting in the specimen over the majority of the test duration.

$$\sigma_{RUP} = \alpha_D \sigma_1 + (1 - \alpha_D)\sigma_{EQ}$$

By using the results of the FE analyses of Chapter 5,in which the effects of initial plastic deformation were taken into account, the punch load level was then related to the minimum value of the peak rupture stress (obtained when membrane stress becomes predominant) by a linear fitting, reported in equation (8.3). Figure 8.3 shows the variation of σ^p_{RUP} versus the punch load with a plot of equation (8.3).

$$\sigma^p_{RUP} = 6.135\ P + 21.61 \tag{8.3}$$

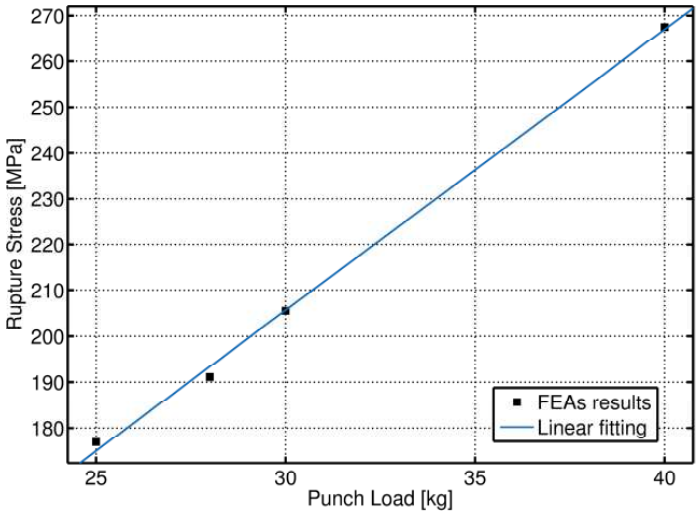

Figure 8.3: Variation of σ^p_{RUP}, obtained by FE analyses of SPCT, versus the punch load, together with the fitting represented by equation (8.3).

This correlation is also applicable to the experimental SPCT results discussed in Chapter 3, as the geometry of the experimental set-up is the same as that used for the calculations reported in Chapter 5.

8.2.3 Inclusion of pre-straining effects - minimum strain rate correction

In the FE analyses reported in Chapter 5, a significant effect of material pre-straining on the SPCT output was observed. This effect can be used to investigate the equivalent minimum strain versus time, obtained by converting the punch displacement, h_{punch}, into the equivalent strain at the punch/specimen contact edge, $\varepsilon_{EQ,EDGE}$, by use of equations (8.1) and (8.2).

The ratio between the minimum strain rate calculated by converting the punch displacement curves obtained by FE analyses with pre-strain effects included ($MSR_{SPCT,PRE}$) to the *MSR* obtained from FE results without including these effects ($MSR_{SPCT,N-PRE}$), is defined as the γ parameter, reported in equation (8.4).

$$\gamma = \frac{MSR_{SPCT,PRE}}{MSR_{SPCT,N-PRE}} = \frac{MSR_{EXP}}{MSR_{CORR}} \tag{8.4}$$

The variation of γ with the load level, *P*, used in the FE calculations, was also fitted by using a polynomial relation, reported in equation (8.5).

$$\gamma = 2.485 \times 10^{-3}\ P^2 - 0.1325\ P + 1.853 \tag{8.5}$$

Figure 8.4 shows the plot of γ, obtained from the creep strain plotted in Figure 8.2, versus the load level together with the plot of equation (8.5).

Several sources of uncertainty, such as the friction contact conditions (see Chapter 7), should be taken into account when comparing the FE results obtained without pre-straining effects to the experimental results, and the identification of initial plastic deformation would not be possible without the use of FE results obtained by a constitutive model capable to take into account pre-strain effects.

In the present Chapter, since testing results were available, the variation of h_{punch}

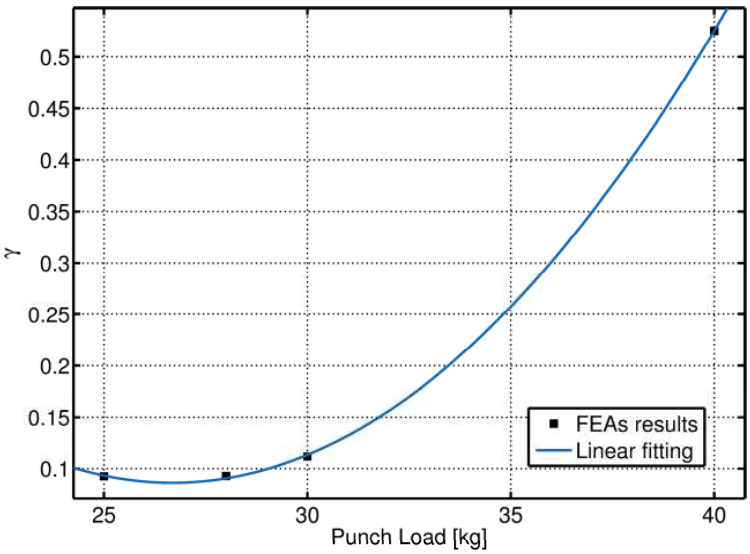

Figure 8.4: Variation of the γ and λ_f parameters with the punch load, obtained by FE analyses results.

obtained by experimental data was converted to $\varepsilon_{EQ,EDGE}$. The corresponding experimental minimum strain rate, MSR_{EXP}, corresponds to the minimum strain rate obtained from SPCT FE calculations with the pre-straining effects accounted for, i.e. $MSR_{FE,PRE}$. In order to isolate the effects pre-straining induces on the material, and to obtain an indication of the creep behaviour of not pre-strained material, a 'modified minimum strain rate', i.e. MSR_{CORR}, was obtained by dividing MSR_{EXP} by the γ parameter, as shown in equation (8.4). MSR_{CORR} corresponds to the minimum strain rate, $MSR_{FE,N-PRE}$, obtained by FE calculations of SPCT without accounting for the pre-straining effects and it can be then compared with the *MSR* of a standard uniaxial creep test carried out at the peak rupture stress obtained by SPCT FE analyses when membrane stretching takes over bending deformation because, for a uniaxial creep test, $\sigma = \sigma^p_{RUP}$.

8.2.4 Inclusion of pre-straining effects - time to failure correction

Similarly to the approach discussed in Section 8.2.3 for the minimum strain rate, the rupture behaviour of SPCTs, was also investigated by use of the numerical results of Chapter 5.

The λ_f parameter, defined by equation (8.6) is the ratio of the failure time obtained by FE analyses of SPCT performed without including the pre-straining effects, $t_{fFE,N-PRE}$, to

that obtained with these effects included, $t_{fFE,PRE}$. As for the case of γ, if an overall creep resistance effect was found for SPCT FE results when pre-straining effects were included (with respect to the results obtained without accounting for pre-straining effects) λ_f is less than unity, while, when $\lambda_f > 1$, overall creep enhancement was observed in FE analyses results.

$$\lambda_f = \frac{t_{fFE,N-PRE}}{t_{fFE,PRE}} = \frac{t_{f,CORR}}{t_{f,EXP}} \tag{8.6}$$

The variation of λ_f versus P was also investigated and, similarly to the case of the minimum strain rate correction, a quadratic polynomial fitting to the corresponding FE results, reported in equation (8.7), was obtained.

$$\lambda_f = 2.521 \times 10^{-3}\, P^2 - 0.1319\, P + 1.814 \tag{8.7}$$

Figure 8.5 shows the plot of λ_f versus the load level obtained from the FE rupture results together with the plot of equation (8.7).

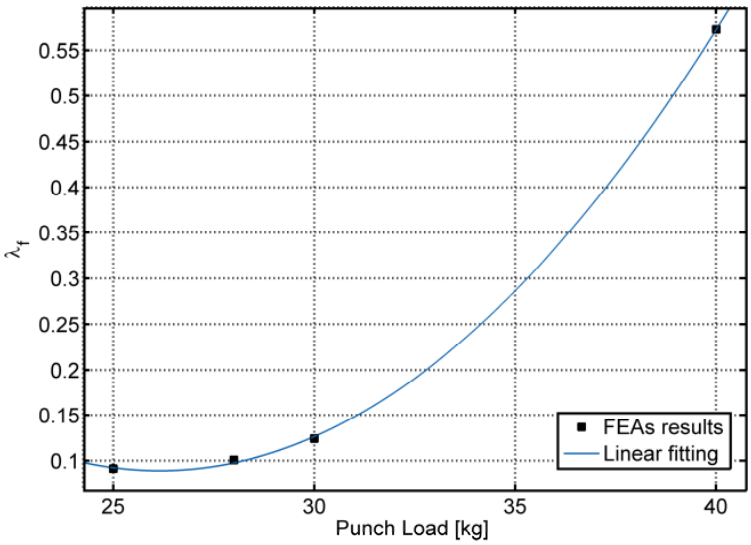

Figure 8.5: Variation of the γ and λ_f parameters with the punch load, obtained by FE analyses results.

Similarly to the case of the *MSR* correlation, this parameter was used to calculate a

'modified' failure time, $t_{f,CORR}$ from the experimental results, $t_{f,EXP}$, in order to isolate the effects of pre-straining. The 'modified' failure time, $t_{fSPCT,CORR}$, can be compared to the failure time of a standard uniaxial creep test performed at a stress level, σ, equal to the minimum value of the peak rupture stress, σ^{p}_{RUP} obtained by FE analyses under membrane stretching-dominant regime (i.e. h_{punch} larger than 0.8 [mm]).

8.3 Conversion of SPCT results for a P91 steel at 600°C

The correlation procedure to relate SPCT output with corresponding uniaxial data described in Section 8.2 was used to convert the experimental results of the SPCTs of P91 steel at 600°C, discussed in Chapter 3, to corresponding uniaxial *MSR* and time to rupture. The effects of initial plastic deformation on the output of SPCTs were taken into account by using the γ and λ_f parameters, obtained by the FE calculations reported in Chapter 5, which were presented in Sections 8.2.3 and 8.2.4, respectively.

The equivalent strain at the punch/specimen contact edge, assumed to be the strain characterising the behaviour of the specimen during the test because it is calculated at the critical location, was obtained by use of equations (8.1) and (8.2). Figure 8.6 shows the variation of the equivalent creep strain versus time obtained from SPCT experimental displacement curves.

According to equations (8.1) and (8.2), the creep strain plotted in Figure 8.6 depends on h_{punch} and on its value when $t = 0$, i.e. h^{in}_{punch}. When the load level decreases, h^{in}_{punch} and $\varepsilon^{in}_{EQ,EDGE}$ decrease as well, therefore, at a constant punch displacement level, for example $h_{punch} = 1.0$ [mm], the creep strain increases.

From the results reported in Chapter 3, the K_{SP} parameter was found to be 1.353. This value led to 'equivalent uniaxial stresses', σ^{UNI}_{EQ}, significantly lower than the stress levels obtained in the specimen by use of FE analyses for all of load levels.

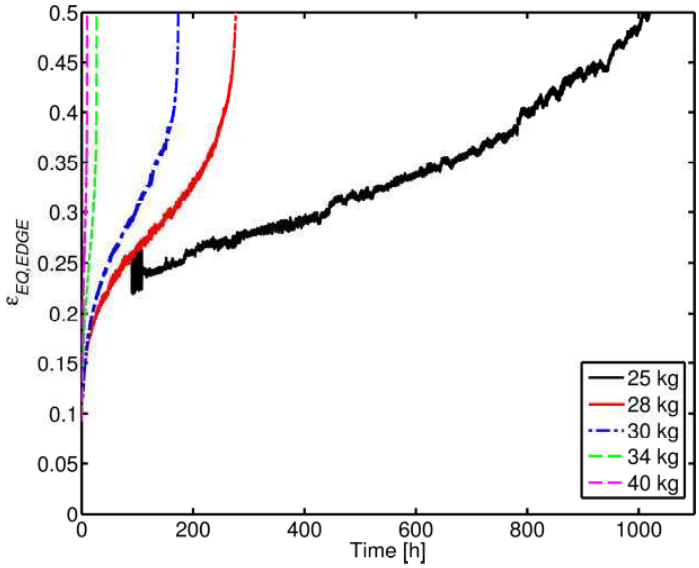

Figure 8.6: Variation of the $\varepsilon_{EQ,EDGE}$, converted from SPCT punch displacement, versus time [h] obtained by equations (8.1)-(8.2).

The punch load used for the experiments were converted into the corresponding values of the peak rupture stress (in the membrane stretching regime) by using equation (8.3), and Table 8.2 compares these values with the 'equivalent uniaxial stress', σ_{EQ}^{UNI}, obtained by using the procedure reported in the draft CEN code of practice, for all of the load levels.

Table 8.2: 'Equivalent uniaxial stress', σ_{EQ}^{UNI}, and minimum peak rupture stress, σ_{RUP}^{p}, obtained by using equation (8.3), for the various loads used for SPCTs.

P [kg]	σ_{EQ}^{UNI}	σ_{RUP}
25	143.704	174.985
28	162.417	193.390
30	169.574	205.660
34	200.992	230.200
40	220.371	267.010

The discrepancies between σ_{EQ}^{UNI} and σ_{RUP}^{p} shown in Table 8.2 indicate that the stress field in the SPCT specimen is higher than that of a uniaxial test characterised by the same failure time. In view of these observations, the corrections described in Sections 8.2.3 and 8.2.4 for the *MSR* and t_f, respectively, were applied to the results obtained from the SPCT data shown in Figure 8.6. Also, the uniaxial data, calculated for stress levels equal to the values of σ_{RUP}^{p}, corresponding to each load level, were compared with the modified SPCT results.

From Figure 8.6, the experimental minimum strain rate, MSR_{EXP}, was calculated. As discussed in Section 8.2.3, this strain rate corresponds to the minimum strain rate, MSR_{PRE}, obtained from FE calculations of SPCT with the pre-straining effects accounted for. In order to obtain the minimum creep rate of not pre-strained material, the 'corrected' minimum strain rate, MSR_{CORR}, was calculated by dividing MSR_{EXP} by γ which is obtained by equation (8.5) for each load level.

Figure 8.7 shows the variation of MSR_{CORR} versus σ^p_{RUP}. Also, the variation of MSR_{EXP} versus σ^p_{RUP} is shown in Figure 8.7 with the corresponding uniaxial secondary creep data, obtained by using Norton's law, equation (2.18) with the stress equal to the values of σ^p_{RUP} of Table 8.2 (for uniaxial tests, σ is equal to $\sigma_{RUP} = const$) and the material constants $B = 1.510 \times 10^{-30}$ and $n = 11.795$ (with the stress in [MPa] and time in [h]).

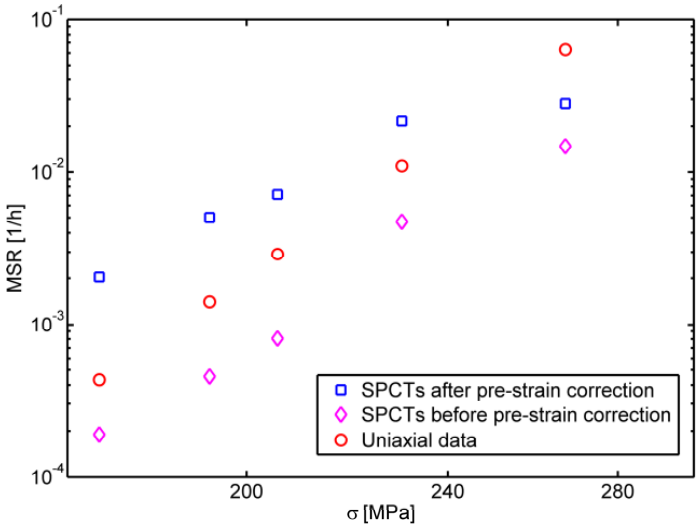

Figure 8.7: Variation of MSR_{CORR} and MSR_{EXP} versus σ^p_{RUP}, together with corresponding uniaxial results.

The failure time was modified by using the procedure described in Section 8.2.4. The experimental time to failure, $t_{fSPCT,EXP}$, is shown in Chapter 3, see Figure 3.9, and, for each load level, the 'corrected' time to failure, $t_{f,CORR}$, was calculated by multiplying $t_{f,EXP}$ by λ_f, calculated for each load level by use of equation (8.7). Figure 8.8 shows the plots of $t_{f,EXP}$ and $t_{f,CORR}$ versus σ^p_{RUP} for all of load levels used in the SPCTs, with the corresponding uniaxial rupture data, obtained by using the stress levels indicated in Table 8.2, with $\sigma = \sigma_{RUP}$, and the rupture material properties, A_{LM} and χ listed in Table 5.2,

i.e. $A_{LM} = 2.120 \times 10^{-27}$ and $\chi = 10.953$ (with the stress in [MPa] and time in [h]).

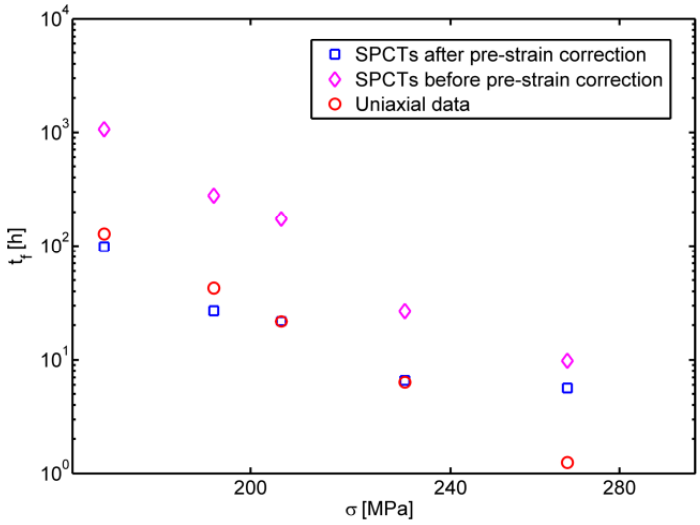

Figure 8.8: Variation of $t_{f,CORR}$ and $t_{f,EXP}$ versus σ^p_{RUP}, together with corresponding uniaxial results.

The results of Figure 8.7 show that the estimations of the minimum strain rate do not exhibit a significant improvement by use of the γ parameter, and they lead to an overestimation of the minimum strain rate for all of load levels except from the case with 40 [kg]. When the effects of pre-straining are not considered in the correlation, the minimum strain rate is underestimated for all of the stress range, with respect to the uniaxial data available.

Figure 8.8 shows that there is a significant improvement in the failure time estimations when the effects of pre-straining are taken into account by use of the λ_f parameter for all of the load levels adopted for testing except from the 40 [kg] case.

Discrepancies between the results corresponding to the lower load levels and those obtained from the 40 [kg] test were found in both Figure 8.7 and 8.8 because, in Chapter 5, the functions which take into account the effects of pre-straining on the creep behaviour of P91 steel at 600°C, i.e. ϕ and ψ, were assumed not to vary for the range of stress adopted in the uniaxial pre-strained creep tests (see equations (3.4) and (3.5)). As a consequence, the accuracy of ϕ and ψ is not constant when different stress levels, and different SPCT loads, are considered. This leads to a decrease in the accuracy of the FE results reported in Chapter 5 for higher load levels (for which the behaviour of the specimen was found to be mainly governed by plasticity, as observed in Chapter 4) and, in turn, a decrease in the

accuracy of γ and λ_f for the high loads.

The source of inaccuracy of the MSR estimations reported in Figure 8.7 can be related to the use of Chakrabarty's solution for the conversion of h_{punch}, to $\varepsilon_{EQ,EDGE}$. This solution does not take into account several factors, such as bending deformation, friction and material deterioration. Therefore, a more accurate conversion technique for strain is needed.

On the other hand, it should be noted that the results of Figure 8.8, based on the results of the FE analyses of Chapter 5, were not obtained by using the membrane stretching Chakrabarty theory. Therefore, in view of the findings of Figure 8.8, the FE results obtained by using the modified creep damage model, capable of taking into account the effects of initial plasticity occurring at the beginning of the test, can provide accurate results for 4 of the 5 load levels.

8.4 Conclusions

The correlation procedure reported in this Chapter leads to estimations of *MSR* and t_f of 'equivalent' uniaxial creep tests by use of FE analyses capable of accounting for the effects of large initial plastic deformations which occur in the specimen. The procedure to convert experimental SPCT data consists of the following steps:

- Conversion of the punch displacement to creep strain, by use of equation (8.1) and calculation of the experimental minimum strain rate MSR_{EXP}
- Conversion of the punch load to minimum value of the peak rupture stress (in membrane stretching regime), σ^p_{RUP} by using equation (8.3)
- Calculation of γ and λ_f by using equations (8.5) and (8.7), respectively
- Calculation of $MSR_{CORR} = MSR_{EXP}/\gamma$ for each load level
- Calculation of $t_{f,CORR} = t_{f,EXP}\lambda_f$ for each load level

The procedure to calculate the 'modified' minimum strain rate was found to be affected by the inaccuracies due to the application of the Chakrabarty model, while the time to failure modification produced a significant improvement of the results for the majority of the punch load range investigated.

The results for the highest load level, i.e. 40 [kg], show a decrease in accuracy because the parameters which take into account the effects of pre-straining on the creep behaviour of P91 steel, defined in Chapter 3, are averaged over the stress range used for the tests, and therefore, their accuracy is not constant in the stress range and, in the case of SPCTs, in the load range.

CHAPTER 9

CONCLUSIONS AND FUTURE WORK

9.1 Concluding remarks

The research reported and discussed in this thesis was aimed to improve the understanding of different features which characterise the behaviour of the SPCT specimen and to develop an improved interpretation technique of the experimental results.

The experimental investigations, discussed in Chapter 3, consist of two testing programmes, i.e. pre-strained uniaxial creep tests and SPCTs. All of the tests reported in this work were carried out on the same batch of P91 steel at 600°. The pre-strained creep tests were carried out at stresses of 150, 160 and 170 [MPa], and different pre-strain levels were used for them. These tests showed that the plastic deformation generated by loading uniaxial creep specimens at high temperature has a very significant effect on the subsequent creep behaviour of P91 steel. This effect is generated by the modification of the density and mobility of dislocations in the material and it varies with the amount of pre-straining and the creep test stress level. This is an important feature to be considered in the modelling and interpretation procedures of SPCT, as large initial plastic deformation is generated in the specimen by the punch load.

The output of the SPCTs, which were carried out with a load ranging between 25 and 40 [kg], shows the typical three regions of SPCT curves. SEM investigations (reported

in Chapter 4) of the fracture surface of failed specimens revealed that the failure mechanism changed from creep governed (characterised by intergranular separation) to plasticity governed (characterised by the presence of fresh dimples) when the load was increased. Furthermore, subgrain rotation near the fracture location increased when the load was increased. A reduction of oxide in the fracture surface was also found when the load was increased, as all of the tests were performed in air and the shorter test duration of high-load tests did not allow for extensive oxidisation to take place in the specimens. The investigation of interrupted test specimens pointed out that a macro-crack starts to nucleate at about 20 % of the failure time and it propagates in the circumferential direction and through the thickness of the specimen. After 669 [h], the macro-crack had propagated around the whole specimen and secondary micro-cracks were found at the tip of the macro-crack.

Finite element (FE) calculations of small punch creep tests were carried out by using a modified creep constitutive model capable of taking into account the effects of the initial plastic deformation generated by the test load on the subsequent creep behaviour of the small disc specimen. The model was developed by using the results of pre-strained uniaxial creep tests. These analyses, reported in Chapter 5, showed that initial plasticity led to a significant resistance in the global creep response of specimen, compared to the calculations performed by using a conventional creep damage constitutive model. The global behaviour of the specimen is characterised by the combination of local creep enhancement occurring in the region of the specimen near the edge of contact between the punch and the specimen, and local creep resistance which takes place in the unsupported region of the sample. The peak damage location did not change when the effects of initial loading plasticity were accounted for, but the propagation direction of the high damage region in the specimen changed as a result of the local modification of the creep response of the material in the specimen.

The FE calculations reported in Chapter 6 were performed to investigate the effects of inaccuracies in the punch loading procedures. The analyses were carried out with different initial positions of the punch and different loading directions, and the effects of the load misalignment and eccentricity on the minimum displacement rate, *MDR*, and the time to failure, t_f, were investigated. When the punch load misalignement and eccentricity in-

creased, the *MDR* was found to decrease, while t_f increased. These effects were particularly markable when the punch eccentricity was larger than 0.2 [mm] and the misalignment was larger than 2°. In these analyses, an elastic/steady-state creep constitutive model was used and the results were compared with those of an additional set of FE calculations performed by using the Liu & Murakami creep damage model. The effects of geometrical inaccuracies obtained by using the secondary creep constitutive model were found to be similar to those obtained by creep damage calculations.

In this thesis, also the effects of non-linear friction, characterising the interaction between the punch and the specimen, were investigated and the results were reported in Chapter 7. A modern friction formulation, proposed by Leu and also used for metal forming, was implemented in an SPCT FE model to describe the variation of the coefficient of friction, μ, with the local loading conditions, that is, the contact pressure, p. These FE calculations showed that the coefficient of friction varied considerably over the contact surface with a distribution that changes during the creep step duration. The peak value of μ was found at the edge of contact for the majority of creep step, and its variation influences the test output.

The experimental studies and the numerical investigations discussed in Chapters 3 and 5, respectively, were used to develop a novel technique for the interpretation of SPCT output and the correlation with corresponding uniaxial data. This technique was reported in Chapter 8 and correlates the punch load, P, with the minimum value of the peak rupture stress, σ^{p}_{RUP} (calculated from FE analyses results when membrane stretching governs the deformation of the specimen) and the punch displacement, h_{punch}, with the equivalent creep strain at the punch/specimen contact edge, calculated by using the Chakrabarty's membrane stretching theory. The minimum displacement rate and the time to failure obtained for various load levels were modified by use of two parameters, γ and λ_f, which were obtained from the FE results of Chapter 5 and take into account the effects of the loading plasticity on the global creep response of the SPCT specimen. By use of γ and λ_f, the effects of pre-straining were 'isolated' and the creep response of the not pre-strained material was identified by use of SPCT results. The estimations of the modified minimum strain rate

and of and time to failure were compared with corresponding uniaxial creep test data. A significant improvement in the accuracy of the time to rupture estimations was obtained when the effects of pre-straining were taken into account in the interpretation technique, while the correlation of the *MSR* showed a lower degree of accuracy, which can be due to the use of Chakrabarty's theory of membrane stretching.

9.2 Future work

This thesis was aimed to improve the understanding of different features governing the response of the SPCT specimen, but several issues still remain open. Further development of some of the aspects of the work reported in the present thesis can lead to an improvement of the accuracy of the numerical models and the completeness of the experimental investigations.

The pre-strained uniaxial creep testing programme, reported in Chapter 3, should include more pre-straining levels and more creep test stresses. This will lead to a more accurate fitting function of the pre-strain parameters, i.e. ϕ and ψ, in the pre-strain range adopted. Furthermore, by use of a wider experimental stress range, the variation of the pre-strain parameters with stress can be modelled, in order to replace the average of the fittings over different stresses, and to have a more accurate modelling procedure for the effects of initial plasticity on the subsequent creep response of the material. The improvements in the accuracy of the ϕ and ψ parameters will, in turn, improve the accuracy of the modified constitutive model and of the FE results of SPCT.

The experimental data correlation procedure should also be improved in order to increase the accuracy of the estimations of corresponding uniaxial data. The improvement of the fitting functions for ϕ and ψ will also be reflected into an improvement of the estimations of the SPCT parameters, γ and λ_f.

Further improvements are also possible for the modelling procedure of the variation of the coefficient of friction, μ, with the local loading conditions. This model should also

account for the effects of thermal adhesion which can be significant at high temperature and, in addition, an experimental procedure to validate the numerical results should also be developed.

A further investigation could include small punch creep testing under different clamping forces, correlated with corresponding numerical calculations in order to also investigate the effects of this factor which can potentially influence the experimental results. In a long term SPCT, the clamping force, applied to the outer annular region of the specimen, can increase the creep deformation in the ring of material that, in view of the constant volume condition valid during creep deformation, modifies the response of the unsupported region of the specimen

REFERENCES

[1] 'CEN Workshop agreement for Small Punch Test Method for Metallic Materials', *CWA 15627*, Brussels, December 2006.

[2] F. Al-Bender and K. De Moerlooze, 'On the relationship between normal load and friction force in pre-sliding frictional contacts. Part 1: Theoretical analysis', *Wear*, **269** (3-4), pp. 174–182, 2010.

[3] M. Ashby, H. Shercliff and D. Cebon, *Materials Engineering, Science, Processing and Design*, Butterworth - Heinemann, Oxford, UK, 2014.

[4] M. Basirat, T. Shrestha, G. P. Potirniche, I. Charit and K. Rink, 'A study of the creep behavior of modified 9Cr-1Mo steel using continuum-damage modeling', *International Journal of Plasticity*, **37** (0), pp. 95–107, 2012.

[5] A. Bertram, *Elasticity and Plasticity of Large Deformations*, Springer, Berlin, Heidelberg, New York, 2005.

[6] J. Betten, *Creep mechanics, 3^{rd} edition*, Springer, Berlin, London, 2008.

[7] V. Bicego, E. Lucon and R. Crudeli, 'Integrated technologies for life assessment of primary power plant components', *Nuclear Engineering and Design*, **182** (2), pp. 113–121, 1998.

[8] D. Blagoeva, Y. Z. Li and R. C. Hurst, 'Qualification of P91 welds through Small Punch creep testing', *Journal of Nuclear Materials*, **409** (2), pp. 124–130, 2011.

[9] F. P. Bowden and D. Tabor, *The Friction and Lubrication of Solids*, Oxford, 1953.

[10] J. H. Bulloch, 'The small punch toughness test: some detailed fractographic information', *International Journal of Pressure Vessels and Piping*, **63** (2), pp. 177–194, 1995.

[11] J. H. Bulloch, 'A review of the ESB small punch test data on various plant components with special emphasis on fractographic details', *Engineering Failure Analysis*, **9** (5), pp. 511–534, 2002.

[12] D. Callister, William, *Materials Science and Engineering - An Introduction - Fifth edition*, John Wiley & Sons, Hoboken, N.J., USA, 2000.

[13] J. Chakrabarty, 'A theory of stretch forming over hemispherical punch heads', *International Journal of Mechanical Sciences*, **12** (4), pp. 315–325, 1970.

[14] W. R. Chang, I. Etsion and D. B. Bogy, 'Static Friction Coefficient Model for Metallic Rough Surfaces', *Journal of Tribology*, **110** (1), pp. 57–63, 1988.

[15] S. Chaudhuri and R. N. Ghosh, 'Creep behavior of 2.25Cr-1Mo steel - Effects of thermal ageing and pre-strain', *Materials Science and Engineering: A*, **510-511**, pp. 136–141, 2009.

[16] J. Chen, Y. Ma and K. Yoon, 'Finite element study for determination of material's creep parameters from small punch test', *Journal of Mechanical Science and Technology*, **24** (6), pp. 1195–1201, 2010.

[17] S. Chu and J. Li, 'Impression creep; a new creep test', *Journal of Materials Science*, **12** (11), pp. 2200–2208, 1977.

[18] D. Cohen, Y. Kligerman and I. Etsion, 'A Model for Contact and Static Friction of Nominally Flat Rough Surfaces Under Full Stick Contact Condition', *Journal of Tribology*, **130** (3), pp. 031401–9, 2008.

[19] D. S. S. Corp., *ABAQUS Theory Manual*, Providence, RI, USA, 2010.

[20] F. Cortellino, T. H. Hyde, W. Sun and C. Pappalettere, 'Finite element calculation of contour integral parameters for cracked P91 pipe weld', *Materials Research Innovations*, **17** (5), pp. 300–305, 2013.

[21] B. Dogan and T. H. Hyde, 'Sampling and Small Punch Testing for Utility Services', in: K. Matocha, H. R and W. Sun (eds.), '2nd International Conference SSTT - Determination of mechanical properties of materials by small punch and other miniature testing techiques, Ostrava (CZ), October 2nd to 4th, 2012', pp. 26–37, OCELOT s.r.o.

[22] P. Dymacek and F. Dobes, 'Influence of Atmosphere on Small Punch Testing of P91 Steel', in: K. Matocha, H. R and W. Sun (eds.), '2nd International Conference SSTT - Determination of mechanical properties of materials by small punch and other miniature testing techiques, Ostrava (Czech Republic), October 2nd to 4th, 2012', pp. 75–78, OCELOT s.r.o.

[23] P. Dymacek and K. Milicka, 'Small punch testing and its numerical simulations under constant deflection force conditions', *Strength of Materials*, **40** (1), pp. 24–27, 2008.

[24] P. Dymacek and K. Milicka, 'Creep small-punch testing and its numerical simulations', *Materials Science and Engineering: A*, **510-511**, pp. 444–449, 2009.

[25] P. Dymacek, S. Stanislav, K. Milicka and F. Dobes, 'Influence of friction on stress and strain distributions in small punch creep test models', *Key Engineering Materials*, **417-418**, pp. 561–564, 2010.

[26] L. Esposito and N. Bonora, 'Time-independent formulation for creep damage modeling in metals based on void and crack evolution', *Materials Science and Engineering: A*, **510-511**, pp. 207–213, 2009.

[27] M. Evans and D. Wang, 'Optimizing the sensitivity of the small-disc creep test to damage and test conditions', *The Journal of Strain Analysis for Engineering Design*, **42** (5), pp. 389–409, 2007.

[28] M. Evans and D. Wang, 'Stochastic modelling of the small disc creep test', *Materials Science and Technology*, **23** (8), pp. 883–892, 2007.

[29] M. Evans and D. Wang, 'The small punch creep test: some results from a numerical model', *Journal of Materials Science*, **43** (6), pp. 1825–1835, 2008.

[30] R. W. Evans, 'A constitutive model for the high-temperature creep of particle-hardened alloys based on the θ projection method', *Proceedings of the Royal Society of London. Series A: Mathematical, Physical and Engineering Sciences*, **456** (1996), pp. 835–868, 2000.

[31] R. W. Evans and M. Evans, 'Numerical modelling of small disc creep test', *Materials Science and Technology*, **22** (10), pp. 1155–1162, 2006.

[32] K. Guan, L. Hua, Q. Wang, X. Zou and M. Song, 'Assessment of toughness in long term service CrMo low alloy steel by fracture toughness and small punch test', *Nuclear Engineering and Design*, **241** (5), pp. 1407–1413, 2011.

[33] K.-S. Guan, T. Xu, G. Zhang and Z.-W. Wang, 'Effect of Microdefects on Load-Deflection of Small Punch Test by Experimental Investigation and Finite Element Analysis', in: '13th International Conference on Pressure Vessel Technology, London, U.K., 20-23 May 2012', .

[34] B. Gulcimen and P. Hahner, 'Determination of creep properties of a P91 weldment by small punch testing and a new evaluation approach', *Materials Science and Engineering: A*, **588**, pp. 125–131, 2013.

[35] W. Han and B. D. Reddy, *Plasticity - Mathematical Theory and Numerical Analysis*, Springer, New York, Heidelberg, Dordrecht, London, 2013.

[36] S. Holmstrom, P. Auerkari, R. Hurst and D. Blagoeva, 'Using small punch test data to determine creep strain and strength reduction properties for heat affected zones', *Materials Science and Technology*, **30** (1), pp. 63–66, 2014.

[37] W. F. Hosford, *Foundamentals of Engineering Plasticity*, New York, N.Y., USA, 2013.

[38] R. C. Hurst, 'Standardisation-A Route to Enhancing the Acceptability of the Small Punch Creep Test', *Proc. of ECCC Creep Conf., 2005*, 2005.

[39] J. Hutchinson, 'Constitutive behavior and crack tip fields for materials undergoing

creep-constrained grain boundary cavitation', *Acta Metallurgica*, **31** (7), pp. 1079 – 1088, 1983.

[40] D. H. Hwang and K. H. Zum Gahr, 'Transition from static to kinetic friction of unlubricated or oil lubricated steel/steel, steel/ceramic and ceramic/ceramic pairs', *Wear*, **255** (1-6), pp. 365–375, 2003.

[41] C. J. Hyde, T. H. Hyde and W. Sun, 'Small Ring Creep Testing of a Nickel-based Superalloy', in: K. Matocha, H. R and W. Sun (eds.), '2nd International Conference SSTT - Determination of mechanical properties of materials by small punch and other miniature testing techiques, Ostrava (CZ), October 2nd to 4th, 2012', OCELOT s.r.o.

[42] C. J. Hyde, T. H. Hyde, W. Sun, S. Nardone and E. D. Bruycker, 'Small ring testing of a creep resistant material', *Materials Science and Engineering: A*, **586**, pp. 358 – 366, 2013.

[43] T. Hyde, 'Creep of 316 stainless steel at 550 and 600°C and the effects of short duration overloads on creep at 550°C', *Materials at High Temperatures*, **14** (1), pp. 27–35, 1997.

[44] T. H. Hyde, 'Anomalous creep behaviour of 316 stainless steel at 550°C', *High Temperature Technology*, **4** (1), pp. 25–29, 1986.

[45] T. H. Hyde, B. S. M. Ali and W. Sun, 'Analysis and Design of a Small, Two-Bar Creep Test Specimen', *Journal of Engineering Materials and Technology*, **135** (4), 2013.

[46] T. H. Hyde, B. S. M. Ali and W. Sun, 'On the Determination of Material Creep Constants Using Miniature Creep Test Specimens', *Journal of Engineering Materials and Technology*, **136** (2), 2014.

[47] T. H. Hyde, A. A. Becker, W. Sun and J. A. Williams, 'Finite-element creep damage analyses of P91 pipes', *International Journal of Pressure Vessels and Piping*, **83** (11-12), pp. 853–863, 2006.

[48] T. H. Hyde, F. Cortellino, J. P. Rouse and W. Sun, 'Small Punch Creep Testing and Data Analysis of a P91 Steel at 650°C', in: K. Matocha, H. R and W. Sun (eds.), '2nd International Conference SSTT - Determination of mechanical properties of materials by small punch and other miniature testing techiques, Ostrava (Czech Republic), October 2nd to 4th, 2012', pp. 64–74, OCELOT s.r.o.

[49] T. H. Hyde, M. Saber and W. Sun, 'Creep crack growth data and prediction for a P91 weld at 650°C', *International Journal of Pressure Vessels and Piping*, **87** (12), pp. 721–729, 2010.

[50] T. H. Hyde, M. Saber and W. Sun, 'Testing and modelling of creep crack growth in compact tension specimens from a P91 weld at 650°C', *Engineering Fracture Mechanics*, **77** (15), pp. 2946–2957, 2010.

[51] T. H. Hyde, M. Stoyanov, W. Sun and C. J. Hyde, 'On the interpretation of results from small punch creep tests', *The Journal of Strain Analysis for Engineering Design*, **45** (3), pp. 141–164, 2010.

[52] T. H. Hyde and W. Sun, 'Evaluation of conversion relationships for impression creep tests', *International Journal of Pressure Vessels and Piping*, **86**, pp. 757–763, 2009.

[53] T. H. Hyde and W. Sun, 'A novel, high sensitivity, small specimen creep test', *The Journal of Strain Analysis for Engineering Design*, **44**, pp. 171–185, 2009.

[54] T. H. Hyde, W. Sun and A. A. Becker, 'Analysis of the impression creep test method using a rectangular indenter for determining the creep properties in welds', *International Journal of Mechanical Sciences*, **38** (10), pp. 1189–1102, 1996.

[55] T. H. Hyde, W. Sun and C. J. Hyde, *Applied Creep Mechanics*, McGraw-Hill Education, USA, 2014.

[56] T. H. Hyde, W. Sun and J. A. Williams, 'Requirements for and use of miniature test specimens to provide mechanical and creep properties of materials: a review', *International Materials Reviews*, **52** (4), pp. 213–255, 2007.

[57] T. Izaki, T. Kobayashi, J. Kusumoto and A. Kanaya, 'A creep life assessment method for boiler pipes using small punch creep test', *International Journal of Pressure Vessels and Piping*, **86** (9), pp. 637–642, 2009.

[58] S. Kikuchi and B. Ilschner, 'Effects of a small prestrain at high temperatures on the creep behaviour of AISI 304 stainless steel', *Scripta Metallurgica*, **20** (2), pp. 159–162, 1986.

[59] K.-i. Kobayashi, I. Kajihara, H. Koyama and G. Stratford, 'Deformation and Fracture Mode during Small Punch Creep Tests', *Journal of Solid Mechanics and Materials Engineering*, **4** (1), pp. 75–86, 2010.

[60] K.-i. Kobayashi, M. Kaneko, H. Koyama, G. C. Stratford and M. Tabuchi, 'The Influence of Both Testing Environment and Fillet Radius of the Die Holder on the Rupture Life of Small Punch Creep Tests', *Journal of Solid Mechanics and Materials Engineering*, **6** (8), pp. 925–934, 2012.

[61] L. Kogut and I. Etsion, 'A Semi-Analytical Solution for the Sliding Inception of a Spherical Contact', *Journal of Tribology*, **125** (3), pp. 499–506, 2003.

[62] L. Kogut and I. Etsion, 'A Static Friction Model for Elastic-Plastic Contacting Rough Surfaces', *Journal of Tribology*, **126** (1), pp. 34–40, 2004.

[63] H. Kraus, *Creep Analysis*, John Wiley & Sons, Inc., New York, NY (USA), 1980.

[64] T. Kutty, S. Kaity and A. Kumar, 'Impression Creep Behaviour of U-6%Zr Alloy: Role of Microstructure', *Procedia Engineering*, **55**, pp. 561–565, 2013, 6$^{\text{th}}$ International Conference on Creep, Fatigue and Creep-Fatigue Interaction.

[65] D.-K. Leu, 'A simple dry friction model for metal forming process', *Journal of Materials Processing Technology*, **209** (5), pp. 2361–2368, 2009.

[66] D. F. Li, N. P. O'Dowd, C. M. Davies and K. M. Nikbin, 'A review of the effect of prior inelastic deformation on high temperature mechanical response of engineering alloys', *International Journal of Pressure Vessels and Piping*, **87** (10), pp. 531–542, 2010.

[67] J. C. Li, 'Impression creep and other localized tests', *Materials Science and Engineering: A*, **322** (1-2), pp. 23–42, 2002.

[68] R. Li, T. H. Hyde, W. Sun and B. Dogan, 'Modelling and Data Interpretation of Small Punch Creep Testing', in: 'AMSE 2011 Pressure Vessels and Piping Conference, Baltimore (MD), USA, July 17-21, 2011', volume 6, pp. 1119–1127, New York: ASME.

[69] Y. Li and R. Sturm, 'Determination of creep properties from small punch test', in: 'AMSE 2008 Pressure Vessels and Piping Conference, Vol.3, Chicago (IL), USA, July 27-31, 2008', pp. 739–750, New York: ASME.

[70] F. H. Lin and A. A. Tseng, 'A finite element analysis of elasto-plastic contact problems in metal forming', *Materials and Design*, **19** (3), pp. 99–108, 1998.

[71] J. Lin, Y. Liu and T. A. Dean, 'A Review on Damage Mechanisms, Models and Calibration Methods under Various Deformation Conditions', *International Journal of Damage Mechanics*, **14** (4), pp. 299–319, 2005.

[72] X. Ling, Y. Zheng, Y. You and Y. Chen, 'Creep damage in small punch creep specimens of Type 304 stainless steel', *International Journal of Pressure Vessels and Piping*, **84** (5), pp. 304–309, 2007.

[73] Y. Liu and S. Murakami, 'Damage Localization of Conventional Creep Damage Models and Proposition of a New Model for Creep Damage Analysis', *JSME International Journal Series A*, **41** (1), pp. 57–65, 1998.

[74] P. Lombardi, L. Cipolla, P. Folgarait, N. Bonora and L. Esposito, 'New time-independent formulation for creep damage in polycrystalline metals and its specialisation to high alloy steel for high-temperature applications', *Materials Science and Engineering: A*, **510-511**, pp. 214–218, 2009.

[75] M. Loveday and B. Dyson, 'Prestrain-induced particle microcracking and creep cavitation in IN597', *Acta Metallurgica*, **31** (3), pp. 397 – 405, 1983.

[76] Y. W. Ma, S. Shim and K. B. Yoon, 'Assessment of power law creep constants of Gr91 steel using small punch creep tests', *Fatigue and Fracture of Engineering Materials and Structures*, **32** (12), pp. 951–960, 2009.

[77] M. Madia, S. Foletti, G. Torsello and A. Cammi, 'On the applicability of the small punch test to the characterization of the 1CrMoV aged steel: Mechanical testing and numerical analysis', *Engineering Failure Analysis*, **34**, pp. 189–203, 2013.

[78] M. P. Manahan, A. S. Argon and O. K. Harling, 'The development of a miniaturized disk bend test for the determination of postirradiation mechanical properties', *Journal of Nuclear Materials*, **104**, pp. 1545–1550, 1981.

[79] A. Mehmanparast, C. M. Davies, D. W. Dean and K. M. Nikbin, 'The influence of pre-compression on the creep deformation and failure behaviour of Type 316H stainless steel', *Engineering Fracture Mechanics*, **110**, pp. 52–67, 2013.

[80] K. Milicka and F. Dobes, 'Small punch testing of P91 steel', *International Journal of Pressure Vessels and Piping*, **83** (9), pp. 625–634, 2006.

[81] S. Murakami, Y. Liu and M. Mizuno, 'Computational methods for creep fracture analysis by damage mechanics', *Computer Methods in Applied Mechanics and Engineering*, **183** (1-2), pp. 15–33, 2000.

[82] Naveena, V. Vijayanand, V. Ganesan, K. Laha and M. Mathew, 'Evaluation of the effect of nitrogen on creep properties of 316LN stainless steel from impression creep tests', *Materials Science and Engineering: A*, **552**, pp. 112 – 118, 2012.

[83] M. Pandey, A. Mukherjee and D. Taplin, 'Prior deformation effects on creep and fracture in inconel alloy X-750', *Metallurgical Transactions A*, **15** (7), pp. 1437–1441, 1984.

[84] J. D. Parker and B. Wilshire, 'Non-destructive life assessment of high temperature components and weldments', *International Journal of Pressure Vessels and Piping*, **50** (1-3), pp. 337–347, 1992.

[85] R. K. Penny and D. L. Marriott, *Design for Creep*, Chapman & Hall, London (UK), 1995.

[86] S. Rashno, B. Nami and S. Miresmaeili, 'Impression creep behavior of a cast MRI153 magnesium alloy', *Materials & Design*, **60**, pp. 289 – 294, 2014.

[87] K. J. R. Rasmussen, 'Full-range stress-strain curves for stainless steel alloys', *Journal of Constructional Steel Research*, **59** (1), pp. 47–61, 2003.

[88] D. Rees, *Basic Engineering Plasticity*, Oxford: Elsevier Ltd., 2006.

[89] M. Renouf, F. Massi, N. Fillot and A. Saulot, 'Numerical tribology of a dry contact', *Tribology International*, **44** (7-8), pp. 834–844, 2011.

[90] H. Riedel, *Fracture at high temperatures*, Springer-Verlag, Berlin, Heidelberg, 1988.

[91] J. P. Rouse, F. Cortellino, W. Sun, T. H. Hyde and J. Shingledecker, 'Small punch creep testing: review on modelling and data interpretation', *Materials Science and Technology*, **29** (11), pp. 1328–1345, 2013.

[92] A. A. Saad, T. H. Hyde, W. Sun, C. J. Hyde and D. W. J. Tanner, 'Characterization of viscoplasticity behaviour of P91 and P92 power plant steels', *International Journal of Pressure Vessels and Piping*, **111-112**, pp. 246–252, 2013.

[93] A. P. Semenov, 'Tribology at high temperatures', *Tribology International*, **28** (1), pp. 45–50, 1995.

[94] T. Shrestha, M. Basirat, I. Charit, G. P. Potirniche and K. K. Rink, 'Creep rupture behavior of Grade 91 steel', *Materials Science and Engineering: A*, **565**, pp. 382–391, 2013.

[95] C. Soyarslan and A. E. Tekkaya, 'A damage coupled orthotropic finite plasticity model for sheet metal forming: CDM approach', *Computational Materials Science*, **48** (1), pp. 150–165, 2010.

[96] E. I. Starovoitov and F. B. Nagiyev, *Foundations of the Theory of Elasticity, Plasticity and Viscoplasticity*, USA and Canada, 2013.

[97] W. Sun, T. H. Hyde and S. J. Brett, 'Small specimen creep testing and application for power plant component remaining life assessment', in: J. Silva Gomes and S. Meguid (eds.), '4th International Conference on Integrity, Reliability and Failure. Funchal, Madeira (PT), June 23rd to 27th, 2013', Edições INEGI.

[98] W. Sun, T. H. Hyde and S. J. Brett, 'Use if the Impression Creep Test Method for Determining Minimum Creep Strain Rate Data', in: K. Matocha, R. Hurst and W. Sun (eds.), '2nd International Conference SSTT - Determination of mechanical properties of materials by small punch and other miniature testing techiques, Ostrava (CZ), October 2nd to 4th, 2012', pp. 297–304, OCELOT s.r.o.

[99] D. Tabor, 'Junction Growth in Metallic Friction: The Role of Combined Stresses and Surface Contamination', *Proceedings of the Royal Society of London. Series A. Mathematical and Physical Sciences*, **251** (1266), pp. 378–393, 1959.

[100] D. Tabor, 'Friction—The Present State of Our Understanding', *Journal of Lubrication Technology*, **103** (2), pp. 169–179, 1981.

[101] K. Tai and T. Endo, 'Effect of pre-creep on the succeeding creep behavior of a 2.25Cr-1Mo steel', *Scripta Metallurgica et Materialia*, **29** (5), pp. 643–646, 1993.

[102] L. Wang, Y. He, J. Zhou and J. Duszczyk, 'Modelling of plowing and shear friction coefficients during high-temperature ball-on-disc tests', *Tribology International*, **42** (1), pp. 15–22, 2009.

[103] M. Whittaker, P. Jones, C. Pleydell-Pearce, D. Rugg and S. Williams, 'The effect of prestrain on low and high temperature creep in Ti834', *Materials Science and Engineering: A*, **527** (24-25), pp. 6683–6689, 2010.

[104] M. Willis, A. McDonaugh-Smith and R. Hales, 'Prestrain effects on creep ductility of a 316 stainless steel light forging', *International Journal of Pressure Vessels and Piping*, **76** (6), pp. 355–359, 1999.

[105] B. Wilshire and C. J. Palmer, 'Strain accumulation during dislocation creep of prestrained copper', *Materials Science and Engineering: A*, **387-389**, pp. 716–718, 2004.

[106] B. Wilshire and M. T. Whittaker, 'The role of grain boundaries in creep strain accumulation', *Acta Materialia*, **57** (14), pp. 4115–4124, 2009.

[107] B. Wilshire and M. Willis, 'Mechanisms of strain accumulation and damage development during creep of prestrained 316 stainless steels', *Metallurgical and Materials Transactions A*, **35** (2), pp. 563–571, 2004.

[108] S. Yang, J. Zhou, X. Ling and Z. Yang, 'Effect of geometric factors and processing parameters on plastic damage of SUS304 stainless steel by small punch test', *Materials and Design*, **41**, pp. 447–452, 2012.

[109] Z. Yang and Z. Wang, 'Relationship between strain and central deflection in small punch specimens', *International Journal of Pressure Vessels and Piping*, **80**, pp. 397–404, 2003.

[110] P.-C. Zhai, G. Chen, T. Hashida and Q.-J. Zhang, 'Evaluation on Small Punch Creep Test by Finite Element Method', *Key Engineering Materials*, **297-300**, pp. 377–383, 2005.

[111] L. Zhao, H. Jing, L. Xu, Y. Han, J. Xiu and Y. Qiao, 'Evaluating of creep property of distinct zones in P92 steel welded joint by small punch creep test', *Materials and Design*, **47**, pp. 677–686, 2013.

[112] W. Zheng, G. Wang, G. Zhao, D. Wei and Z. Jiang, 'Modeling and analysis of dry friction in micro-forming of metals', *Tribology International*, **57**, pp. 202–209, 2013.

[113] Z. Zhou, Y. Zheng, X. Ling, R. Hu and J. Zhou, 'A study on influence factors of small punch creep test by experimental investigation and finite element analysis', *Materials Science and Engineering: A*, **527** (10-11), pp. 2784–2789, 2010.

[114] F.-K. Zhuang, G.-Y. Zhou and S.-T. Tu, 'Numerical investigation of frictional effect on measuring accuracy of different small specimen creep tests', *International Journal of Pressure Vessels and Piping*, **110**, pp. 42–49, 2013.

APPENDIX A

SUBROUTINE FOR THE MODIFIED CONSTITUTIVE MODEL

```
SUBROUTINE CREEP(DECRA,DESWA,STATEV,SERD,ECO,ESWO,P,QTILD,
1 TEMP,DTEMP,PREDEF,DPRED,TIME,DTIME,CMNAME,LEXIMP,LEND,
2 COORDS,NSTATV,NOEL,NPT,LAYER,KSPT,KSTEP,KINC)

INCLUDE 'ABA_PARAM.INC'
CHARACTER*80 CMNAME
 INTEGER I, FLAG

INTEGER, PARAMETER :: DBL=8
INTEGER, PARAMETER :: SINGLE=4
REAL(KIND=DBL) A, B, LA, LB, W, DW, SRUP, PHI, PSI
REAL(KIND=SINGLE) N, M, X, ALPHA, QPR, TT, SI, WMAX
REAL(KIND=DBL) PRE_STRAIN
REAL(KIND=SINGLE) phi_a, phi_b, phi_c, phi_d
REAL(KIND=SINGLE) psi_a, psi_b, psi_c, psi_d
REAL(KIND=SINGLE) as, bs, cs, ms
DIMENSION DECRA(5),DESWA(5),STATEV(*),PREDEF(*),DPRED(*),
1 TIME(2),COORDS(*),EC(2),ESW(2)
```

```
      DO I=1,5
            DECRA(I)=0.0D0
            DESWA(I)=0.0D0
      ENDDO

C     VALUE FOR THE FLAG VARIABLE
C     —  1: PRESTRAIN EFFECTS=ON  —
C     —  0: PRESTRAIN EFFECTS=OFF  —
      FLAG=1

C———————————————————-
C———————————————————-
C     FITTING CONSTANTS FOR THE CORRELATION
C     OF TRUE STRAIN AND ENGINEERING STRAIN
      as=.05199
      bs=.1181
      ms=.5083
C———————————————————-
C———————————————————-

C     NOT PRE-STRAINED MATERIAL PROPERTIES
      A=1.51e-30
      N=11.795
      X=10.953
      B=2.120e-27
```

```
ALPHA=0.3
QPR=5.3
M=-4.754E-4


C      PHI PARAMETER FITTING CONSTANTS – AVERAGED
phi_a=-5.9534
phi_b=0.0669
phi_c=-0.0088
phi_d=3.2360e-04


C      PSI PARAMETER FITTING CONSTANTS – AVERAGED
psi_a=-3.2409
psi_b=0.0261
psi_c=4.7633e-04


C———————————————————-
C———————————————————-


C     INITIALISATION OF MATERIAL CONSTANTS
C     AND SOLUTION DEPENDENT VARIABLES
C     Limitation for maximum damage value
WMAX=0.9901


C     LEGEND FOR SOLUTION DEPENDENT VARIABLES:


C     1. STATEV(1) IS THE CREEP DAMAGE
C     2. STATEV(2) IS THE MAXIMUM PRINCIPAL STRESS
```

```
C     3. STATEV(3) IS THE RUPTURE STRESS
C     4. STATEV(4) IS THE CREEP STRAIN RATE
C    5. STATEV(5), DEFINED IN USDFLD, IS THE DAMAGE TAKEN FROM FIELD(1)
C     6. STATEV(6), DEFINED IN USDFLD, IS THE TRUE PRE-STRAIN VALUE
C     7. STATEV(7) IS THE PHI VARIABLE
C     8. STATEV(8) IS THE PSI VARIABLE

IF (KINC.EQ.1.AND.KSTEP.EQ.2) THEN
        STATEV(1)=0.0
        STATEV(4)=0.0
ENDIF


W=STATEV(1)
SI=STATEV(2)

IF (W.GE.WMAX) THEN
        W=WMAX
ENDIF

TT=TIME(2)

IF (LEND.EQ.0) THEN
        TT=TIME(2)-DTIME
ENDIF


C     Rupture stress definition

SRUP=ALPHA*SI+(1.0-ALPHA)*QTILD
```

```
IF (TT.EQ.0.0) THEN
      TT=TT+1.0e-6
ENDIF


C     MATERIAL CREEP BEHAVIOUR MODIFICATION
IF (FLAG.EQ.1) THEN
       PRE_STRAIN=100.0*(as*STATEV(6)+bs*STATEV(6)**ms)
ENDIF


C     DEFINITION OF CREEP STRAIN RATE
C     AND CREEP DAMAGE RATE


PHI=exp(phi_a*PRE_STRAIN)+phi_b*PRE_STRAIN**2.0+phi_c*
2PRE_STRAIN**3.0+phi_d*PRE_STRAIN**4.0

PSI=exp(psi_a*PRE_STRAIN)+psi_b*PRE_STRAIN**2.0+
2psi_c*PRE_STRAIN**3.0

IF (LEND.EQ.0) THEN

      IF (LEXIMP.EQ.1) THEN
            DECRA(5)=PHI*A*N*QTILD**(N-1.0)*exp(2.0*(N+1.0)/(3.1416*
            2sqrt(1.0+3.0/N))*W**1.5)*DTIME
      ENDIF


      DECRA(1)=PHI*A*QTILD**N*exp((2.0*(N+1.0))/
```

```
      2(3.1416*sqrt(1.0+3.0/N))*W**1.5)*DTIME

C     THE DAMAGE PARAMETER INCREASES AT THE END OF THE
      INCREMENT ONLY

      DW=0.0

      IF (W.GE.WMAX) THEN
            W=WMAX
      ENDIF

ENDIF

IF (LEND.EQ.1) THEN

      IF (LEXIMP.EQ.1) THEN
            DECRA(5)=PHI*A*N*QTILD**(N-1.0)*exp(2.0*(N+1.0)/(3.1416*
            2sqrt(1.0+3.0/N))*W**1.5)*DTIME
      ENDIF

      DECRA(1)=PHI*A*QTILD**N*exp((2.0*(N+1.0))/
      2(3.1416*sqrt(1.0+3.0/N))*W**1.5)*DTIME

      IF (SRUP.GE.0.0) THEN
            DW=PSI*B*(1.0-exp(-QPR))*(SRUP**X)*((exp(QPR*W))/QPR)*DTIME

            W=W+DW
            IF (W.GE.WMAX) THEN
                  W=WMAX
            ENDIF
```

```
      ENDIF

ENDIF

STATEV(1)=W
STATEV(2)=SI
STATEV(4)=DECRA(1)
STATEV(3)=SRUP
STATEV(7)=PHI
STATEV(8)=PSI

RETURN
END



c**********************************************************************
SUBROUTINE USDFLD(FIELD,STATEV,PNEWDT,DIRECT,T,CELENT,
 1 TIME,DTIME,CMNAME,ORNAME,NFIELD,NSTATV,NOEL,NPT,LAYER,
 2 KSPT,KSTEP,KINC,NDI,NSHR,COORD,JMAC,JMATYP,
 3 MATLAYO,LACCFLA)

INCLUDE 'ABA_PARAM.INC'
CHARACTER*80 CMNAME
CHARACTER*3 FLGRAY(15)
DIMENSION FIELD(NFIELD),STATEV(NSTATV),DIRECT(3,3),
1 T(3,3),TIME(2)
DIMENSION ARRAY(15),JARRAY(15),JMAC(*),JMATYP(*),COORD(*)
```

```
CALL GETVRM('PE',ARRAY,JARRAY,FLGRAY,JRCD,JMAC,JMATYP,
1 MATLAYO,LACCFLA)

C THE PLASTIC PRE-STRAIN, IN ABSOLUTE VALUE IS THE SOLUTION
DEPENDENT VARIABLE STATEV(6)

STATEV(6)=ARRAY(7)

IF (KSTEP.LT.2) THEN
      FIELD(1)=0.0
ENDIF


IF (KSTEP.EQ.2) THEN
      IF (KINC.EQ.1) THEN
            FIELD(1)=0.0
      ENDIF
      IF (KINC.GT.1) THEN
            IF (STATEV(1).GE.0.0) THEN
                  FIELD(1)=STATEV(1)
            ELSE
                  FIELD(1)=0.0
            ENDIF
      ENDIF
ENDIF


CALL GETVRM('SP',ARRAY,JARRAY,FLGRAY,JRCD,JMAC,JMATYP,
1 MATLAYO,LACCFLA)
```

```
STATEV(2)=ARRAY(3)
STATEV(5)=FIELD(1)

RETURN
END
```

APPENDIX B

SUBROUTINE FOR LEU'S FRICTION FORMULATION

```
SUBROUTINE fric_coef(fCoef, fCoefDeriv, nBlock, nProps,
*   nTemp, nFields, jFlags, rData, surfInt, surfSlv, surfMst,
*   props, slipRate, pressure, tempAvg, fieldAvg )

include 'aba_param.INC'

parameter( jKStep = 1,
*     jKInc = 2,
*     nFlags = 2,
*     jTimStep = 1,
*     jTimGlb = 2,
*     jDTimCur = 3,
*     nData = 3,
*     idfdSlipRate = 1,
*     idfdPressure = 2,
*     idfdtemperature = 3)
```

```
      dimension fCoef(nBlock), fCoefDeriv(nBLock,3),
     *     props(nProps),slipRate(nBlock),pressure(nBlock),
     *     tempAvg(nBlock), fieldAvg(nBlock,nFields),
     *     jFlags(nFlags), rData(nData)


      character*80 surfInt, surfSlv, surfMst

      real*8 s_u, n, mi, p, pmax, alpha1, alpha, den,
     *     dalpha_dp, dden, dmi_dalpha, dmi_dp


      n = 0
      s_u = 310
      var1 = nBlock
      var3 = jFlags(2)
      var4 = props(1)
      k1 = 1
      pmax=3200


      do k1=1,nBlock
            p = pressure(k1)
            ca=3.0
            alpha1 = ca*p/s_u
            alpha = TANH(alpha1)
            den = sqrt(3.0)*((1-alpha**2)**.5+alpha**
           *     (n/2))

            mi = alpha/den
```

```
if (p.eq.0.0) then
        p=.0001
        dalpha_dp = 12/s_u*exp(6*p/s_u)/
        *(exp(12*p/s_u)+2*exp(6*p/s_u)+1)
        dden = sqrt(3.0)*(.5*(1-alpha**2)**(-.5)*
        *(-2*alpha)+alpha**(n/2-1)*.5*n)
        p=0
elseif (alpha.ge.0.999) then
        alpha=0.999

        if (p.gt.pmax) then
                p=pmax
        endif

        dalpha_dp = 12/s_u*exp(6*p/s_u)/
        *(exp(12*p/s_u)+2*exp(6*p/s_u)+1)
        dden = sqrt(3.0)*(.5*(1-alpha**2)**(-.5)*
        *(-2*alpha)+alpha**(n/2-1)*.5*n)
        else
                dalpha_dp = 12/s_u*exp(6*p/s_u)/
                *(exp(12*p/s_u)+2*exp(6*p/s_u)+1)


                dden = sqrt(3.0)*(.5*(1-alpha**2)**(-.5)*
                *(-2*alpha)+alpha**(n/2-1)*.5*n)
        endif


dmi_dalpha = (den-alpha*dden)/
```

```
        *(den**2)


        dmi_dp = dmi_dalpha*dalpha_dp
        fCoef(k1) = mi

        fCoefDeriv(nBlock,1) = 0

        fCoefDeriv(nBlock,2) = dmi_dp
        fCoefDeriv(nBlock,3) = 0
enddo
return
end
```